



National Library
of Canada

Bibliothèque nationale
du Canada

Canadian Theses Service

Service des thèses canadiennes

Ottawa, Canada
K1A 0N4

NOTICE

The quality of this microform is heavily dependent upon the quality of the original thesis submitted for microfilming. Every effort has been made to ensure the highest quality of reproduction possible.

If pages are missing, contact the university which granted the degree.

Some pages may have indistinct print especially if the original pages were typed with a poor typewriter ribbon or if the university sent us an inferior photocopy.

Reproduction in full or in part of this microform is governed by the Canadian Copyright Act, R.S.C. 1970, c. C-30, and subsequent amendments.

AVIS

La qualité de cette microforme dépend grandement de la qualité de la thèse soumise au microfilmage. Nous avons tout fait pour assurer une qualité supérieure de reproduction.

S'il manque des pages, veuillez communiquer avec l'université qui a conféré le grade.

La qualité d'impression de certaines pages peut laisser à désirer, surtout si les pages originales ont été dactylographiées à l'aide d'un ruban usé ou si l'université nous a fait parvenir une photocopie de qualité inférieure.

La reproduction, même partielle, de cette microforme est soumise à la Loi canadienne sur le droit d'auteur, SRC 1970, c. C-30, et ses amendements subséquents.

UNIVERSITY OF ALBERTA

Pulsed Doppler Exploration of Arterial Velocity Fields

by

J. David Campbell



A THESIS

SUBMITTED TO THE FACULTY OF GRADUATE STUDIES AND RESEARCH
IN PARTIAL FULFILMENT OF THE REQUIREMENTS FOR THE DEGREE
OF DOCTOR OF PHILOSOPHY

Department of Physiology

EDMONTON, ALBERTA

Fall 1990



National Library
of Canada

Bibliothèque nationale
du Canada

Canadian Theses Service Service des thèses canadiennes

Ottawa, Canada
K1A 0N4

The author has granted an irrevocable non-exclusive licence allowing the National Library of Canada to reproduce, loan, distribute or sell copies of his/her thesis by any means and in any form or format, making this thesis available to interested persons.

The author retains ownership of the copyright in his/her thesis. Neither the thesis nor substantial extracts from it may be printed or otherwise reproduced without his/her permission.

L'auteur a accordé une licence irrévocable et non exclusive permettant à la Bibliothèque nationale du Canada de reproduire, prêter, distribuer ou vendre des copies de sa thèse de quelque manière et sous quelque forme que ce soit pour mettre des exemplaires de cette thèse à la disposition des personnes intéressées.

L'auteur conserve la propriété du droit d'auteur qui protège sa thèse. Ni la thèse ni des extraits substantiels de celle-ci ne doivent être imprimés ou autrement reproduits sans son autorisation.

ISBN 0-315-65032-X



University of Alberta
Edmonton

Department of Physiology
Faculty of Medicine

Canada T6G 2H7

7-55 Medical Sciences Building
Telephone: (403) 492-3359
Facsimile: (403) 492-8915

17th July, 1990.

To Whom It May Concern:

We hereby give J. David Campbell full permission to use our unpublished data on the Doppler signal originating in a dog carotid artery as Figure 6 in his Doctoral thesis entitled "Pulsed Doppler Exploration of Arterial Velocity Fields".

K.J. Hutchison, M.D., Professor.

E. Karpinski, Ph.D. P.Eng.
Faculty Service Office.

UNIVERSITY OF ALBERTA

RELEASE FORM

NAME OF AUTHOR J. David Campbell
TITLE OF THESIS Pulsed Doppler Exploration of
Arterial Velocity Fields
DEGREE FOR WHICH THESIS WAS PRESENTED DOCTOR OF PHILOSOPHY
YEAR THIS DEGREE GRANTED 1990

Permission is hereby granted to THE UNIVERSITY OF ALBERTA LIBRARY to reproduce single copies of this thesis and to lend or sell such copies for private, scholarly or scientific research purposes only.

The author reserves other publication rights, and neither the thesis nor extensive extracts from it may be printed or otherwise reproduced without the author's written permission.

(SIGNED) ...*J. D. Campbell*.....

PERMANENT ADDRESS:

..513 RH...MICHENER PARK
..EDMONTON ALBERTA..
.....T6H 4M5.....

DATED .AUGUST...24.....1990

THE UNIVERSITY OF ALBERTA
FACULTY OF GRADUATE STUDIES AND RESEARCH


The undersigned certify that they have read, and recommend to the Faculty of Graduate Studies and Research, for acceptance, a thesis entitled PULSED DOPPLER EXPLORATION OF ARTERIAL VELOCITY FIELDS submitted by J. David Campbell in partial fulfilment of the requirements for the degree of Doctor of Philosophy.

Dr. K.J. Hutchison

..... 

Supervisor

Dr. E. Karpinski

..... 

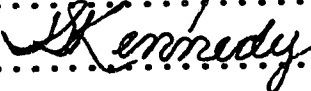
Dr. A.S. French

..... 

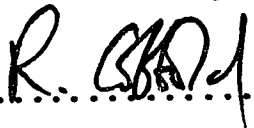
Dr. E.J. Sanders

..... 

Dr. J.S. Kennedy

..... 

Dr. R.S.C. Cobbold

..... 

External Examiner

Date

Dedication

To my parents, Bob and June, and my dear wife, Kathy, for all their support and nurturing, and to my Uncle John, who introduced me to goal setting - my thesis goal is finally achieved.

Abstract

One 20 MHz and one 10 MHz pulsed Doppler ultrasonic velocimeter (PDUVM) were used to explore disturbed velocity fields similar to those associated diagnostically and etiologically with arterial disease. The mean sample volume length of the 20 MHz PDUVM was 0.69 mm and its mean sample volume diameter was 0.97 mm. The corresponding dimensions of the 10 MHz PDUVM were 0.93 mm and 1.09 mm, respectively. In steady laminar flow convolution of both PDUVM sample volumes with the velocity field was apparent in the distorted velocity profiles measured; a compensation for convolution limited to laminar flow velocity profiles was developed. In steady and pulsatile post-stenotic flow, PDUVM detection of jet, separated and turbulent flow regimes was confirmed by comparing PDUVM velocity profiles and spectra with the actual velocity field revealed by flow visualization. In steady post-stenotic flow four sources of spectral broadening were demonstrated with the 20 MHz PDUVM: placement of the sample volume in the shear layer between jet and separation zones; turbulence due to jet breakup; transit time of scatterers through the sample volume; and use of the PDUVM at the extremes of its range. In pulsatile post-stenotic flow PDUVM spectral width decreased with increasing pulse rate at the site of peak flow disturbance but there was no effect of pulsatility on spectral width.

The 10 MHz PDUVM was used to record cross-sectional velocity contours at different phases of the pulse cycle 0.5

cm downstream of abdominal aortic branch arteries in anaesthetized dogs. Transient flow recirculation occurred in the post-systolic phase of the pulse cycle at the aortic wall opposite the branch artery. There was no recirculation at the systolic peak but there was asymmetry of the velocity contour. In a cast-derived, geometrically exact *in vitro* model of one of the renal branch sites the *in vivo* results were extended to a wider range of flow conditions. In steady and pulsatile flow paired recirculation zones (vortices) along the aortic wall opposite the branch were detected at moderate to high branch flow rates.

Acknowledgements

I wish to thank my supervisor, Dr. Ken Hutchison, for his support, encouragement, and wisdom, especially during the time when I was recovering from a severe illness. My thanks also go to Dr. Ed Karpinski for his encouragement and helpful supervision.

I am indebted to a number of individuals for technical assistance. Wendy Pearson, Nick Diakiw, Dave Ogden, Ken Burt, Tim Barry, Rod Gramlich, Don Smith, and Robert Rolff of the Department of Physiology all assisted me at one time or another. Chief among these was Wendy Pearson of Dr. Hutchison's lab. Her skill, enthusiasm, and supportive attitude are greatly appreciated. Dave Sands, formerly of the Department of Radio and Television, helped get me started on the high speed cinematography required for the flow visualization. Tom Villett of the Department of Mechanical Engineering provided several pieces of helpful advice and information.

I am grateful to Dr. Keir Pearson for the use of his high speed cinecamera and to Dr. Esmond Sanders for the use of his film projector.

Finally, I wish to acknowledge the financial support of The Alberta Heritage Foundation For Medical Research.

Table of Contents

Chapter	Page
I. INTRODUCTION	1
A. GENERAL INTRODUCTION	1
B. HEMODYNAMICS AND ATHEROSCLEROSIS	1
C. TECHNIQUES USED TO INVESTIGATE ARTERIAL VELOCITY FIELDS	10
Velocity Profiles and Waveforms	10
The Hot Film Anemometer	12
The Laser Doppler Anemometer	13
Flow Visualization	14
The PDUVM	15
D. VELOCITY FIELDS OF SPECIFIC ARTERIAL GEOMETRIES	16
Arterial Stenoses	16
Arterial Bends	20
Arterial Branches	22
Arterial Bifurcations	24
E. THE DOPPLER EFFECT AND PULSED DOPPLER VELOCIMETER	26
F. OBJECTIVES	35
Determination of Limits of the Method	35
Exploration of Post-stenotic Velocity Fields	36
Exploration of Velocity Fields in the Vicinity of Aortic Branches	37
II. MATERIALS AND METHODS	38
A. SAMPLE VOLUMES OF 10 AND 20 MHZ PDUVM'S	38
B. STEADY LAMINAR FLOW <i>IN VITRO</i>	40
The Cardiovascular Model	40
Experimental Protocol	45

Calculation of Doppler Shift Frequencies and Spectral Widths	46
Calculation of Laminar Velocity Profiles	51
C. POST-STENOTIC FLOW WITH STEADY UPSTREAM FLOW ...	51
D. POST-STENOTIC FLOW WITH PULSATILE FLOW UPSTREAM	53
E. BRANCHED AORTIC FLOW <i>IN VIVO</i>	62
Velocity Field Measurement	62
Measurement of Turbulence	65
Experimental Protocol	67
F. BRANCHED AORTIC FLOW <i>IN VITRO</i>	68
III. RESULTS	72
A. SAMPLE VOLUMES	72
B. VELOCITY PROFILES: LAMINAR AND POST-STENOTIC FLOW	72
Steady Laminar Flow	72
Post-stenotic Flow with Steady Flow Upstream	88
Post-stenotic Flow with Pulsatile Flow Upstream	104
Cross-sectional Profiles: Velocity Contours	108
C. VELOCITY CONTOURS AT AORTIC BRANCHES	108
Anaesthetized Dog Studies	110
<i>In Vitro</i> Model Studies	118
D. FACTORS AFFECTING PDUVM SPECTRAL WIDTH	132
Steady Laminar Flow	132
Post-stenotic Flow with Steady Flow Upstream	134
Post-stenotic Flow with Pulsatile Flow Upstream	140
<i>In Vivo</i> Aortic Branches	175

<i>In Vitro</i> Aortic Branches	175
IV. DISCUSSION	176
A. OPENING REMARKS	176
B. PDUVM SPATIAL RESOLUTION	177
Sample Volumes	177
Laminar Flow Velocity Profiles	180
Comparative Spatial Resolutions	182
C. PDUVM VELOCITY OUTPUT	183
D. PDUVM RECOGNITION OF POST-STENOTIC FLOW REGIMES	188
A Clinical Question	188
Jet and Separated Flow	188
Reasons for Variation in PDUVM Spectral Width	191
Jet Breakup in Pulsatile Flow	198
E. THE HEMODYNAMIC BASIS OF ATHEROSCLEROSIS	198
Wall Shear Stress	198
Pulsatile Post-Stenotic Flow	201
Branched Aortic Flow <i>In Vivo</i>	202
Branched Aortic Flow <i>In Vitro</i>	206
V. CONCLUSION	209
BIBLIOGRAPHY	212
APPENDIX	235

List of Tables

Table	Page
1 Steady laminar flow test section Reynolds numbers and the volume flow rates and tube diameters from which they were calculated.....	44
2 Comparison of theoretical and 20 MHz PDUVM spectral mean measured maximum velocities at the four steady laminar flow Reynolds numbers.....	79
3 Comparison of theoretical and 20 MHz PDUVM spectral maximum measured maximum velocities at the four steady laminar flow Reynolds numbers.....	84
4 Comparison of theoretical and 10 MHz PDUVM spectral mean measured maximum velocities at the four steady laminar flow Reynolds numbers.....	87
5 Comparison of theoretical and 10 MHz PDUVM spectral maximum measured maximum velocities at the four steady laminar flow Reynolds numbers.....	90
6 Variation of centrestream relative spectral width with axial location downstream of the three model stenoses at three Reynolds numbers each.....	141
7 Mean relative spectral widths, relative burst times, and time average relative spectral widths obtained from the bursting analysis of the PDUVM waveforms of figure 56....	164
8 Mean relative spectral widths, relative burst times, and time average relative spectral widths obtained from the bursting analysis of the PDUVM waveforms of figure 60....	172

List of Figures

Figure	Page
1 Schematic of the arterial tree and sites of atherosclerosis.....	8
2 Schematic of the PDUVM electronics.....	32
3 Schematic of the steady flow model circuit.....	41
4 Illustration of mode and contour frequencies of a Doppler spectrum.....	47
5 Demonstration of coincidence or non-coincidence of PDUVM mean and mode frequencies.....	49
6 The difference between PDUVM raw mean and mode frequencies and spectral widths <i>in vivo</i>	50
7 Schematic of the flow visualization apparatus.....	54
8 Schematic of the pulsatile flow model circuit.....	55
9 Outline of a sinusoidal cam and its base circle.....	57
10 Photograph of the cam-based pulsatile unit.....	59
11 Example of a grid of velocity waveforms.....	63
12 A three-dimensional velocity profile.....	64
13 Example of cross-sectional velocity contours.....	66
14 Photograph of the aortic branch model.....	70
15 Variation of PDUVM sample volume diameters with range gate position.....	73
16 20 MHz PDUVM mode frequency profile in steady laminar flow.....	75
17 20 MHz PDUVM mode frequency velocity profiles in steady laminar flow.....	76

List of Figures - cont'd

Figure	Page
18 20 MHz PDUVM mean frequency velocity profiles in steady laminar flow.....	77
19 Rationale for the convolution compensation procedure.	81
20 Compensated 20 MHz PDUVM steady flow velocity profiles.....	82
21 10 MHz PDUVM mode frequency velocity profiles in steady laminar flow.....	85
22 10 MHz PDUVM mean frequency velocity profiles in steady laminar flow.....	86
23 Compensated 10 MHz PDUVM steady flow velocity profiles.....	89
24 Photograph of the post-stenotic test section.....	92
25 Nine point steady flow velocity profile 0.4 cm downstream of the 2.9 mm model stenosis at a Reynolds number of 384.....	93
26 Cinecamera record of the visualized velocity field of figure 25.....	95
27 Scaled diagram of figure 26 with particle position vectors.....	96
28 Three distinct post-stenotic flow regimes identified by flow visualization.....	97
29 Correlation of PDUVM and visualized post-stenotic flow regime velocities.....	100
30 Steady flow velocity profiles at seven post-stenotic axial positions.....	101

List of Figures - cont'd

Figure	Page
31 Pulsatile flow velocity profiles at seven post-stenotic axial positions at six times in the pulse cycle.....	105
32 <i>In vivo</i> post-stenotic cross-sectional velocity contours.....	109
33 Cross-sectional aortic velocity contours 250 msec after the R wave near a dog cranial mesenteric artery.....	111
34 Cross-sectional aortic velocity contours 350 msec after the R wave near a dog cranial mesenteric artery.....	112
35 Cross-sectional aortic velocity contours 334 msec after the R wave near a dog left renal artery.....	115
36 Cross-sectional aortic velocity contours 334 msec after the R wave midway between a dog left and right renal arteries.....	117
37 Cross-sectional aortic velocity contours 334 msec after the R wave near a dog right renal artery.....	119
38 Steady flow cross-sectional model aortic velocity contours near the right renal artery at four different right renal flows.....	120
39 Grid of model aortic velocity waveforms near the right renal artery with steady upstream flow and maximum right renal flow.....	123
40 Steady flow cross-sectional model aortic velocity contours at four separate times near the right renal artery with maximum right renal flow.....	124

List of Figures - cont'd

Figure	Page
41 Centrestream pulsatile flow model aortic velocity waveforms near the right renal artery at three different right renal flows.....	126
42 Pulsatile flow cross-sectional model aortic velocity contours near the right renal artery 200 msec after triggering at three different right renal flows.....	128
43 Pulsatile flow cross-sectional model aortic velocity contours near the right renal artery at four different times in the pulse cycle at a right renal flow of 32 percent aortic flow.....	130
44 Pulsatile flow cross-sectional model aortic velocity contours near the right renal artery at four different times in the pulse cycle at a right renal flow of 48 percent aortic flow.....	131
45 Variation of PDUVM spectral width with range gate position in steady laminar flow.....	133
46 Schematic of the results of flow visualization downstream of the 0.19 cm model stenosis at a Reynolds number of 316.....	135
47 Steady flow mode frequency velocity profile one diameter downstream of the 0.19 cm model stenosis at a Reynolds number of 316.....	136
48 Relative spectral width across the tube diameter one diameter downstream of the 0.19 cm model stenosis at a Reynolds of 316.....	137

List of Figures - cont'd

Figure	Page
49 Axial variation of centrestream relative spectral width downstream of the 0.19 cm model stenosis at a Reynolds number of 717.....	139
50 Variation of maximum relative spectral width with tube Reynolds number for unstenosed and stenosed model flow conditions.....	142
51 Pulsatile flow centrestream 20 MHz PDUVM spectral waveform 0.6 cm downstream of the 0.19 cm model stenosis accompanied by the corresponding flow visualization record.....	144
52 Pulsatile flow centrestream 20 MHz PDUVM spectral waveform 1.6 cm downstream of the 0.19 cm model stenosis accompanied by the corresponding flow visualization record.....	146
53 Pulsatile flow centrestream 20 MHz PDUVM spectral waveform 2.6 cm downstream of the 0.19 cm model stenosis accompanied by the corresponding flow visualization record.....	149
54 Pulsatile flow centrestream 20 MHz PDUVM spectral waveform 3.6 cm downstream of the 0.19 cm model stenosis accompanied by the corresponding flow visualization record.....	152

List of Figures - cont'd

Figure	Page
55 Pulsatile flow centrestream 20 MHz PDUVM spectral waveform 14.8 cm downstream of the 0.19 cm model stenosis accompanied by the corresponding flow visualization record.....	155
56 Pulsatile flow centrestream 20 MHz PDUVM spectral waveforms at six post-stenotic axial positions and three pulse rates.....	157
57 Electromagnetic flow waveforms and corresponding sync pulses used in the three pulse rate experiments of figure 56.....	159
58 Diagram of smoothed PDUVM spectral waveform used to analyze the effect of pulse rate on post-stenotic turbulence production.....	162
59 Variation of time average relative spectral width with post-stenotic axial position at the three pulse rates....	166
60 Pulsatile flow centrestream 20 MHz PDUVM spectral waveforms at six post-stenotic axial positions and three pulsilities.....	169
61 Variation of time average relative spectral width with post-stenotic axial position at the three pulsilities..	173

List of Abbreviations

AC - alternating current
ASW - absolute spectral width
AVRLW - time average relative spectral width
BE - turbulent burst end
BPM - beats per minute
BS - turbulent burst start
cm - centimeter
C - speed of sound in a specified medium
DEC - Digital Equipment Corporation
Do - tube diameter
dB - decibel
EKG - electrocardiogram
FFT - Fast Fourier Transform
FM - frequency modulation
Fd - Doppler frequency shift signal
Fo - ultrasonic transmission frequency
Fr - backscattered ultrasound frequency
Fs - offset frequency used to obtain directional Doppler
signal
g - gram
HFA - hot film anemometer
Hz - hertz
kHz - kilohertz
kg - kilogram

List of Abbreviations - cont'd

L - entrance length for steady laminar flow
LDA - laser Doppler anemometer
M - mode frequency
MASW - mean absolute spectral width over a burst
MHz - megahertz
MMC - mean mode frequency over the whole pulse cycle
MRELW - mean relative spectral width over a burst
MRI - magnetic resonance imaging
m - meter
mg - milligram
min - minute
ml - millilitre
mm - millimeter
msec - millisecond
NaCl - sodium chloride
PDUVM - pulsed Doppler ultrasonic velocimeter
PP - pulse period
Q - volume flow rate
Q_m - mean volume flow rate
Q_p - peak volume flow rate
RELBT - relative burst time
Re - Reynolds number
R_o - tube radius
r - tube radial position

List of Abbreviations - cont'd

SAHA - sample and hold amplifier

sec - second

V - velocity

V_{max} - maximum velocity

V(r) - velocity profile

WCMRW - mean relative spectral width over the whole pulse cycle

WCMSW - mean absolute spectral width over the whole pulse cycle

θ - angle of ultrasonic beam with vessel axis

λ - flow pulsatility

μ - dynamic viscosity

π - the number pi

ρ - fluid density

Σ - summation notation

I. INTRODUCTION

A. GENERAL INTRODUCTION

The relationship between hemodynamics and arterial disease, which is a major motivation for exploring arterial velocity fields, is described in the first part of this introduction. The techniques used to explore arterial velocity fields are then reviewed. This is followed by an account of the findings of investigators of arterial velocity fields at specific geometries important in either the diagnosis or etiology of arterial disease. Since the pulsed Doppler ultrasound velocimetry technique used in this thesis is based on the Doppler effect, a brief account is given of the history and use of this effect. Finally, the introduction concludes with a statement of the objectives of this thesis.

B. HEMODYNAMICS AND ATHEROSCLEROSIS

The fundamental parameter of cardiovascular function is tissue perfusion, the volume flow of blood that delivers nutrient molecules to, and removes waste molecules from the body's cells (Berne and Levy, 1981). By increasing or decreasing the calibre of the arterioles (the normal site of major peripheral resistance) intrinsic and extrinsic cardiovascular control systems vary tissue perfusion according to the needs of the perfused cells. The sum total

of all the body's component perfusions, the cardiac output, is distributed by the large and medium-sized arteries to each specific tissue. When atherosclerotic disease results in the formation of a lumen-narrowing plaque in one of the distributing arteries, the narrowing site may become the flow determining resistance (Berguer and Hwang, 1974). Arterial stenosis is the term used to identify this possibly flow limiting site of reduced arterial lumen (Young, 1979). When atherosclerotic stenosis development is sufficiently advanced the resistance to flow becomes excessively high and the downstream tissue experiences insufficient perfusion (ischemia). If the stenosis site abcesses, an embolism may form and cut off the downstream flow completely. In either case, if the downstream tissue is the heart or brain life-threatening tissue death (infarction) may result.

Because atherosclerosis accounts for so much morbidity and mortality in the Western world (Levy, 1981; Robbins and Angell, 1976), it is of prime importance to detect the disease as early as possible. The problem is essentially one of detecting altered fluid dynamics of the blood, i.e. disturbed hemodynamics, since the atherosclerotic plaque encroaching on the lumen disrupts the normally laminar flow patterns and produces post-plaque flow disturbances (Blackshear *et al.*, 1979).

Before the advent of Doppler ultrasound, arterial disease was mainly assessed by clinical examination and contrast arteriography. Some non-invasive techniques were

available, but use of these was limited for the most part to their original developers. Contrast arteriography, because of its invasive nature and potential risks was, and continues to be, limited to pre-operative patients (Strandness, 1986). It is not suitable for repetitive studies.

With the advent of Doppler ultrasound, the diagnosis of arterial disease was significantly improved. This is especially true for extracranial disease of the carotid artery, which is readily accessible by ultrasound and has a high incidence of atherosclerosis (Spain, 1966; Wesolowski *et al.*, 1965). Initially, a number of indirect Doppler tests were used, such as the supraorbital Doppler examination (Lye *et al.*, 1976). The disadvantages of such tests are that they cannot provide specific localizing information and cannot be used to grade the severity of the lesion. Today, the indirect carotid tests have been mostly superceded by the direct technique of duplex scanning (Fell *et al.*, 1981).

Duplex scanning for arterial disease currently involves real time B-mode ultrasonic imaging of the vessel of interest and pulsed Doppler ultrasonic velocimeter (PDUVM) inspection of the velocity field via real time fast Fourier transform (FFT) spectral analysis of the PDUVM signal (Fell *et al.*, 1981). The B-mode vascular image serves as a guide for placement of the PDUVM sample volume within the vessel lumen. The B-mode image also allows measurement and control of the angle between the vascular and PDUVM beam axes.

Diagnosis of arterial disease is based upon the departure of the PDUVM spectra from normal peak frequencies and spectral widths. The increase in peak frequency is interpreted as being due to the presence of an atherosclerotic stenosis generating a high velocity jet. The increase in spectral width is usually interpreted as due to post-stenotic turbulence, although in the lateral aspect of the carotid sinus spectral broadening is a normal finding (Phillips *et al.*, 1983; Ku *et al.*, 1985b). Qualitative spectral analysis criteria have been developed by correlating the findings of independently interpreted contrast arteriograms (Zierler *et al.*, 1983a). The artery under consideration is placed in one of five categories: normal; minimal stenosis; non-hemodynamically significant stenosis; hemodynamically significant stenosis; and total occlusion. The diagnostic accuracy of duplex scanning using these criteria is best for hemodynamically significant stenoses and poorest for normal and mildly stenosed arteries. However, results with computer-based pattern recognition spectral analysis suggest that normal and mildly stenosed arteries may be detected with greater accuracy (Greene *et al.*, 1982; Knox *et al.*, 1982).

There are numerous applications of Doppler ultrasound in the detection of non-carotid arterial disease. Duplex scanning is used to assess branches of the abdominal aorta and the major arteries in the lower limbs (Jager *et al.*, 1985; Rittgers *et al.*, 1985). Continuous wave Doppler

flowmeters are used to analyze the velocity waveform patterns in peripheral vascular disease (Johnston *et al.*, 1978). If occlusive disease is present, it will show up in a downstream dampening of the velocity waveform. Continuous wave Doppler flowmeters are used to make non-invasive, segmental blood pressure measurements for locating sites of arterial occlusion in the limbs (Yao *et al.*, 1969; Strandness and Bell, 1965). Doppler flowmeters are also used to test for intermittent claudication and impotence due to arterial disease (Sumner and Strandness, 1969; Kempczinski, 1979). In patients who undergo surgical treatment for arterial disease, Doppler flowmeters become a valuable tool to assess the success of surgery (Strandness and Bell, 1966). During arterial reconstructions Doppler flowmeters find use in the assessment of flow patterns in the reconstructed segment (Barnes and Garrett, 1978; Zierler *et al.*, 1983b). There are at least four transcranial applications of pulsed Doppler flowmeters: detection of intracranial stenosis (Aaslid and Lindegaard, 1986); cerebrovascular spasm (Seiler *et al.*, 1986); arteriovenous malformation (Lindegaard *et al.*, 1986); and cerebral aneurism (Gilsbach and Harders, 1986).

The study of arterial hemodynamics is important not only in the diagnosis of arterial disease, but also in the investigation of its etiology. The initiation of atherosclerosis is still very poorly understood, and many hypotheses of atherogenesis have been proposed. One

hypothesis which is currently receiving serious attention is the so-called "Response to Injury Hypothesis" (Ross and Glomset, 1976a, 1976b). According to this view, chronic injury to arterial endothelial cells results in increased adhesiveness of the tunica intima to circulating platelets or monocytes. The nature of the endothelial injury is poorly defined, but is thought to lie somewhere along a spectrum between denudation and non-denudation (Ross, 1986). The injured endothelium, or the adherent cells above are activated to release Platelet Derived Growth Factor or a similar growth factor which is chemotactic and mitogenic for vascular smooth muscle cells. The latter then migrate from the tunica media to the intima, where they multiply and secrete connective tissue and other substances to form the well known "space occupying lesions" of atherosclerosis.

The critical question with regard to the Response to Injury hypothesis is: what agents or factors are responsible for the chronic injury to arterial endothelial cells? Texon (1957) was the first to suggest that hemodynamic factors might initiate the atherosclerotic process. He hypothesized that at specific points in the bends and branches of the arterial tree suction forces developed due to local increases in blood velocity. Texon believed that continued exposure of the intima to such suction forces would result in intimal thickening and plaque development. More recently, high shear (Fry, 1968), low shear (Caro *et al.*, 1971), and turbulence (Stehbens, 1974; 1973; 1968) have been suggested

as the means by which endothelial cells become injured. The evidence for a hemodynamic role in atherogenesis is indirect and based primarily on correlations of the observed lesion foci with sites of disturbed flow demonstrated in models of arterial branch points, bends, and stenoses (D'Luna *et al.*, 1982; Fox and Hugh, 1966; Wesolowski *et al.*, 1965). Some of the known sites of predilection of atherosclerotic plaques are illustrated in figure 1. Certain "Risk Factors" of atherosclerosis also provide indirect evidence in favour of a hemodynamic basis of this disease. Hypertension would be expected to distort arterial geometries resulting in increased flow disturbance (Nerem and Levesque, 1983). Also, heredity as a risk factor in atherogenesis can be explained hemodynamically via the inheritance of arterial geometries promoting excessive flow disturbance (Friedman *et al.*, 1983). In the past two decades there have been some fundamental studies on the occurrence of flow disturbances *in vivo* (Hutchison and Karpinski, 1982; Giddens *et al.*, 1976). Thus the predictions of model studies are starting to be verified in the only situation which will yield direct evidence on the role of hemodynamic factors in atherogenesis.

There has recently been a swing towards the low shear hypothesis with respect to disease of the carotid bifurcation (Ku *et al.*, 1985a; Zarins *et al.*, 1983; Kjaernes *et al.*, 1981). At this location the evidence points strongly toward an association between recirculation and low or

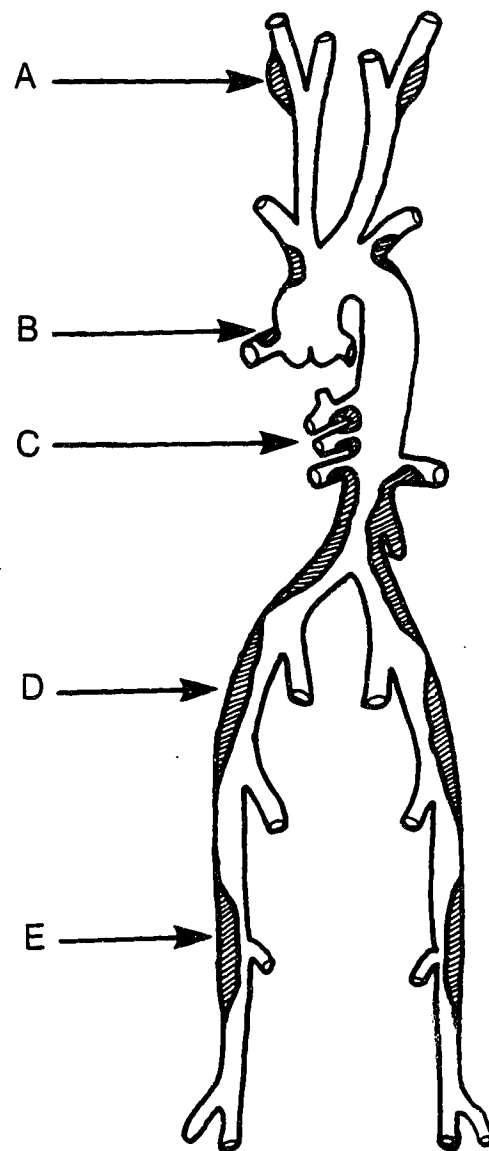


Figure 1. Schematic of the major vessels of the arterial tree and the known sites of predilection (hatched) for atherosclerotic disease (modified from Wesolowski *et al.*, 1965). A. Carotid bifurcation. B. Coronary arteries. C. Abdominal aorta branches. D. Ilio-femoral segment. E. Femoro-popliteal segment.

oscillatory shear with atherosclerotic plaque development. Apart from this location there remains uncertainty as to what specific hemodynamic effect is associated with atherogenesis. There are several reasons for this. First, our knowledge of the specific localization of early atherosclerotic lesions within most arterial bends, branches, and bifurcations is uncertain (Nerem, 1981). Second, the pulsatile nature of arterial blood flow dictates that flow disturbances will oscillate, both temporally and spatially, over the pulse cycle (Naumann and Schmid-Schonbein, 1983). Therefore, an endothelial site which experiences high shear during early systole may well experience low shear during late systole or diastole. There is currently a lack of detailed, quantitative information regarding the hemodynamics of arterial flow disturbances *in vivo* as a function of the pulse cycle (Taylor, 1983). Finally, there is some disagreement as to what animal model is representative of human atherosclerosis (Stehbens, 1975).

Before questions regarding the correlation of atheroma sites with arterial flow disturbances can be properly addressed, the spatial and temporal details of the latter must be known. Unlike steady laminar flow in a straight tube, arterial flow disturbances are predicted to have both forward and reverse velocities during systole, and to have their velocity vectors distributed along all three coordinate axes (Naumann and Schmid-Schonbein, 1983; Roberson and Crowe, 1980). Moreover, since conduit geometry

is very important in determining flow conditions, the tremendous variation in vascular geometries further complicates the velocity patterns found in the arterial tree.

Fluid dynamicists are familiar with the problem of analyzing such complicated flow systems. Their usual solution is to take the Eulerian point of view (Roberson and Crowe, 1980), treat a complex flow system as a velocity field, and analyze it with the appropriate tools. These include experimental measurements involving, for example, the hot film anemometer (HFA), the laser Doppler anemometer (LDA), and the pulsed Doppler ultrasonic velocimeter (PDUVM). The tools of experimental investigators of arterial velocity fields are discussed in the following section.

C. TECHNIQUES USED TO INVESTIGATE ARTERIAL VELOCITY FIELDS

Velocity Profiles and Waveforms

Most investigators of arterial velocity fields have employed one or more of four velocity-sensing techniques: hot-film anemometry, laser Doppler anemometry, flow visualization, and pulsed Doppler ultrasonic velocimetry. Very recently Magnetic Resonance Imaging (MRI) has been used to study post-stenotic velocity fields (Rittgers *et al.*, 1988). The HFA, LDA, and PDUVM techniques all rely on the interpretation of velocity profiles and velocity waveforms. Very rarely velocity profiles are obtained by quantitative

flow visualization (Karino *et al.*, 1979; Karino and Goldsmith, 1985). A velocity profile is a plot of the velocity distribution across the diameter of the vessel under investigation at a particular instant in time. A blunt or flat velocity profile shape may result from a number of flow conditions. If the flow is steady (is not pulsatile, does not change with time) the velocity profile may be blunt because the viscous boundary layer adjacent to the vessel wall is not fully developed. The classic example of this is the flow at the entrance to a pipe (Seed and Wood, 1971). Alternatively, a blunt velocity profile in steady flow may be due to the presence of fully developed turbulence. Other causes of blunt velocity profiles are the presence of a non-Newtonian fluid, tapering in the flow vessel, and the presence of pulsatile flow, especially during acceleration. A parabolic profile is typically observed in fully developed steady laminar flow (Seed and Wood, 1971). Skewing or asymmetry in a velocity profile may occur in the vicinity of curves or branches in a vessel due to localized acceleration of fluid elements when the local radius of vessel curvature changes. Velocity profile skewing also occurs in the presence of flow separation, which is characterized by radical divergence of a boundary (wall) flow zone from adjacent, more centrestream flow elements due to a positive downstream pressure gradient (Fox and Hugh, 1966).

A velocity waveform is a record of the variation of velocity with time in the pulse cycle at a particular

location in the vessel lumen. The presence of fluctuations or high frequency content in centrestream velocity waveforms has been used to detect disturbed or turbulent flow. In early studies flow disturbance was detected by visual assessment of velocity waveforms (Ling *et al.*, 1968; Nerem and Seed, 1972) while in later studies it was detected by more quantitative methods involving spectral analysis (Gutstein *et al.*, 1973; Kim and Corcoran, 1974; Cassanova and Giddens, 1978). Flow disturbance and turbulence have been shown to be features of the post-stenotic velocity field (Young and Tsai, 1973a; 1973b; Yongchareon and Young, 1979). They have been infrequently observed in the unstenosed aorta, usually in the thoracic segment (Ling *et al.*, 1968; Kiser *et al.*, 1976).

The operation, advantages, and limitations of the HFA, LDA, flow visualization, and PDUVM techniques will be briefly described in the following subsections. The MRI technique is still not fully developed (Rittgers *et al.*, 1988), and will not be discussed further in this thesis.

The Hot Film Anemometer

The hot film anemometer measures the convective heat transfer between the local fluid flow and its heated film sensor. Since this heat transfer is proportional to the flow velocity, the velocity near the sensor can therefore be detected. The HFA has been used to explore arterial velocity fields both *in vivo* and *in vitro*. *In vivo* studies have

mostly been limited to single axial locations due to the necessity of puncturing the vessel wall. A further *in vivo* difficulty is the tendency of the hot film to become desensitized due to the accumulation of clotted platelets and fibrin. Two other problems with the HFA encountered both *in vitro* and *in vivo* are the potential for disturbing the flow field and a non-linear output which complicates calibration. Also, early HFA devices lacked directional capability. Nevertheless, the hot film anemometer has a high frequency response, which has facilitated the acquisition of much useful information on arterial flow disturbances. Furthermore, the HFA performance in the measurement of undisturbed steady and pulsatile blood velocity profiles has been rigorously tested and found to be of a high quality (Ling *et al.*, 1968). Most of the *in vivo* HFA studies have been conducted in the aortas of anaesthetized animals such as dogs or pigs. The work has generally involved qualitative descriptions of measured velocity profiles and/or velocity waveforms at different locations along the aortic axis.

The Laser Doppler Anemometer

The LDA detects the Doppler frequency shift of laser light reflected from tiny particles moving in a flow field. Since this frequency shift is, by the Doppler effect, proportional to the particle velocity, the velocity at the reflection site ('sample volume') can therefore be measured. Laser Doppler anemometry is the most powerful technique for

describing a velocity field because it can measure velocity vectors along two coordinate axes, has a high spatial resolution due to a relatively small sample volume, and can sense bidirectional flow (Bharadvaj *et al.* 1982a). The LDA has, however, a major disadvantage with respect to the exploration of arterial velocity fields: it cannot be used *in vivo* because the vessel wall blocks the transmission of the laser light. Therefore LDA studies are typically conducted in clear-walled arterial models filled with a transparent liquid such as water or glycerol in water. Minute particles, such as silicone carbide, titanium dioxide, or latex are added to the model fluid to enhance the backscattering of light from the sample volume. The chief advantage of the LDA method over the hot film anemometer is the capability of recording velocities at multiple axial locations. Many investigators have taken advantage of this feature, especially in models of arterial bifurcations and branches.

Flow Visualization

Flow visualization, usually conducted in clear-walled arterial models made of glass or plastic, involves seeding the flow fluid (usually water, saline, or some other transparent liquid) with minute tracer particles such as hydrogen bubbles or dyes. The velocity field is then determined by observing and/or photographing the paths taken by the tracer particles (Clayton and Massey, 1967;

Merzkirch, 1979). After this, the data is usually summarized in a qualitative way, although some quantitative flow visualization studies have been reported (Karino *et al.*, 1979; Karino and Goldsmith, 1985). An early report of flow visualization related to arterial velocity fields was made by Fox and Hugh (1966). Using open channel models and fine aluminum powder scattered over the surface of moving water, they showed that flow separation can occur at branches, bends, and expansion sites. Fox and Hugh proposed that such flow separation could favour the development of atherosclerosis at analogous sites in the arterial tree. Although their model geometries only crudely resembled those found in arteries, the work of Fox and Hugh provided a new direction for atherosclerosis research.

The PDUVM

The pulsed Doppler ultrasonic velocimeter detects the Doppler frequency shift of ultrasound backscattered from tiny particles, such as erythrocytes, moving in a flow field. Since this frequency shift is, by the Doppler effect, proportional to the particle velocity, the velocity in the sample volume (analogous to the LDA) can therefore be measured. A more detailed description of the operation of the PDUVM is given in a later section of this introduction (see 'The Doppler Effect and Pulsed Doppler Velocimeter'). The spatial resolution of pulsed Doppler explorations of arterial velocity fields has sometimes been criticized

because the PDUVM sample volume is typically much larger than that of the laser Doppler anemometer. Nevertheless, the PDUVM can be used *in vivo*, where laser Doppler anemometry and most forms of flow visualization cannot be used. Furthermore, the PDUVM is a completely non-invasive device and is therefore more suitable than the hot film anemometer for *in vivo* application. Indeed, as has been mentioned previously (see 'Hemodynamics and Atherosclerosis' above) the PDUVM is used extensively in clinical settings.

D. VELOCITY FIELDS OF SPECIFIC ARTERIAL GEOMETRIES

Arterial Stenoses

Arterial stenosis was briefly defined in the section on hemodynamics and atherosclerosis. It is worth repeating here that arterial stenosis is a clinical condition, usually as a result of atherosclerotic disease. Furthermore, because of the previously mentioned dangers of this pathological geometry to the downstream tissue, its detection is of prime importance. Arterial stenosis can be detected by identifying the flow disturbances it produces in the downstream velocity field (see below), and thus a major objective of the non-invasive diagnosis of arterial disease is the detection of disturbed hemodynamics caused by arterial stenosis. Arterial stenoses are also important from the point of view of etiology of arterial disease. Artificial and *in vitro* stenoses are easily produced and generate flow disturbances

which are also found at other arterial geometries associated with atherosclerosis. Such stenoses are therefore a convenient means of studying the relationship between disturbed hemodynamics and atherogenesis.

The fluid dynamics of stenoses can be illustrated by considering the diameter changes that occur as one passes through a stenosis from the upstream to the downstream end. As the upstream end of the stenosis is approached the tube diameter decreases and the fluid elements are accelerated due to the continuity principle of fluid dynamics (Roberson and Crowe, 1980). The resultant high velocity fluid emerging from the downstream end is known as a jet (Cassanova and Giddens, 1978; Hutchison and Karpinski, 1985). The tube diameter abruptly increases at the downstream end of the stenosis and, again due to the continuity principle, the fluid velocity across the tube decreases. This causes the lateral fluid pressure to increase, thus resulting in a positive pressure gradient between the stenosis and the post-stenotic velocity field. The positive pressure gradient favours separation from the jet of the slower moving fluid lateral to it (Azuma and Fukushima, 1976; Ahmed and Giddens, 1983a). The separated fluid reverses direction at the tube wall forming a recirculation zone between the jet and tube walls. At some finite distance downstream of the separation point the separated fluid reattaches to the rest of the forward moving fluid due to a decline in the positive pressure gradient. Near the reattachment site the jet decays

or breaks up into slower moving fluid with or without flow disturbance. Flow disturbance may also be generated in the shear layer between the jet and recirculation zone. The extent of the recirculation zone and the type of post-stenotic flow disturbance generated depend on the stenosis grade (percent area or diameter reduction), the upstream Reynolds number, and the steadiness or unsteadiness (time variation) of the flow.

In steady (constant over time) flow at a fixed Reynolds number the axial and radial extent of the post-stenotic recirculation zone and the amount of flow disturbance increased with increasing stenosis grade (Ahmed and Giddens, 1983a; Young and Tsai, 1973a). For a fixed stenosis grade the axial extent of the post-stenotic recirculation zone increased with decreasing Reynolds number (Ahmed and Giddens, 1983a). Asymmetric post-stenotic recirculation zones have been observed in steady flow, especially when the stenoses were asymmetric (Lesvesque *et al.*, 1986; Azuma and Fukushima, 1976; Greene and Hstrand, 1979). Two types of post-stenotic flow disturbance have been observed in steady flow: vortex shedding and turbulence (Ahmed and Giddens, 1983b).

In pulsatile (unsteady or time varying) flow the amount of flow disturbance increased with increasing stenosis grade (Young and Tsai, 1973b; Giddens and Khalifa, 1982). At low stenosis grades flow disturbance, if any, occurred during the systolic deceleration phase (Giddens *et al.*, 1976; Azuma

and Fukushima, 1976). As stenosis grade increased flow disturbance spread to other parts of the cycle until the flow was continuously disturbed at extremely severe stenosis grades (Giddens *et al.*, 1976; Thiele *et al.*, 1983). Three types of post-stenotic flow disturbance have been observed in pulsatile flow; a start-up structure, a shear layer oscillation, and turbulence (Khalifa and Giddens, 1981). Vortex shedding and coherent structures have also been seen in pulsatile post-stenotic flow (Giddens *et al.*, 1976; Giddens and Khalifa, 1982; D'Luna *et al.*, 1982; Talukder *et al.*, 1986). Pulsatile post-stenotic flow disturbance has been observed to increase with decreasing Womersley pulse frequency parameter (D'Luna *et al.*, 1982; Yongchareon and Young, 1979). As has been observed in steady flow, asymmetric recirculation zones have been detected in pulsatile post-stenotic flow (Lesvesque *et al.*, 1986; Hutchison and Karpinski, 1985; Greene and Hirst, 1979; Azuma and Fukushima, 1976).

Flow disturbance intensity has been observed to peak then diminish with increasing post-stenotic axial distance (Khalifa and Giddens, 1981; Ahmed and Giddens, 1983; Giddens *et al.*, 1983). The position of the maximum flow disturbance was downstream of the velocity maximum (in the jet), and occurred in the region of jet decay (Ahmed and Giddens, 1983b; Hutchison and Karpinski, 1985). Spectral analysis of the velocity signal was used to characterize the flow disturbances downstream of *in vitro* model stenoses (Kim and

Corcoran, 1974; Cassanova and Giddens, 1978; Khalifa and Giddens, 1981; Ahmed and Giddens, 1983b). While this permitted a more quantitative description of flow disturbance the post-stenotic pattern was, in general, similar to that observed by other methods.

Arterial Bends

Vessel curvature occurs frequently in the arterial tree and, in some cases, such as the aortic arch, the change in vessel direction is quite considerable. The fluid dynamics of arterial bends can be extremely complicated (Lyne, 1970; Zalosh and Nelson, 1973; Smith, 1975; Talbot and Gong, 1983), and a full treatment of the subject is beyond the scope of this thesis. Nevertheless, the fluid dynamics of arterial bends are briefly discussed here since this geometry has been implicated in the etiology of atherosclerosis (Fox and Hugh, 1966; Texon, 1957).

The curvature of a vessel causes the fluid elements along the inside of the bend to be centripetally accelerated to a greater degree than the elements along the outside. Thus the velocity profile is skewed toward the inside of the bend. This is the recognized flow pattern under entrance (inviscid) flow conditions (Nerem, 1981). Under fully developed or viscous flow conditions, however, the velocity profile in a bend is skewed toward the outer wall due to so-called secondary flow effects (Nerem *et al.*, 1976). The latter result from the centripetal pressure gradient which

accompanies the centripetal acceleration of the fluid elements in the bend. By the Bernoulli effect the higher velocities along the inside of the bend cause a decrease in the lateral pressure at that site and the low outer bend velocities cause an increase in the pressure there. Because of the pressure gradient in the bend, not only secondary flows, but flow separation may occur. Separation predominantly occurs along the inside of a bend (Fox and Hugh, 1966; Gessner, 1973; Farthing and Peronneau, 1979; Talbot and Gong, 1983), but may also occur along the outside (Fox and Hugh, 1966). The reduced velocities in a separation zone cause a velocity profile to be skewed away from it, i.e. predominantly toward the outer wall of a bend.

The velocity fields observed in arterial bends vary considerably due to the conflicting factors above and perhaps also due to insufficient data. In the ascending aorta, which is a recognized entrance region (Nerem, 1981) the velocity profile was skewed toward the inside wall (Seed and Wood, 1971). On the other hand, Rodkiewicz (1975) demonstrated flow separation along the inner wall of the aortic arch. Farthing and Peronneau (1979) have observed flow reversal mostly along the inner wall of the aortic arch, but occasionally along the outer wall. Falsetti *et al.* (1972) observed velocity profile skewing in the ascending aorta but were unable to show a consistent direction. Consistent skewing of velocity profiles toward the outer wall has been shown in the left main coronary artery (Nerem

et al., 1976; Altobelli and Nerem, 1985) but not by all investigators (Wells *et al.*, 1977).

Arterial Branches

Before a vessel branches it is called the parent vessel. The branches of the parent vessel are then known as the daughter vessels. When there are only two daughter vessels of similar size the branch site is known as a bifurcation. Sometimes, as occurs in the abdominal aorta, one of the daughter vessels is much larger than the other and is known as the main branch. The smaller vessel is then known as the side branch. As it is for arterial bends, the study of arterial branch sites is important in investigations into the etiology of arterial disease (Fox and Hugh, 1966). In this section findings on branches of the type found in the abdominal aorta are reviewed. Results from arterial bifurcations are reviewed in a separate section immediately following the present one.

The fluid dynamics of arterial branches is dominated by the increase in total cross-sectional area at the branch site and the flow division into the daughter branches. The increase in cross-sectional area reduces the velocities in the daughter branches which results in increased lateral pressures. Thus there exists a positive pressure gradient at the entrance to each branch and, if the gradient is steep enough, flow separation will occur. If separation occurs it is located along the outer (continuous with parent) walls of

the branches since this is where the fluid velocity is lowest and pressure the highest. If the flow into one particular branch is decreased flow velocities will decrease proportionately, the lateral pressure will therefore increase, and thus further flow separation will be favoured.

Flow disturbance (Gutstein *et al.*, 1973) and skewing of the main branch velocity profile toward the side branch wall (Houle and Roach, 1981) have been observed at arterial branch sites. In steady flow conditions flow reversal and/or flow separation have been demonstrated along the main branch wall opposite the side branch (El Masry *et al.*, 1978; Karino *et al.*, 1979; Houle and Roach, 1981; Liepsch *et al.*, 1982; Lutz *et al.*, 1983; Karino and Goldsmith, 1985; Karino *et al.*, 1989). The size of the main branch separation zone was increased with increasing flowrate through the side branch (Karino *et al.*, 1979), increasing side-to-main branch diameter ratio (Karino and Goldsmith, 1985), and increasing upstream Reynolds number (El Masry *et al.*, 1978). No such separation zone was observed in physiological pulsatile flow and therefore it was suggested that caution be exercised in extrapolating steady flow results to pulsatile conditions (Lutz *et al.*, 1983). A smaller region of flow separation and/or reversal was detected along the upstream wall of the side branch under steady (Karino *et al.*, 1979; Houle and Roach, 1981; Karino and Goldsmith, 1985) and pulsatile (Sabbah *et al.*, 1984a) flow conditions. Helical flow patterns were also observed in some side branches (Fukushima

et al., 1988; Sabbah *et al.*, 1984b).

Arterial Bifurcations

In a bifurcation, the site of meeting of daughter branch walls at which the flow divides is known as the flow divider. The carotid bifurcation, a particularly well studied geometry in the arterial tree, is asymmetric. It consists of the division of the common carotid artery into the internal and external carotid branches, the former branch having a larger diameter. Also, the internal carotid branch expands at the bifurcation junction into a bulb known as the carotid sinus.

There are two prominent features of bifurcation velocity fields; velocity profile skewing, and the possibility of flow separation. The velocity profiles in the daughter branches are typically skewed toward the flow divider walls because the fluid elements impinging on the flow divider originate in the centrestream of the parent vessel. These fluid elements are normally moving at higher velocities than those adjacent to the walls of the parent vessel. The latter flow into the region along the outer (opposite the flow divider) walls of the daughter branches, thus reinforcing the direction of velocity profile skewing. Flow separation in a bifurcation may occur due to the rise in local pressure which accompanies the increase in cross-sectional area described in the section on arterial branches. When separation does occur it is located along the

outer (lateral) walls of the bifurcation.

Velocity profile skewing toward the inner (flow divider) walls of arterial bifurcations has been demonstrated in numerous studies under both steady (Brech and Bellhouse, 1973; Walburn and Stein, 1980; Bharadvaj *et al.*, 1982a) and pulsatile (Brech and Bellhouse, 1973; Walburn and Stein, 1980; Friedman *et al.*, 1981; Friedman *et al.*, 1987) flow conditions. Flow separation along the lateral walls of arterial bifurcations has also been a frequent finding (El Masry *et al.*, 1978; Malcolm and Roach, 1979; Walburn and Stein, 1980; Logerfo *et al.*, 1981a, 1981b; Bharadvaj *et al.*, 1982a, 1982b; Ku and Giddens, 1983; Fukushima *et al.*, 1988), although it has not always occurred in both branches (El Masry *et al.*, 1978; Walburn and Stein, 1980; Bharadvaj *et al.*, 1982a, 1982b) or at low Reynolds numbers (El Masry *et al.*, 1978; Friedman *et al.*, 1980). The size of arterial bifurcation separation zones has been shown to increase with decreasing flow into the branch in which the zone is located (Malcolm and Roach, 1979; Logerfo *et al.*, 1981a, 1981b; Bharadvaj *et al.*, 1982a) and to increase with increasing upstream Reynolds number (El Masry *et al.*, 1978; Bharadvaj *et al.*, 1982a).

Special findings in the well studied human carotid bifurcation deserve mention. A prominent zone of flow separation was observed along the outer wall of the carotid sinus (Logerfo *et al.*, 1981b; Bharadvaj *et al.*, 1982a, 1982b; Ku and Giddens, 1983; Fukushima *et al.*, 1988). In

steady flow this separation zone moved upstream with decreasing internal carotid artery flow and increasing common carotid artery flow (Bharadvaj *et al.*, 1982b) and increased in size with increasing external carotid artery flow (Logerfo *et al.*, 1981b). In pulsatile flow the sinus separation zone was formed during systolic acceleration, expanded during systolic deceleration, and remained expanded during diastole (Ku and Giddens, 1983). Wall shear stresses measured by the velocity profile technique in steady (Zarins *et al.*, 1983) and pulsatile (Ku *et al.*, 1985a) flow have revealed that the outer sinus wall is a region of low, sometimes reversed or oscillatory shear, while the inner (flow divider) wall is a region of high shear. Helical secondary flows have also been observed in the carotid sinus (Logerfo *et al.*, 1981b; Bharadvaj *et al.*, 1982b; Ku and Giddens, 1983) and systolic flow reversal has been detected ultrasonically along the sinus outer wall (Phillips *et al.*, 1983; Ku *et al.*, 1985b).

E. THE DOPPLER EFFECT AND PULSED DOPPLER VELOCIMETER

Users of pulsed Doppler technology are indebted to the Austrian mathematician/physicist Christian Doppler, who discovered the Doppler effect in the mid-nineteenth century (White, 1982; Eden, 1986). Simply put, the Doppler effect states that whenever there is relative motion between a wave source and an observer, the observed wave frequency will be greater or less than the source frequency, depending on the

direction of the velocity vector. In his original paper Doppler used the analogy of a ship sailing on the ocean to explain the phenomenon (Eden, 1986). Thus a ship sailing toward a wave source encounters more waves per unit time than a ship at rest, and a ship sailing away from a wave source encounters less waves per unit time than a ship at rest. Doppler used several different examples of astronomical data to support his theory, all of which were later shown not to be due to the Doppler effect. Nevertheless, his formulation for sound waves was correct (Eden, 1986).

The first experimental verification of the Doppler effect was made by the Dutchman Christoph Buys Ballot (White, 1982). Buys Ballot used a locomotive and flatcar loaned from the Dutch government, horn players, and musically trained observers in his experiments (Eden, 1986). Horn players on the flatcar and beside the track were asked to play the same note as the locomotive pulled the flatcar at a speed of forty miles per hour. As the flatcar passed the stationary horn players and observers the Doppler effect for sound waves was confirmed: the apparent pitch of the flatcar note was a half note higher than the stationary note on approach of the flatcar and a half note lower on recession. It was not until the turn of the century that the optical Doppler effect was experimentally confirmed (White, 1982).

There are diverse non-medical applications of the Doppler effect. The previously mentioned laser Doppler anemometer (LDA) is used in engineering flow measurements requiring high spatial resolution and minimum disturbance of the flow field (Roberson and Crowe, 1980). Radar systems also employ the Doppler principle (Kock, 1973). The 'Big Bang' expanding theory of our universe relies on the demonstrated Doppler shifts in the light spectra of certain galaxies (White, 1982). The Doppler effect has enabled calculation of the rotation speeds of the sun, planets, and rings of Saturn (White, 1982). Aerial navigation, satellite tracking, control of thermonuclear reactions, and measurement of car speeds by police officers all rely on the Doppler effect (Eden, 1986).

Medical applications of the Doppler effect are chiefly concerned with the clinical evaluation of the cardiovascular system. An exception to this is the laser Doppler anemometer, which has been used in numerous *in vitro* model studies of arterial velocity fields (Bharadvaj *et al.*, 1982a; Ku *et al.*, 1985a, 1985b). While the LDA cannot be used *in vivo*, a different laser Doppler configuration is used to measure skin blood flow (Stein *et al.*, 1977; Nilsson *et al.*, 1980; Winsor *et al.*, 1989). In addition, Kajiya *et al.* (1981) have developed an invasive laser Doppler velocimeter using an optical fibre and catheter probe. This has been used to measure velocity waveforms in the left circumflex coronary arteries of anaesthetized dogs. Doppler

ultrasonic flowmeters are used extensively in clinical settings (see 'Hemodynamics and Atherosclerosis', above), as well as in fundamental hemodynamic studies (Greene and Hirstand, 1979; Hutchison and Karpinski, 1985).

The first Doppler ultrasonic blood flow-sensing device was used by Satomura (1957). This and other (Franklin *et al.*, 1961) early Doppler flowmeters were of the continuous wave, non-directional type. Thus their flow signals resulted from moving structures at all depths in the sound beam and they were unable to distinguish between forward and reverse flows. A qualitative directional Doppler flowmeter was developed by McLeod in 1967 (Baker *et al.*, 1978), and a quantitative version by Nippa *et al.* (1975). Between the latter two developments pulsed Doppler ultrasonic velocimeter (PDUVM) technology emerged (Baker, 1970). By transmitting and receiving discrete pulses of sound this new device was able to detect blood flow at specific, selectable locations along the ultrasonic beam. The most recent developments in Doppler flowmeter technology are the widespread clinical use of duplex scanners in the diagnosis of arterial disease (see 'Hemodynamics and Atherosclerosis' above) and the use of multigated pulsed Doppler velocimeters for the rapid acquisition of arterial velocity profile data (Reneman *et al.*, 1986). The former device was pioneered by Barber *et al.* (1974), and the latter by Baker (1970).

The PDUVM operates as follows. A pulsed ultrasonic beam is directed into the vessel of interest, and the sound is

backscattered from each insonated red blood cell with a Doppler frequency shift, F_d , proportional to the cell's velocity, V . The actual equation used in this situation differs from that presented in elementary physics texts because the transducer emitting the ultrasound acts both as a 'source' and a 'listener':

$$F_d = 2(F_o)V\cos\theta/C \dots \dots \dots (1)$$

where F_o = transmission frequency

θ = angle of ultrasonic

beam with artery axis

C = velocity of sound

in medium

Derivations of this equation from first principles may be found in Khalifa (1978) and Aaslid (1986). In general, *in vivo* red cell velocities are such that the backscattered Doppler signal has a frequency shift which lies in the audio range. Furthermore, the finite size of the ultrasonic beam results in a spectrum of frequency shifts, ΣF_d , returning to the transducer. The breadth of this spectrum is partly dependent upon the range of velocities, ΣV , present in the intersection of the ultrasonic beam with the velocity field, and partly upon the transit time through the beam (Newhouse *et al.*, 1980; Garbini *et al.*, 1982). Thus the PDUVM does not

output point velocities. Instead, it outputs a range of velocities present in a fixed spatial region known as the sample volume. The characteristics of a given PDUVM sample volume are partly dependent upon transducer geometry, and partly upon the electronics of transducer excitation.

The electronic components of the PDUVM consist of a master oscillator, gating circuit, and quadrature phase detector (Zagzebski, 1986; Hartley, 1978; Jorgensen *et al.*, 1973). A schematic of the PDUVM electronics is depicted in figure 2. The master oscillator generates a reference frequency which is segmented into a train of pulses by the gating circuit. The pulse train excites the ultrasonic transducer (a piezoelectric crystal) to repeatedly emit bursts of ultrasound. These are backscattered from the flow field and sampled after a finite time interval which determines the distance between the transducer and its sample volume. The spatial position of the latter is controlled by the "range setting" of the gating circuit. The higher the range setting, the longer the sampling gate remains closed. When the gate is opened, the backscattered pulse signal received by the quadrature phase detector has travelled a distance proportional to the gate delay. The sign of the phase shift between the two quadrature signals is determined by the direction of red blood cell motion with respect to the ultrasonic axis. This directional information can be recorded by passing the Doppler signal through a frequency-offset circuit. A forward velocity signal will lie

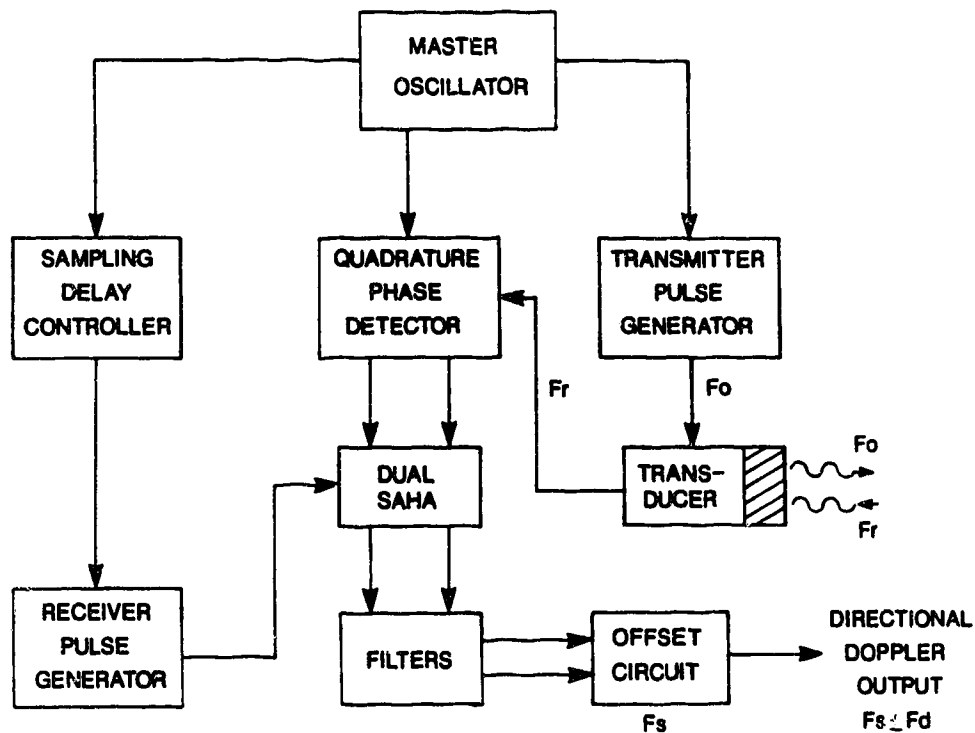


Figure 2. Schematic of the PDUVM electronics used in this thesis. SAHA = sample and hold amplifier. F_r = the backscattered Doppler signal which is the sum of the transmission frequency, F_o , and the Doppler shift, F_d . Also included is the offset circuit which adds an offset frequency, F_s , to the PDUVM quadrature output.

above the offset frequency while a reverse velocity signal will lie below the offset.

The methods of analysis of the PDVVM signal have evolved over time. The earliest Doppler flowmeters used zero crossing detectors to obtain a representative frequency from the Doppler output spectrum (Baker *et al.*, 1978). Zero crossing detectors continued to be used into the 1970's at which time their inaccuracies and limitations became well known (Reneman and Spencer, 1974; Lunt, 1975; Johnston *et al.*, 1977). Briefly, these inaccuracies and limitations are: the zero crosser cannot produce a linear output if the blood velocity profiles vary in time; the zero crosser is very sensitive to noise in the Doppler signal; the zero crosser frequency is reduced by artifactual signals produced by arterial wall motion; necessary filtering of the zero crosser output may interfere with the recording of transient velocity changes; and the zero crosser does not give meaningful output when blood flow is present in two directions at once. Furthermore, it has been found that zero crossing detectors present problems in the face of turbulent flow conditions (Spencer, 1986). These problems, and the loss of the complete Doppler spectrum when using zero crosser analysis, led to the development of frequency spectrum analysis techniques (Spencer, 1986). A number of choices for real time spectral analysis were available in the late 1970's: the fast Fourier transform (FFT); time compression analysis; multifilter frequency analysis; analog

processing of the original Doppler signal; and the phase-locked-loop method (Johnston *et al.*, 1977). In the early 1980's, the Autoregressive (AR) technique of spectral analysis was suggested as avoiding the problem of spectral leakage associated with the FFT method (D'Luna *et al.*, 1982). Nevertheless, the digital FFT has emerged as the predominant method of Doppler spectral analysis in current clinical settings (Beach and Phillips, 1984).

Despite its use in clinical settings, very few rigorous studies employing the PDUVM have been conducted in the post stenotic velocity field (Hutchison and Karpinski, 1985; Thiele *et al.*, 1983). Most of the information about the post-stenotic velocity field has been acquired with the hot film anemometer, laser Doppler anemometer, or by flow visualization. There is clearly a need to assess in detail the capabilities and limitations of the PDUVM/FFT method as a tool for exploring post-stenotic velocity fields. Moreover, the effect of variation of heart rate and pulsatility on the post-stenotic velocity field has not been investigated by this method. With the exception of the carotid bifurcation (Phillips *et al.*, 1983; Ku *et al.*, 1985b) there is without question a shortage of pulsed Doppler data on the velocity fields of arterial branches. Acquisition of such data is necessary to assist investigators interested in possible hemodynamic causes of atherosclerosis.

F. OBJECTIVES

The general purpose of this thesis was to use 10 and 20 MHz single-gated PDUVM's to explore the velocity fields associated with arterial disease. The purpose underlying this was to broaden the knowledge base used in the ultrasonic detection of arterial disease and to obtain further evidence in support of the role of hemodynamic factors in atherogenesis. Specific objectives related to the general objective fall into one of three categories: determination of limitations of the method; exploration of post-stenotic velocity fields; and exploration of velocity fields in the vicinity of aortic branches.

Determination of Limits of the Method

The accepted means of describing the spatial resolution of a PDUVM is to quote its sample volume dimensions (Morris *et al.*, 1973; Hoeks *et al.*, 1984). Therefore the first step taken towards determination of the limits of the PDUVM method was to measure the sample volumes of both the 10 and 20 MHz velocimeters. Next, the performance of the PDUVM in the simplest possible flow regime, steady laminar flow, was assessed. This was accomplished by comparing the theoretical velocity profile for steady laminar flow with velocity profiles measured by the PDUVM. The effect of different spectral parameters on the computation of laminar velocity profiles was also investigated.

Exploration of Post-stenotic Velocity Fields

Exploration of post-stenotic velocity fields was the most clinically oriented objective of this thesis, since the diseased artery typically has a stenotic geometry. The first step taken was to determine the limitations of the PDUVM method in the simplest situation - when the flow upstream of the stenosis was steady. Again a comparison was made between velocity profiles measured with the PDUVM and the actual velocity field determined by alternate means. In this case flow visualization was used to determine the actual post stenotic velocity field. A second objective was to investigate the type of post-stenotic flow regimes that were identifiable with the PDUVM when the flow upstream of the stenosis was pulsatile. Initially, the pattern of PDUVM velocity profiles downstream of different model stenoses was determined. Later, the correspondence between centrestream PDUVM spectral waveforms and the visualized post-stenotic velocity field at different times in the pulse cycle was determined. Next, the question was asked: how do PDUVM spectral waveforms vary with position of the sample volume in the post-stenotic velocity field? This was the sort of question addressed by Phillips *et al.* (1983) and Ku *et al.* (1985b) with respect to the carotid bifurcation. But to our knowledge it has not been investigated post-stenotically with a PDUVM. Initially, the influence of radial and axial sample volume position on the post-stenotic PDUVM spectral width under conditions of steady upstream flow was

investigated. Later, the effect of variation of pulse rate and pulsatility on centrestream PDUVM spectral width at a series of axial locations downstream of model stenoses was investigated.

Exploration of Velocity Fields in the Vicinity of Aortic Branches

Direct evidence on the role of hemodynamics in the initiation and/or progression of atherosclerosis can only be obtained by *in vivo* experiments. Since the major branches of abdominal aorta are frequently subject to atherosclerotic disease (Spain, 1966; Wesolowski *et al.*, 1965), and since there are only limited reports of *in vivo* pulsed Doppler investigations at these sites (Miller *et al.*, 1972), it was decided that a major objective of this thesis would be a detailed exploration of velocity fields near such branches in the anaesthetized dog. Specifically, the cranial mesenteric, left renal, and right renal artery branch sites were selected for PDUVM investigation. Because variation of physiological parameters such as branch flow is very difficult in the anaesthetized animal, another objective was to supplement the *in vivo* experiments with experiments in a cast-derived model of one of the *in vivo* branch sites. The effect of variation of branch flow on the model velocity field was investigated both under steady and pulsatile flow conditions.

II. MATERIALS AND METHODS

A. SAMPLE VOLUMES OF 10 AND 20 MHZ PDUVM'S

The sample volumes of one 20 MHz and one 10 MHz PDUVM transducer were determined by the moving string technique (Walker *et al.*, 1982). Each transducer was mounted in a micromanipulator at an angle of 60 degrees with respect to the horizontal. To obtain a Doppler signal, each transducer was directed at a loop of 4-0 (0.2 mm diameter) surgical silk thread rotating in the horizontal plane. The thread was tightly strung about two pulleys mounted in an acrylic tank. Thread rotation was produced by linking one of the pulleys to an axle driven by a DC motor. To provide an environment suitable for ultrasonic transmission the acrylic tank was filled with distilled water to a level where both the thread and transducer were immersed and the sides and bottom were lined with sound-absorbing foam.

The Doppler signal returning from the moving thread was passed through a Bruel and Kjaer type 2021 heterodyne filter and recorded on standard EKG tape using a Statham SP2002 recorder. The appropriate thread focussing frequency was determined by the Doppler shift equation to be 4 kHz. This was based on a physiological red cell velocity of 60 cm./sec. in a vessel insonated with a 10 MHz PDUVM, assuming a sound velocity of 1540 m./sec. Focussing was achieved by adjusting the DC motor speed so that the signal peak occurred at 4 kHz on a Bruel and Kjaer type 1025 Automatic

Vibration Exciter Control coupled to the Heterodyne filter.

For the 20 MHz transducer, sample volume intensity profiles were determined as follows. The PDUVM range was successively set at 2.5, 3.7, 4.9, 6.1, and 7.3 mm and the probe descended upon the moving thread until a maximum signal was produced. After focussing, vertical and horizontal signal profiles were obtained at each range setting by moving the sample volume across the thread with the range gate and horizontal manipulator, respectively. The resulting signal profiles were used to make signal intensity versus sample volume position plots. The plot widths at the 50 percent of maximum intensity level were measured and used as estimates of the axial (length along sound beam axis) and horizontal (diameter) sample volume dimensions at each range location. At each range gate location fourteen plot widths were averaged to obtain a measure of sample volume length and diameter. The 10 MHz transducer sample volume dimensions were determined in the same way, except that the range settings were extended further and fewer plot widths (ten) were used in the averaging. The range settings were 2.8, 3.9, 5.1, 6.3, 7.5, 8.7, and 9.9 mm. For both transducers the sample volume dimensions were averaged over all the range settings to yield a summary length and diameter.

B. STEADY LAMINAR FLOW IN VITRO

The Cardiovascular Model

A cardiovascular model (figure 3) was constructed and used to investigate the velocity and spatial resolution of both the 10 and 20 MHz velocimeters under conditions of steady laminar flow. The model incorporated a steady flow, tygon tubing version of the circuit used by Chapman and Charlesworth (1983) and a working fluid and test section similar to that of Greene and Hestand (1979). Specifically, the test section consisted of thin - walled dialysis tubing, which is known to transmit Doppler ultrasound with minimum refraction (Peronneau *et al.*, 1977). The dialysis tubing (Spectrapor no. 4) had a manufacturer rated dry wall thickness of 0.051 mm. The wet wall thickness using calipers was 0.015 cm. Depending on the amount of axial stretch in the test section, the wet tube diameter varied from 5.4 to 5.5 mm. The tubing was immersed in a 0.9 percent NaCl bath to facilitate ultrasonic coupling between PDUVM transducers and the measured velocity field.

The circulating fluid consisted of a cellulose - seeded mixture of glycerol (36.7 percent by mass) in distilled water. The mixture had a dynamic viscosity of 3.1 centipoise when measured in a Brookfield LVF viscometer with UL adapter. The mixture's density was found to be 1.09 g./ml. by measuring the mass and volume of a representative sample. The speed of 3.8 to 19.2 MHz sound in 36.7 percent

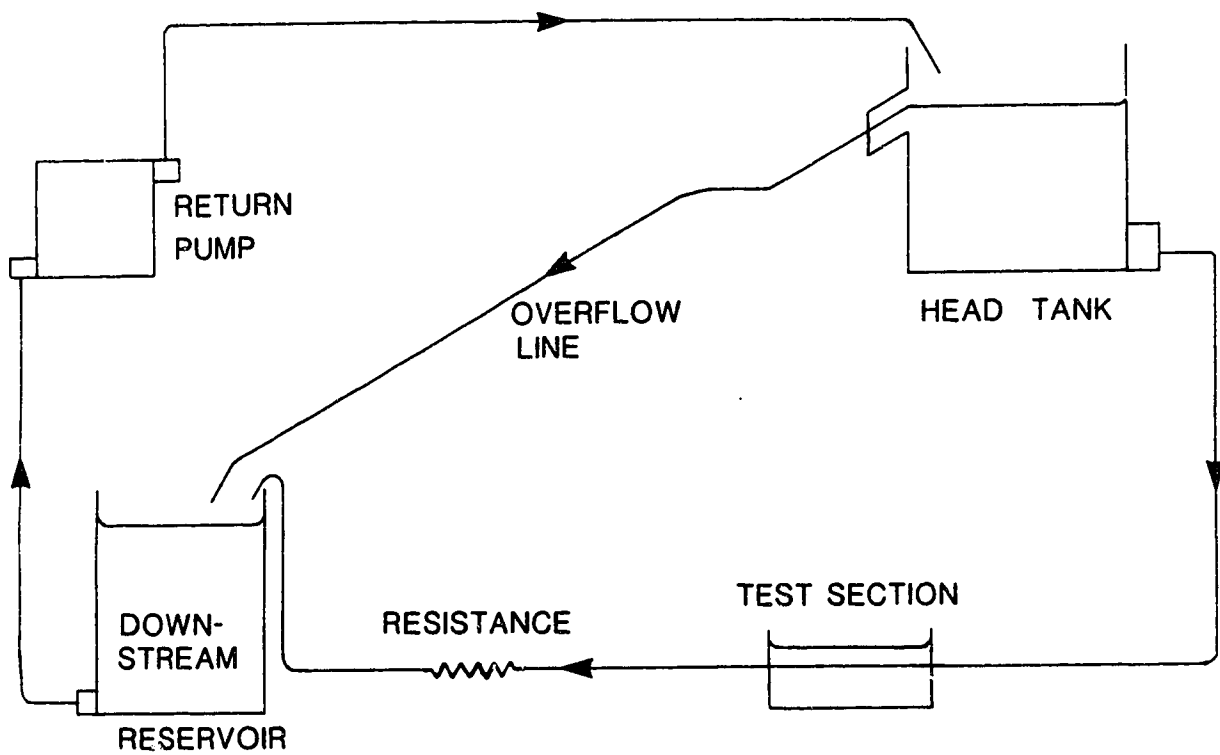


Figure 3. Schematic of the steady flow cardiovascular model. PDUVM sampling was conducted in the test section bath.

glycerol/water is reported to be 1571 meters per second (Willis, 1947). This was taken as the value of the 'C' parameter in the *in vitro* applications of the Doppler shift equation. In later *in vivo* experiments the parameter value used was 1540 m./sec.

Cellulose seeding was accomplished in two steps. First, microcrystalline cellulose (Sigma no. 20) was added to the glycerol/water mixture to a concentration of 0.56 percent by mass. The solution was then vacuum - filtered (Whatman no. 54 paper) to remove particles larger than 20 micrometers in diameter. This ensured that the PDUVM - measured velocity profiles would not be distorted by the effects of high sedimentation rates or large particle to tube diameter ratios. PDUVM measurements carried out in a vertically oriented tube suggested that sedimentation was not a problem in the more convenient horizontal arrangement of the test section. Electromagnetic stirrers in the head tank and downstream reservoir were used to keep the cellulose concentration uniform throughout the model.

To maintain a constant pressure head the return pump was set to slightly exceed the head tank outflow; the excess flow was shunted to the downstream reservoir by the overflow path. The flow rate through the test section was determined by the value of a variable downstream resistance and the height of the head tank above the test section. The downstream resistance was successively increased by inserting short segments of concentric tygon tubing, after

the method of Hay (1976). Four different volume flow rates were generated using the tygon resistors and measured by timed collection into graduated cylinders (Table 1). The corresponding Reynolds numbers were calculated using the equation:

$$Re = 4\rho Q/\pi D_o\mu \dots\dots\dots(2)$$

- where Q = volume flow
 ρ = fluid density
 D_o = tube diameter
 μ = dynamic viscosity

To ensure laminar flow in the test section, the Reynolds numbers (Table 1) were restricted to 1200 or less, and the entrance and test section geometry were maintained uniformly cylindrical and smooth. To ensure fully developed flow, an entrance length, L, of 84 cm. was used. Given the above maximum Reynolds numbers, Re, and a maximum test section radius, Ro, of 2.75 mm., this entrance exceeded generously the minimum obtained from the entrance equation quoted in McDonald (1974):

$$L = 0.08(R_o)(Re) \dots\dots\dots(3)$$

REYNOLDS NUMBER (Re)	VOLUME FLOWRATE (ml/sec)	MEASURED DIAMETER (mm)
462	5.68	5.5
686	8.28	5.4
848	10.23	5.4
1142	13.78	5.4

Table 1. Laminar flow test section Reynolds numbers and the volume flow rates and tube diameters from which they were calculated.

Experimental Protocol

Each experiment began with the measurement of circuit volume flow and tube diameter at the velocity sampling site. These measurements were fed into a minicomputer (DEC, LSI-11-2) for calculation of the theoretical velocity profile, $V(r)$, for steady, fully developed, laminar flow (Roberson and Crowe, 1980):

$$V(r) = V_{\max}(1-(r/R_o)^2) \dots \dots \dots (4)$$

where $V_{\max} = 2Q/\pi(R_o)^2$

and r = tube radial position

Velocity profiles were then measured using the 10 and 20 MHz pulsed Doppler ultrasonic velocimeters. The sample volume of each PDUVM was range-gated through the mid-vertical plane of the dialysis tubing in increments of 0.4 mm along the ultrasonic axis. At each sampling point the PDUVM's quadrature outputs were passed through a frequency offset circuit which displaced the Doppler signal, F_d , according to the velocity sign of the scatterers (cellulose) moving within the sample volume. Forward moving scatterers resulted in a Doppler spectrum lying above the offset frequency, F_s , while reverse moving scatterers resulted in a spectrum lying below the offset. The shifted spectrum was fed into a digital spectrum analyzer (Angioscan, Unigon industries) and the FFT processor output stored in a

software array. Each sampled spectrum was analyzed to determine the mode and contour frequencies using the definitions and software of Hutchison and Karpinski (1985).

Calculation of Doppler Shift Frequencies and Spectral Widths

For the sake of completeness, the calculation of the mode and contour frequencies of the Doppler signal used by Hutchison and Karpinski (1985) is briefly described here. Also described is the calculation of the mean Doppler frequency since it was used in addition to the mode in the determination of laminar velocity profiles. The mode Doppler frequency was calculated as that frequency with the highest amplitude in the Doppler spectrum (figure 4). The upper and lower contours were calculated as those frequencies respectively above and below the mode with amplitudes 8 decibels down from the mode amplitude. The mode and contours were stored on computer discs for subsequent analysis. The low contour to upper contour band width was used in the computation of the spectral mean. In particular, an arithmetic mean of the frequencies lying between the upper and lower contours was computed. From the same set of frequencies the standard deviation was calculated by the usual formula involving the computed mean and the number of points. Like the mode and contour frequencies, the spectral mean and standard deviation were stored on computer discs for subsequent analysis. In the laminar flow experiments of this thesis both the spectral mode and spectral mean were

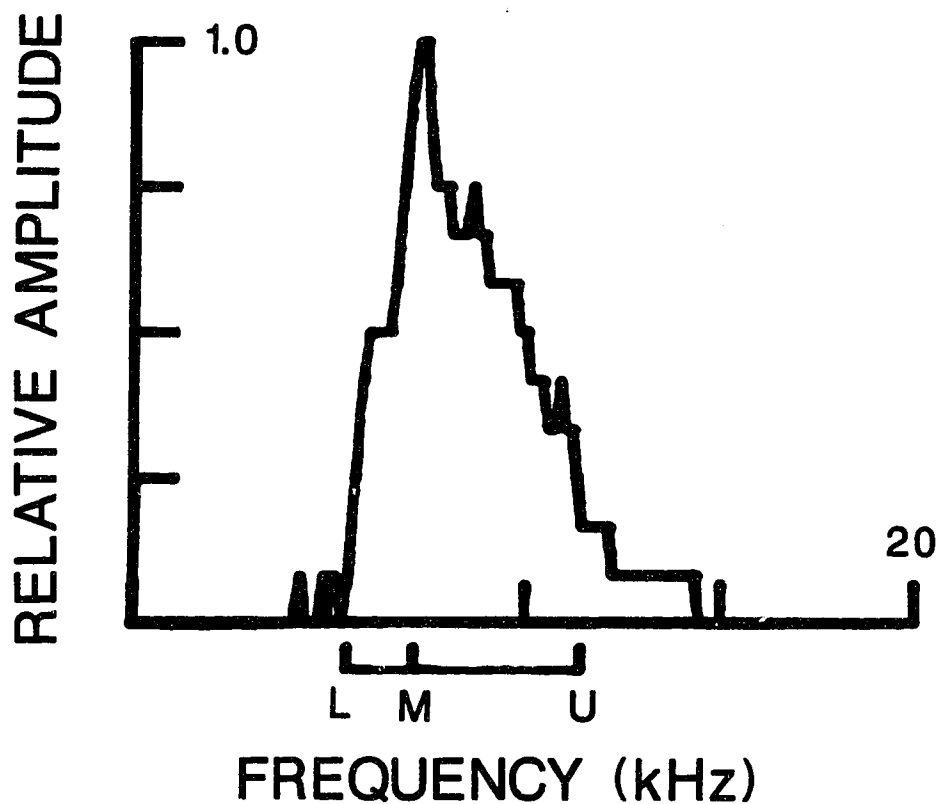


Figure 4. Typical Doppler spectrum illustrating the derivation of mode frequency and spectral contours. M - mode frequency: the frequency with highest amplitude. U - upper 8 decibel down contour: the frequency above the mode with amplitude 8 decibels down from the mode amplitude. L - lower 8 decibel down contour: the frequency below the mode with amplitude 8 decibels down from the mode amplitude.

used in the calculation of velocity profiles for comparative purposes. In all other parts the spectral mode was used to represent the Doppler frequency shift, since it avoids some of the disadvantages of the spectral mean in the detection of the true Doppler signal location (Langlois *et al.*, 1984). As illustrated in figure 5(a) the spectral mean and mode coincide if the Doppler signal spectrum is symmetric, e.g. a Gaussian distribution. In practice, the Doppler spectrum is often asymmetric (Langlois *et al.*, 1984). When this occurs the spectral mean and mode differ considerably, as shown in figure 5(b). Furthermore, in this situation it is the mode that correctly identifies where the bulk of the signal is located. This difference in the location of the mean and mode occurs whether or not the spectral mean is calculated from a filtered signal. Without some form of bandwidth filtering the raw spectral mean/standard deviation method is very sensitive to noise. This is demonstrated in figure 6 using a Doppler signal originating in the carotid artery of a dog. The mean/standard deviation spectral plot is of ragged appearance due to noise outside the spectrum of the Doppler signal. This interference is absent in the mode/8 dB contour spectral plot. The mean/standard deviation spectral method was used only in the laminar flow experiments and was bandwidth filtered using the mode's 8 dB upper and lower contours as cutoff points. The mode/contour width method was preferred as it better reflects the occurrence of asymmetry in the Doppler signal spectrum (Langlois *et al.*, 1984).

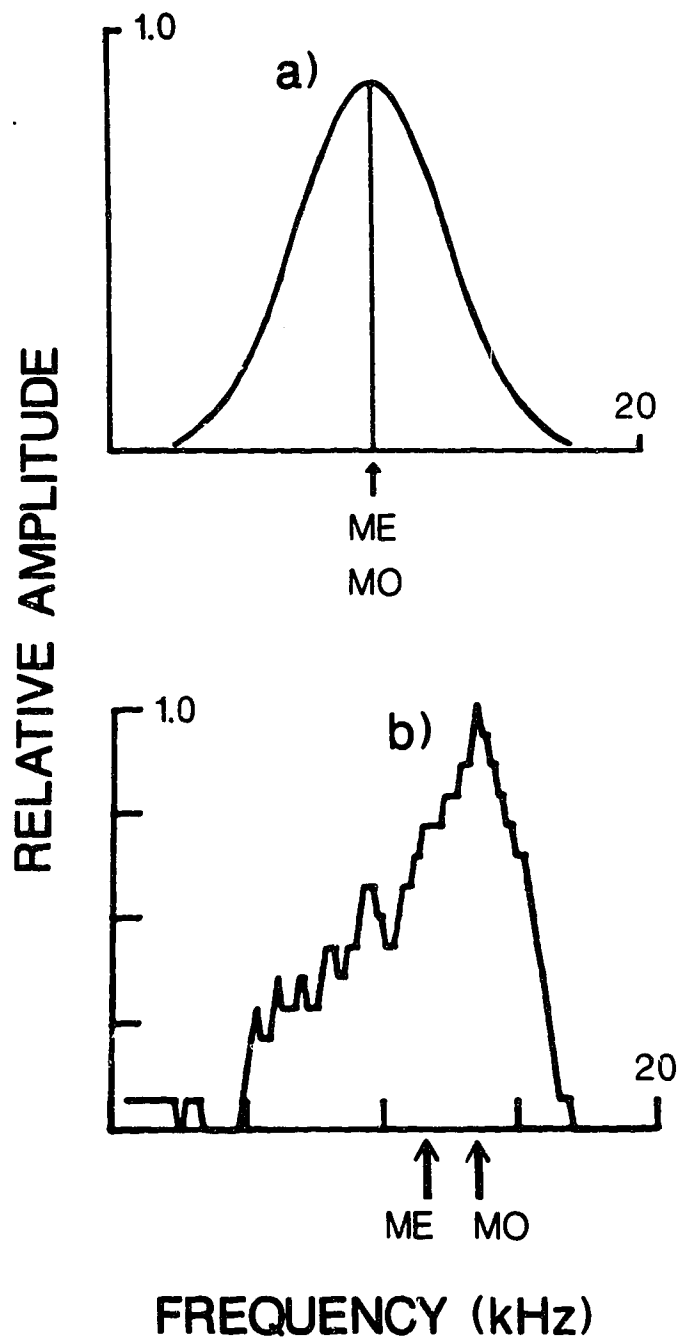


Figure 5. Demonstration of the coincidence or noncoincidence of the spectral mean (ME) and spectral mode (MO) depending on the shape of the Doppler signal spectrum. a) Coincidence occurs when the spectrum is symmetric. b) The mean and mode differ substantially when the spectrum is asymmetric.

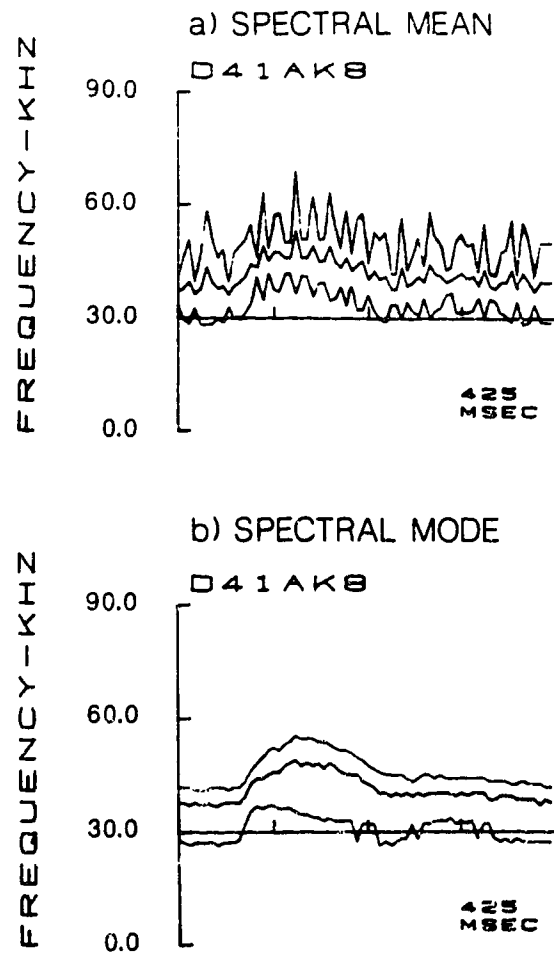


Figure 6. The difference between the raw mean and mode frequencies and corresponding spectral widths calculated from the Doppler signal originating in a dog carotid artery. a) The raw spectral mean surrounded above and below by its standard deviation is very noisy. b) The spectral mode surrounded by its upper and lower 8 dB contours is much smoother. Unpublished results of Drs. Hutchison and Karpinski of the University of Alberta. Used with permission.

Calculation of Laminar Velocity Profiles

To obtain laminar flow velocity profiles, $V(r)$, for both PDUVM's the mean and mode frequencies at each radial position, r , were substituted for the Doppler shift frequency, F_d , in a rearranged form of equation (1):

$$V(r) = C(F_d)/(2(F_o)\cos\theta)\dots\dots\dots(5)$$

where C = speed of sound in working fluid

F_o = transmission frequency

and θ = transducer-flow axis angle

A Hewlett Packard 7221S pen-plotter was used to plot the Doppler shift amplitude spectra and theoretical and PDUVM-measured velocity profiles.

C. POST-STENOTIC FLOW WITH STEADY UPSTREAM FLOW

Three acrylic stenoses, each 1 cm. long, and of internal diameters 0.19, 0.29, and 0.4 cm. were fitted to the steady flow test section entrance. Small diameter (5.5 to 6.0 mm) dialysis tubing was tied with 4-0 surgical thread around the lip of each stenosis so that the downstream section was accessible to the PDUVM. Three of the resistors used in the laminar flow experiments were used to vary the flow in the stenosed model. The combination of three stenoses and three flow rates allowed the investigation of nine different post-stenotic velocity fields. The 20 MHz

PDUVM was used to measure velocity profiles in the test section central horizontal plane starting at 0.44 cm. downstream of the stenoses. The PDUVM probe, and therefore the sample volume, was manually stepped across the tube diameter in increments of 0.5 mm using a micromanipulator. The same post-PDUVM instrumentation used in the laminar flow experiments was used to process and store the Doppler signal.

After velocity profile measurement flow visualization was used as an independent measurement of the post-stenotic velocity field. During the preparation of the model fluid it was not only seeded with cellulose by the same method as the laminar flow experiments, but also with light-reflecting tracer particles (Mearlmaid, Mearl Corp.). Mearlmaid seeding was accomplished as follows. First, 8 to 10 ml of Mearlmaid paste was added to 5330 ml of a glycerol (36.7 percent by mass) in water solution and allowed to mix thoroughly. The resultant Mearlmaid solution was allowed to stand for about 12 hours to promote sedimentation of the larger particles. After 12 hours, 300 ml were removed from the top, unseeded layer of the solution. Finally, this 300 ml was mixed into a fresh 5330 ml of cellulose-seeded model fluid used in the laminar flow experiments. Using the glass rod technique of Philpot *et al.* (1985) the test section central horizontal plane was illuminated with a 7 mW helium-neon laser. The flow patterns of the Mearlmaid particles were then photographed at 200 frames per second with a 16 mm

cinecamera (Locam) and high speed colour film (Kodak Ektachrome 7250, VNX 449). A schematic of the flow visualization apparatus is given in figure 7.

D. POST-STENOTIC FLOW WITH PULSATILE FLOW UPSTREAM

Rearrangement of the steady flow circuit and addition of a pulsatile unit, a control unit, and a downstream head tank allowed the investigation of post-stenotic velocity fields when the upstream flow was pulsatile. A schematic of the pulsatile circuit is given in figure 8. The working fluid used was similar to that of the steady flow experiments, but with the addition of sodium chloride to a concentration of 0.9 percent (w/v), to make the fluid sensitive to electromagnetic flow recording. To prevent algae growth 23 ml of the antiseptic fluid Halcyon (Halcyon Waterbed Inc.) was added. An electromagnetic flowmeter probe (Nycotron) inserted upstream of the test section was used to monitor the mean and instantaneous volume flow rates. The electromagnetic flowmeter signal was calibrated under conditions of steady flow by timed collection into a graduated cylinder. After calibration the circuit was switched to its pulsatile configuration and pulsatility (λ) was calculated using the formula:

$$\lambda = Q_p/Q_m - 1 \dots \dots \dots (6)$$

where Q_m = mean flow rate

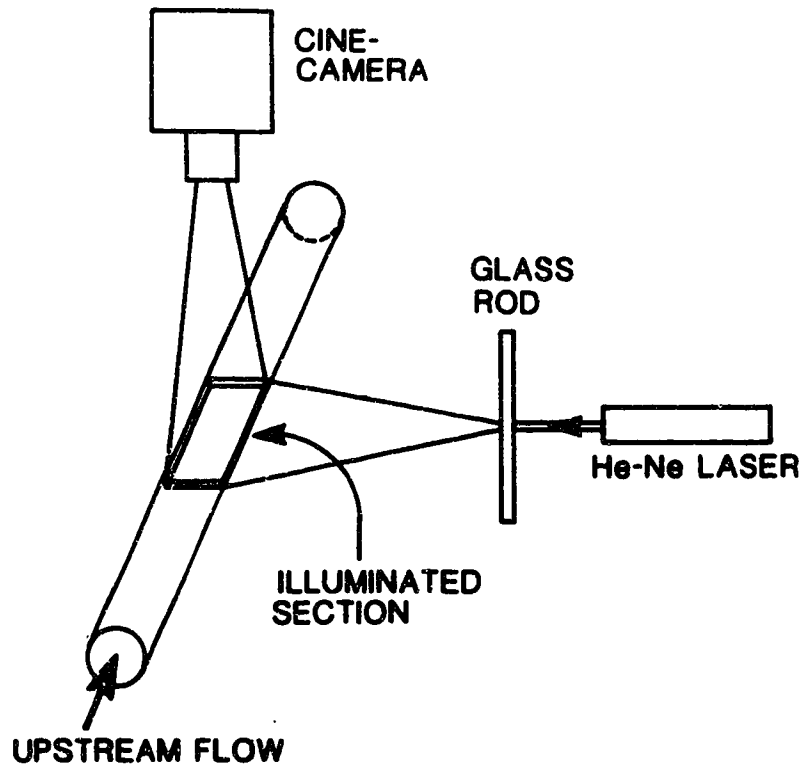


Figure 7. Schematic of the flow visualization apparatus used to reveal the actual post stenotic velocity field in the central horizontal plane of the test section dialysis tubing.

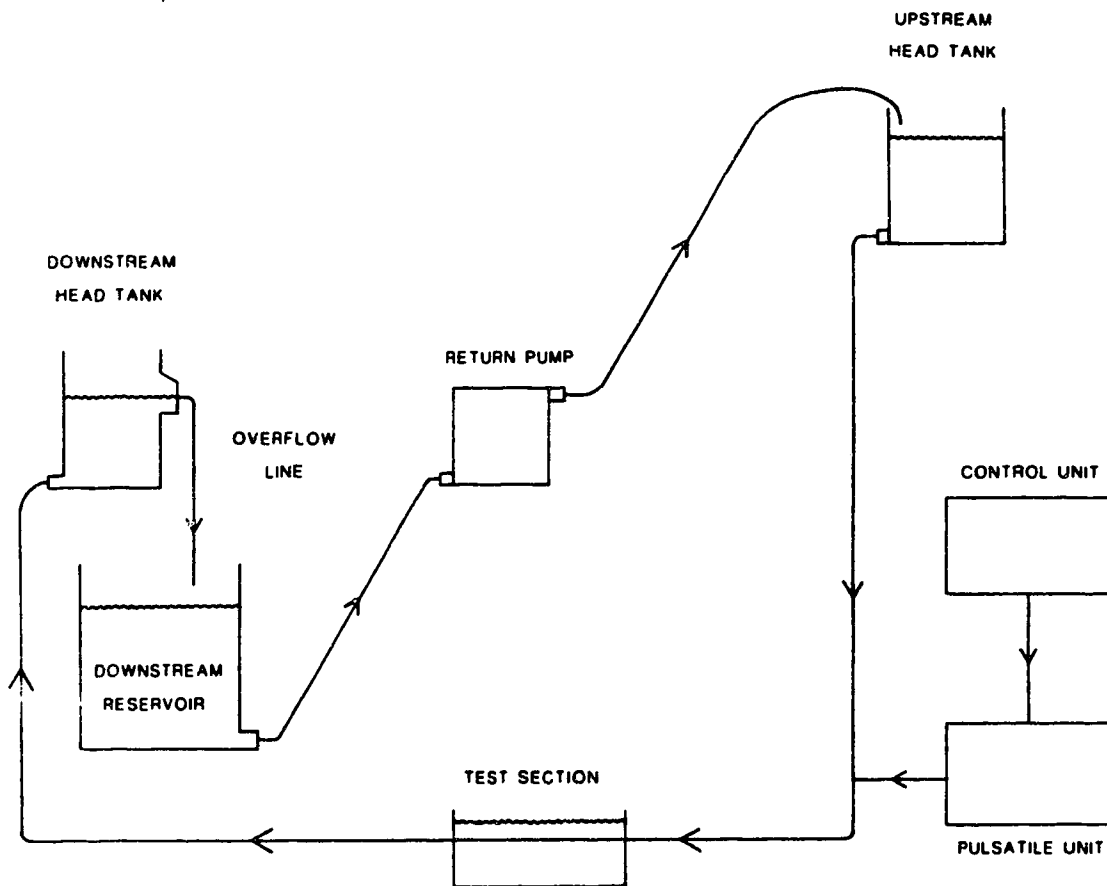


Figure 8. Schematic of the pulsatile cardiovascular model. This circuit was used for both pulsatile post-stenotic and pulsatile branch flow model studies.

Q_p = peak flow rate,

obtained from the instantaneous flow signal

The initial pulsatile unit consisted of a cylindrical vibrator (Derritron, VP4) inserted into the acrylic pressure chamber used by Hutchison (1974). The control unit consisted of a 100 ampere power amplifier externally driven by a sine wave originating in a Hewlett-Packard 3310A function generator. Pulsatility and pulse rate were determined by the control unit amplitude and frequency settings. In later experiments the pulsatile unit consisted of a cam-driven piston apparatus similar to that of Pelot (1981). Control of this pulsatile unit was achieved by turning off the power and manually adjusting cam amplitude and axle rotation speed. Specifically, the model pulsatility was determined by the amplitude of the waveform superimposed on the cam base circle and varied by using a series of plastic cams of different amplitudes. The cam outlines were calculated by an interactive computer (DEC, previously described) program and plotted with the previously described interfaced pen-plotter. An example of a sinusoidal waveform superimposed on a base circle is given in figure 9. Model pulse rate was determined by the rotation speed of the cam axle. This, in turn, was indirectly controlled by the rotation speed of a geared AC motor (Bodine Electric Co.). The cam and motor axles each had a pulley and the two pulleys were linked by a rubber belt. By increasing the

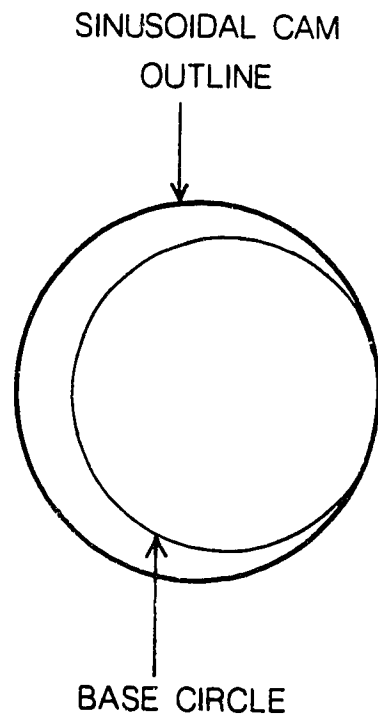


Figure 9. Outline of a sinusoidal cam used in the pulsatile flow experiments. Also shown is the base circle from which the cam was derived.

diameter of the motor axle pulley, and decreasing the diameter of the cam axle pulley, the cam rotation speed could be increased, and vice versa. A photograph of the cam-based pulsatile unit is given in figure 10.

For both pulsatile units the flow rate was controlled by the height differential between the upstream and downstream head tanks and a screw clamp resistor between the upstream head tank and the pulsatile unit.

Three main experimental protocols were followed. First, the flow fields 0.6 to 25.0 cm downstream of the previously used 1.9 and 2.9 mm acrylic stenoses were visualized using the light-reflecting particles and photographic technique of the steady flow experiments. Pulse rate was varied between 1.5 and 4 Hz, pulsatility between 0.24 and 1.05, and mean flow rate between 250 and 694 ml/minute. At some of the visualized axial locations the velocity field was sampled with the 20 MHz PDUVM for comparative purposes. As in the steady flow post-stenotic experiments, velocity profiles were recorded along the central horizontal plane of the post-stenotic tubing with sample volume increments of 0.5 mm. In these experiments the vibrator-based pulsatile unit was employed. In the second protocol the effect of pulse rate on the velocity field 0.6 to 15.0 cm downstream of the 2.9 mm stenosis was investigated. Initially, PDUVM spectra were recorded while the pulse rate was varied from 2.0 to 4.5 Hertz at a pulsatility of 0.42 and a mean flow rate of 330 ml/minute using the vibrator-based pulsatile unit.

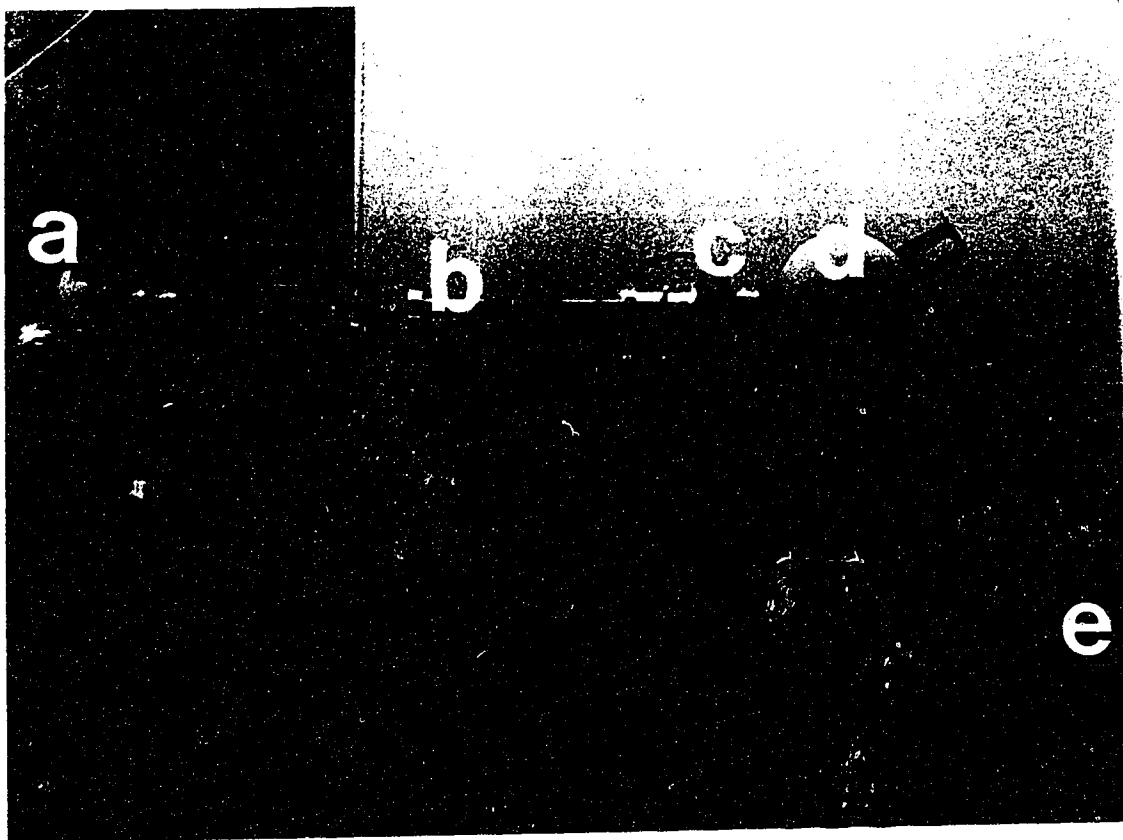


Figure 10. Photograph of the cam-based pulsatile unit used in pulsatile flow model experiments. a) Stroke chamber. b) Follower shaft. c) Sync signal microswitch. d) Plastic cam. e) Geared AC motor.

Later, PDUVM spectra were recorded while the rate was varied from 51 to 240 beats per minute (BPM) at a mean pulsatility of 1.78 and a mean flow of 292 ml/minute using the cam-based pulsatile unit. For both of these pulse rate protocols PDUVM velocity profiles were recorded along the central horizontal and central vertical planes at each axial location. The third protocol investigated the effect of pulsatility on the velocity field 0.6 to 15.0 cm downstream of the 2.9 mm stenosis. The pulsatility was varied from 0.7 to 2.0 while the pulse rate and mean volume flow were maintained at 105 bpm and 316 ml/min, respectively.

In the first two protocols the post-stenotic test section consisted of the same diameter dialysis tubing as in the steady flow post-stenotic experiments. In the third protocol it was found that the dialysis tubing collapsed at the highest pulsatility. Therefore, in these experiments the post-stenotic test section consisted of a 1/4 inch inner diameter rigid acrylic rod fitted over the stenosis with O rings. PDUVM transducer access to the test section was obtained via holes drilled in the central vertical plane of the rod at the required axial locations. Custom made rubber stoppers plugged the holes not filled by the PDUVM transducer. PDUVM spectra and derived velocity profiles were recorded only in the central vertical plane of the post-stenotic tubing. In this instance the sample volume increment was 0.6 mm along the ultrasonic axis.

In all three protocols the electromagnetic flowmeter signals were recorded on separate channels of a Gould 2400S chart recorder. The PDUVM quadrature outputs were recorded on the direct channels of a tape recorder (Gould no. 6500; ± 3 dB over 100 Hz to 150 kHz). When the vibrator-based pulsatile unit was used, the square sync output of the control unit was recorded simultaneously on an FM channel. This provided a periodic triggering signal necessary for subsequent computer sampling of the Doppler signal. When the cam-based pulsatile unit was used, the tripping of a microswitch mounted in the vicinity of the cam follower generated the sync signal to be recorded on the FM channel and required for sampling. A metal rod mounted perpendicularly on the follower tripped the switch once per cam cycle. The switch mount was variable through the use of a set screw, thus allowing for cams of different amplitudes. On playback, the PDUVM signals were processed through the same offset circuit and spectrum analyser as were used in the steady upstream flow experiments. Sampling of PDUVM spectra was triggered by the rising or falling edge of the FM channel sync signal. The spectra were stored on disc or in bank memory. Spectra having rise to rise intervals that differed by less than 10 percent were ensemble averaged. As in the previous post-stenotic experiments the spectral mode was used as the representative frequency in the Doppler shift equation, and the spectral width was calculated from the separation between the mode's 8 decibel down contours.

E. BRANCHED AORTIC FLOW *IN VIVO*

Velocity Field Measurement

In a series of experiments in anaesthetized dogs, pulsed Doppler velocimetry was used to map aortic velocity fields in the vicinity of abdominal branches, usually 0.5 cm downstream of the cephalic (cranial) mesenteric and left renal arteries. The entire cross-section of the aorta was mapped so that spectra from both centre-stream and off-centre locations were recorded using the 10 MHz PDUVM. This pattern of recording provided a grid of velocity waveforms. An example of such a grid recorded 3 cm downstream of a 42 percent diameter reducing stenosis in a dog common carotid artery is shown in figure 11. The distance between grid points, and therefore the sample volume increment, was 1.0 mm in the horizontal direction and 1.2 mm along the ultrasonic axis. The method of recording, playback, and sampling of the PDUVM output was the same as in the pulsatile post-stenotic experiments with the exception that the dog EKG was used instead of the control unit sync output.

To describe the velocity field more clearly velocities occurring at the same point in the pulse cycle were placed in a software array and an algorithm which developed a three dimensional cross-sectional velocity profile was applied. An example occurring 250 msec. after the EKG R wave for the same artery as in figure 11 is presented in figure 12. An

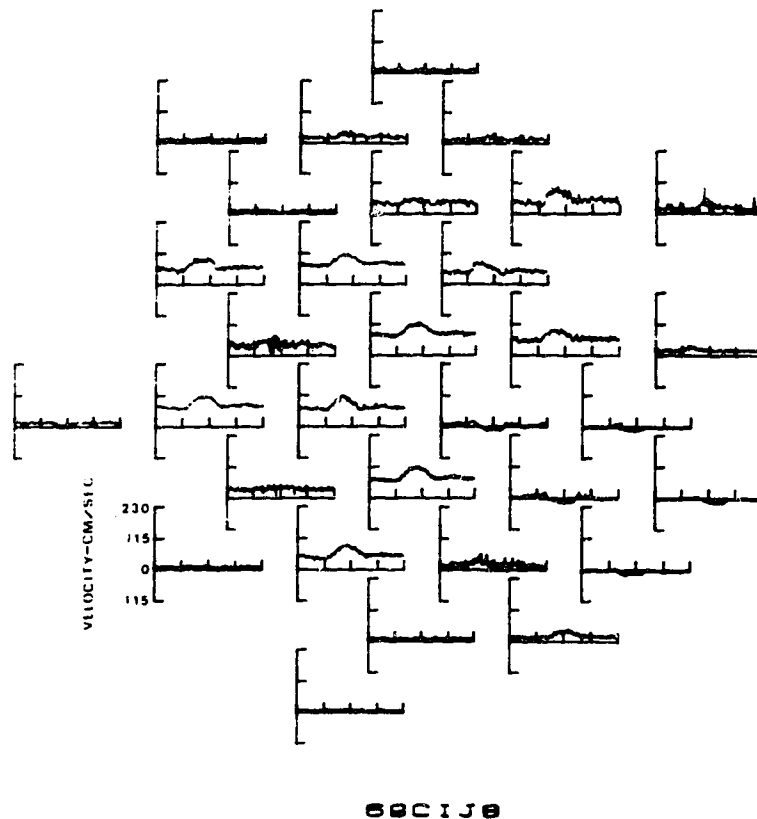


Figure 11. A grid of velocity waveforms developed from mode frequencies at 0.5 cm intervals 3 cm downstream of a 42 percent diameter reducing stenosis on a dog common carotid artery.

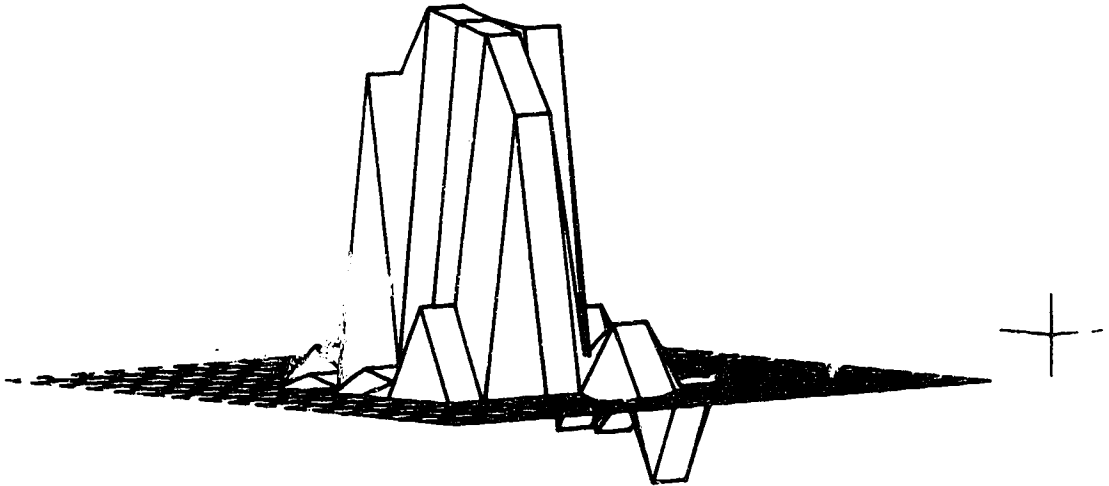


Figure 12. A three-dimensional velocity profile from 3 cm downstream of a 42 percent diameter reducing stenosis developed from the velocities 250 msec after the R wave of a grid of waveforms across the cross-section of a dog common carotid artery. The plane represents zero velocity: velocities below the plane are negative and above are positive.

asymmetric zone of recirculation typical of the post-stenotic velocity field is indicated by the negative velocities seen beneath the zero velocity plane. Another algorithm was applied to the array of velocities to develop corresponding aortic cross-sectional velocity contours. The algorithm asked for the number of contours (usually five to six) and constructed these by linear interpolation between the points of the velocity array. The maximum and minimum contour velocities were also input to the algorithm to determine the limits of interpolation. Velocity contours derived from the cross-sectional velocity profile of figure 12 are shown in figure 13. The asymmetric flow recirculation zone is clearly shown by the negative velocity contours in the right ventral (lower) region of the artery cross-section. In the diagrams of cross-sectional velocity contours a representative velocity waveform from the centre of the grid is plotted to indicate the timing of the displayed contours. In figure 13 this waveform has no negative component, while in figure 34 (results section) there is a negative component. This is because the transient zone of flow reversal encroaches on the mid-line in figure 34 but does not in figure 13.

Measurement of Turbulence

Spectral mode contours at the 8 dB level were plotted in conjunction with each velocity waveform to provide a measure of spectral width, but have not been reproduced here

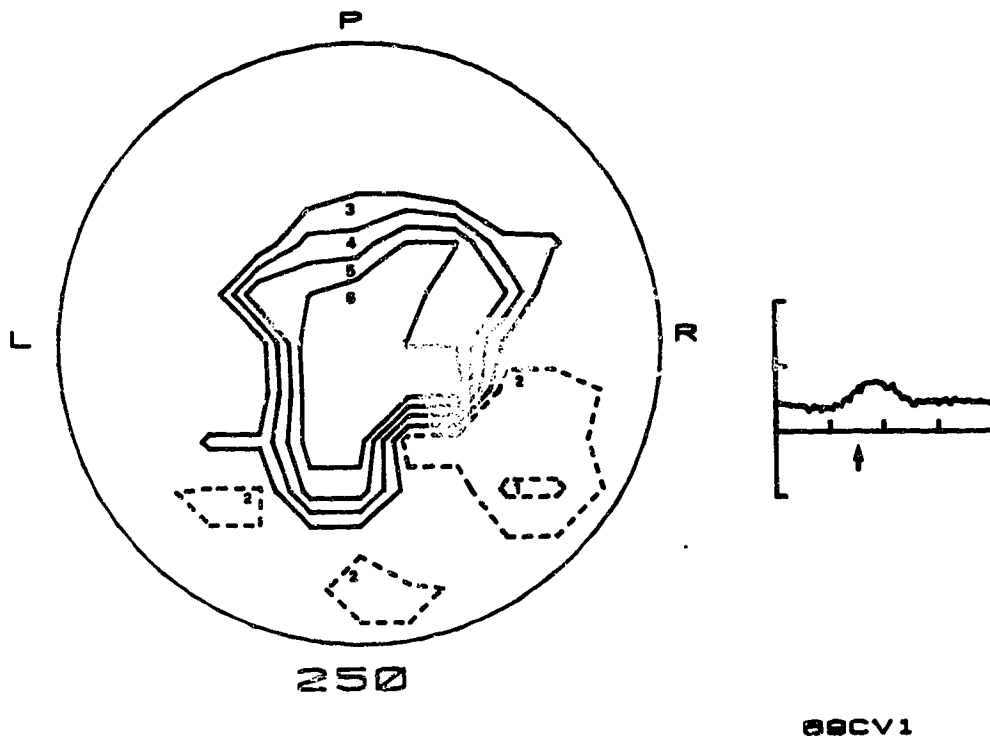


Figure 13. Cross-sectional velocity contours at 250 msec after the R wave (indicated by the arrow below the velocity waveform to the right) from 3 cm downstream of a 42 percent diameter reducing stenosis on a dog common carotid artery. Contour velocities are (1) -21.7, (2) -1.0, (3) 19.7, (4) 40.4, (5) 61.1, (6) 81.9 cm/sec. L: left, R: right, P: posterior (dorsal).

since no increased spectral broadening was apparent.

Experimental Protocol

Velocity contours were recorded in the above manner in 8 anaesthetized dogs 0.5 cm. downstream of the cranial mesenteric artery, in 6 dogs 0.5 cm. downstream of the left renal artery, and at a small number of other abdominal locations. Anaesthesia was induced using intravenous sodium pentobarbital (35 mg/kg) and maintained with halothane. All dogs were female and weighed between 15 and 35 kilograms. A respirator (Harvard Apparatus no. 607) controlled the rate and depth of respiration such that intermittent one minute periods of apnea were unaccompanied by changes in pulse rate, blood pressure, or local blood flow. Doppler recordings were made during the apneic periods when there was no movement of the PDUM probe due to respiratory excursions. The abdominal aorta was exposed through a midline laparotomy. In experiments involving the cranial mesenteric artery the diaphragm was incised to allow full exposure of the celiac and mesenteric arteries. A Nycotron electromagnetic flow probe was applied to the abdominal aorta downstream of the branches of interest and the intervening branches were ligated. Smaller Nycotron probes were also applied to the branches of interest to monitor the flow through them. Pulse rate, arterial blood pressure, and the above flow rates were recorded throughout the experimental period on a 4 channel dynograph (Beckman). Each

experiment was terminated by intravenous administration of potassium chloride. At that time a length of aorta containing the branches of interest was excised. A silicone rubber cast of the segment was made while its length and pressure were maintained at their *in vivo* values. Arterial dimensions were estimated from this cast using vernier calipers.

F. BRANCHED AORTIC FLOW *IN VITRO*

The silicone rubber cast of *in vivo* dog experiment 74 was used to make a flow-through acrylic mold of the aorta in the vicinity of the left and right renal artery branches. This particular cast was chosen because of the wide axial separation (1.8 cm) between the origins of the renal arteries which resulted in significant flow reversal *in vivo*. The rubber cast was suspended in a tube filled with unhardened acrylic resin. After the acrylic resin had hardened, the cast was pulled out of it, leaving a flow-through mold with the exact *in vivo* luminal geometry. The ventral hemispheric surface of the mold immediately downstream of the right renal artery was machined down until the wall was thin enough (approximately one mm) to conduct pulsed ultrasound with minimum refraction. The left and right renal artery branches were also isolated by machining to facilitate fitting them with outflow tubing. The flow through mold was then inserted into the previously described pulsatile circuit and surrounded with a water bath to allow

ultrasound coupling between the PDUVM transducer and the *in vitro* flow field. A photograph of the branch model and the cast from which it was derived is given in figure 14. In preparation for pulsed Doppler sampling the pulsatile circuit was filled with a fresh batch of fluid having the same composition as that used in the pulsatile post-stenotic experiments.

Initially, steady flow experiments were carried out by deactivating the pulsatile unit. Aortic flow was recorded with an electromagnetic flowmeter calibrated in the same way as the pulsatile post-stenotic experiments above. Renal branch flow was measured by timed collection into a graduated cylinder. Aortic flow was set at 1197 ml per minute with a screw clamp, left renal flow was set at zero ml per minute with a screw clamp, and right renal branch flow was varied from zero to 56 percent of aortic flow with the aid of screw clamps and outflow tubing of different diameters. The right branch flow was returned to the model circuit via the downstream reservoir. For each right branch flow rate the 10 MHz PDUVM was used to record a grid of velocity waveforms 0.5 cm downstream of the right renal branch by the same methods used in the *in vivo* experiments.

To achieve pulsatile flow the cam-based pulsatile unit of the post-stenotic experiments was activated and set at a frequency of 105 beats per minute. Mean aortic flow was maintained between 327 and 406 ml per minute, peak aortic flow was maintained between 1197 and 1217 ml per minute, and

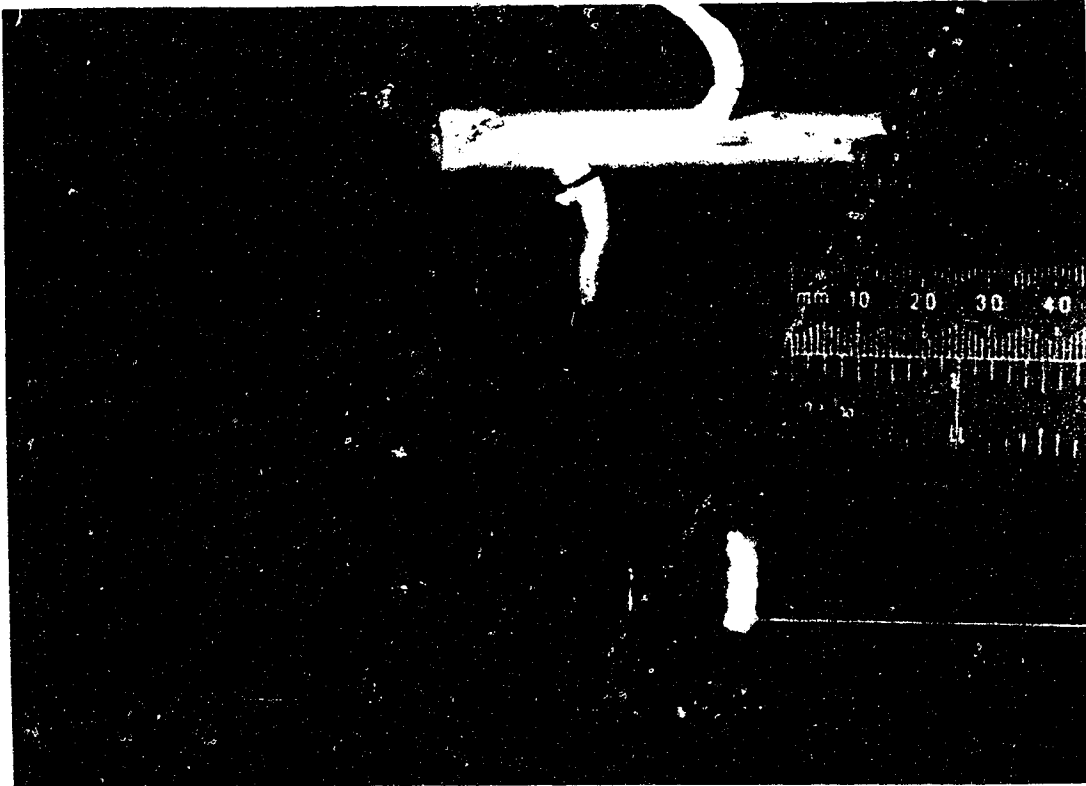


Figure 14. Photograph of the ventral surface of the acrylic branch model (below ruler) used in the *in vitro* branch experiments. Also shown is the ventral surface of the silicone rubber cast (above ruler) from which the acrylic model was made. The caudal ends of the aortae are situated on the righthand side of the photograph.

left renal branch flow was kept at zero ml per minute. Right renal branch flow was then varied from zero to 48 percent of mean aortic flow. At each right branch flow rate the 10 MHz PDUVM was used to record a grid of velocity waveforms at the same axial location as in the steady branch experiments. As was done in the pulsatile post-stenotic experiments, the sync signal from the pulsatile unit was recorded for the purpose of triggering the computer sampling of the recorded PDUVM signal once every pulse cycle.

III. RESULTS

A. SAMPLE VOLUMES

The variation of the two PDUVM mean sample volume diameters with range gate setting is depicted in figure 15. The 20 MHz PDUVM sample volume mean diameter clearly increased with increasing range gate position while the 10 MHz PDUVM mean diameter decreased in the same direction. Because of these opposing trends the difference in mean diameters was greatest at the nearest ranges (2.5 mm - 20 MHz, 2.8 mm - 10 MHz) and least at ranges of 7.3 mm (20 MHz) and 7.5 mm (10 MHz). An explanation of the differing behaviours of the 20 and 10 MHz PDUVM sample volume diameters with range gate position will be given in the discussion section of this thesis. The 20 MHz PDUVM overall mean sample volume length along the ultrasonic axis was 0.69 mm and the overall mean diameter was 0.97 mm. The 10 MHz PDUVM overall mean sample volume length along the ultrasonic axis was 0.93 mm and its overall mean diameter was 1.09 mm. Thus the 20 MHz PDUVM had a smaller sample volume than the 10 MHz PDUVM.

B. VELOCITY PROFILES: LAMINAR AND POST-STENOTIC FLOW

Steady Laminar Flow

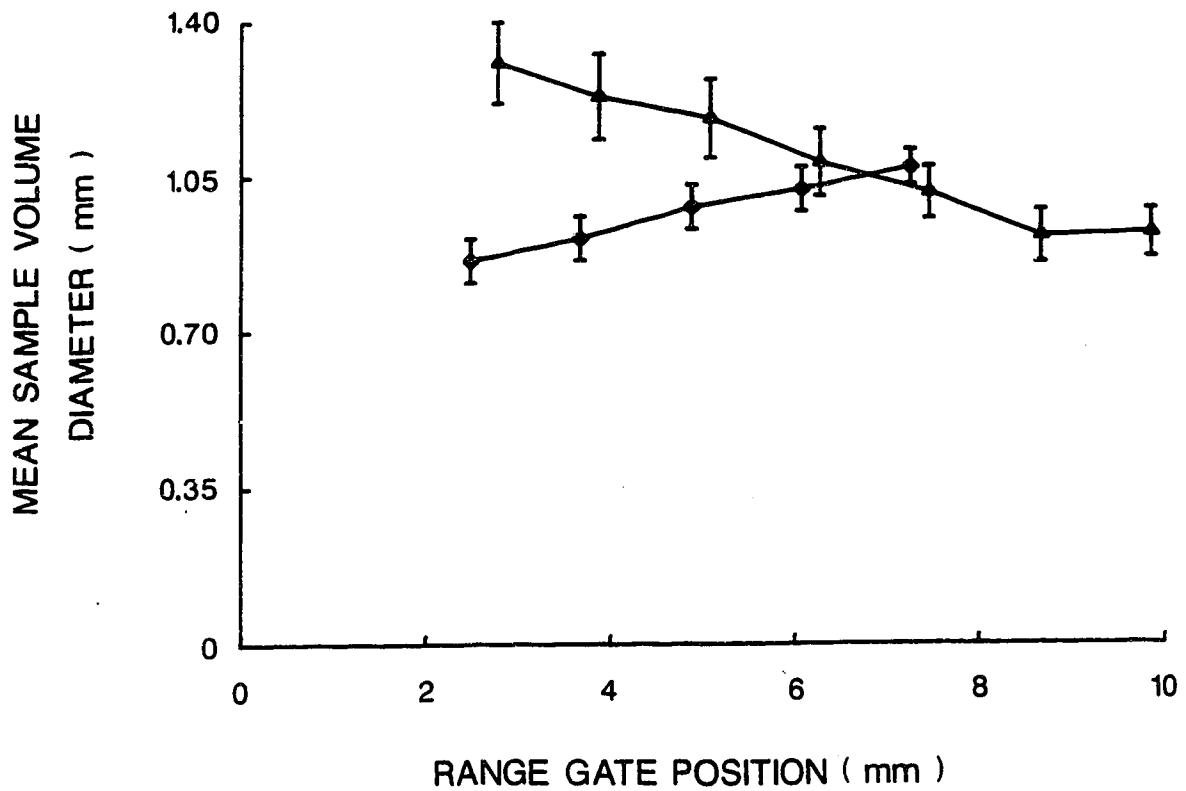


Figure 15. The variation in PDUVM sample volume mean diameter with range gate position. The bars indicate standard errors of the mean at each point. 20 MHz PDUVM - diamond, $n = 14$ at each point. 10 MHz PDUVM - triangle, $n = 10$ at each point.

20 MHz PDUVM

Figure 16 is a composite diagram showing 20 MHz PDUVM spectra, recorded from the model under conditions of steady laminar flow at a Reynolds number of 686, superimposed on a frequency profile, i.e. a mode frequency versus radial position plot. The plotted increase in mode frequency towards centrestream is represented by a shift of the spectra to higher frequencies. At each laminar flow Reynolds number velocity profiles were computed from the corresponding 20 MHz PDUVM-measured frequency profiles (such as that in figure 16) using equation (5). Figure 17 depicts the velocity profiles obtained when the spectral mode was used as the Doppler shift frequency in the equation. Each PDUVM profile is accompanied by the theoretical velocity profile for the same Reynolds number. Figure 18 presents velocity profiles calculated with the spectral mean as the representative Doppler frequency, and compares them with the corresponding theoretical profiles, as in figure 17. The spectral mean profiles were clearly smoother than the mode profiles, the latter being particularly noisy in the distal (right) half of the tube. Both mode and mean-based velocity profiles were similar in three respects. First, the profiles were all generally parabolic in shape, as would be expected in steady laminar flow. Second, the tube diameters, determined from the intercepts of the Doppler profiles

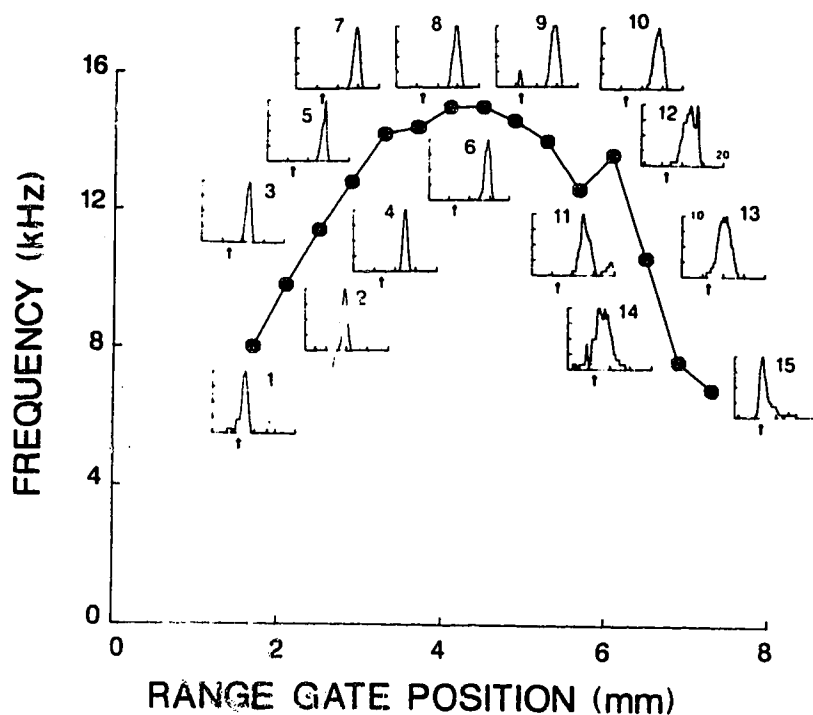


Figure 16. 20 MHz PDUVM mode frequency profile across the unstenosed tube at a steady flow Reynolds number of 686. The spectra from which each mode frequency was derived are superimposed. For each spectrum the ordinate is relative amplitude, normalized to each maximum. The abscissa is frequency in kHz, with a 20 kHz maximum. The offset frequency of 6 kHz (zero velocity) is indicated by an arrow on each spectrum.

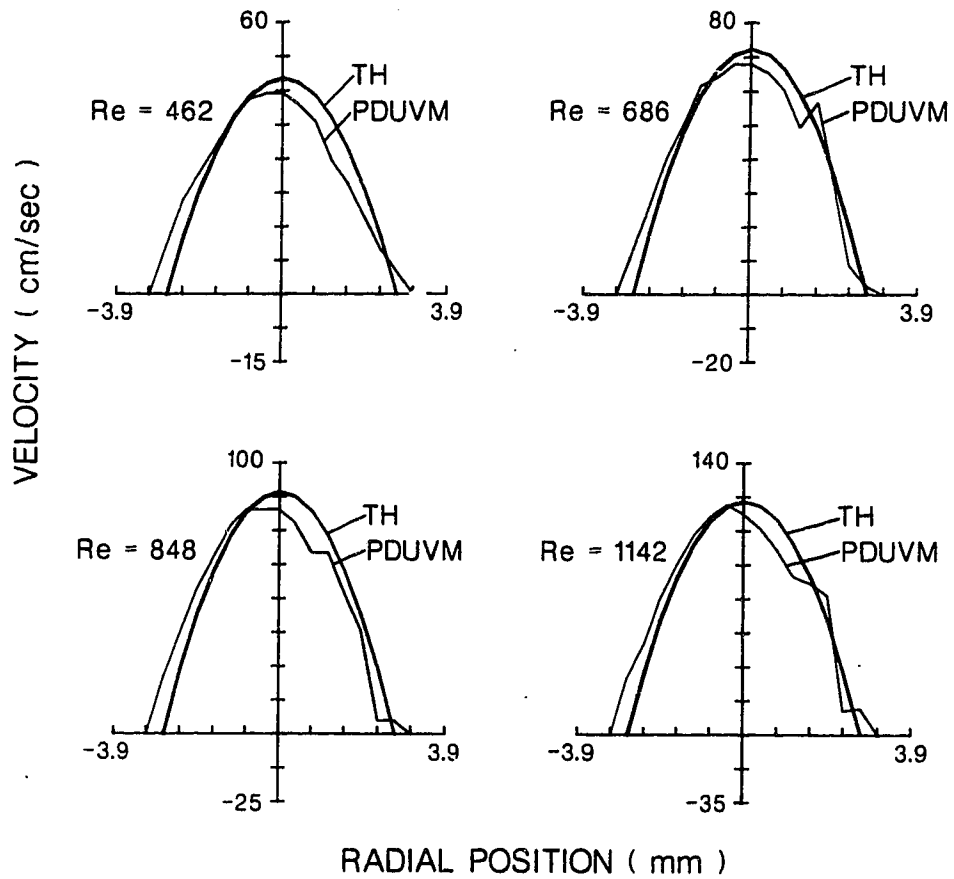


Figure 17. Steady flow velocity profiles recorded with the 20 MHz PDUVM and based on the spectral mode. Re - Reynolds number. TH - theoretical velocity profile.

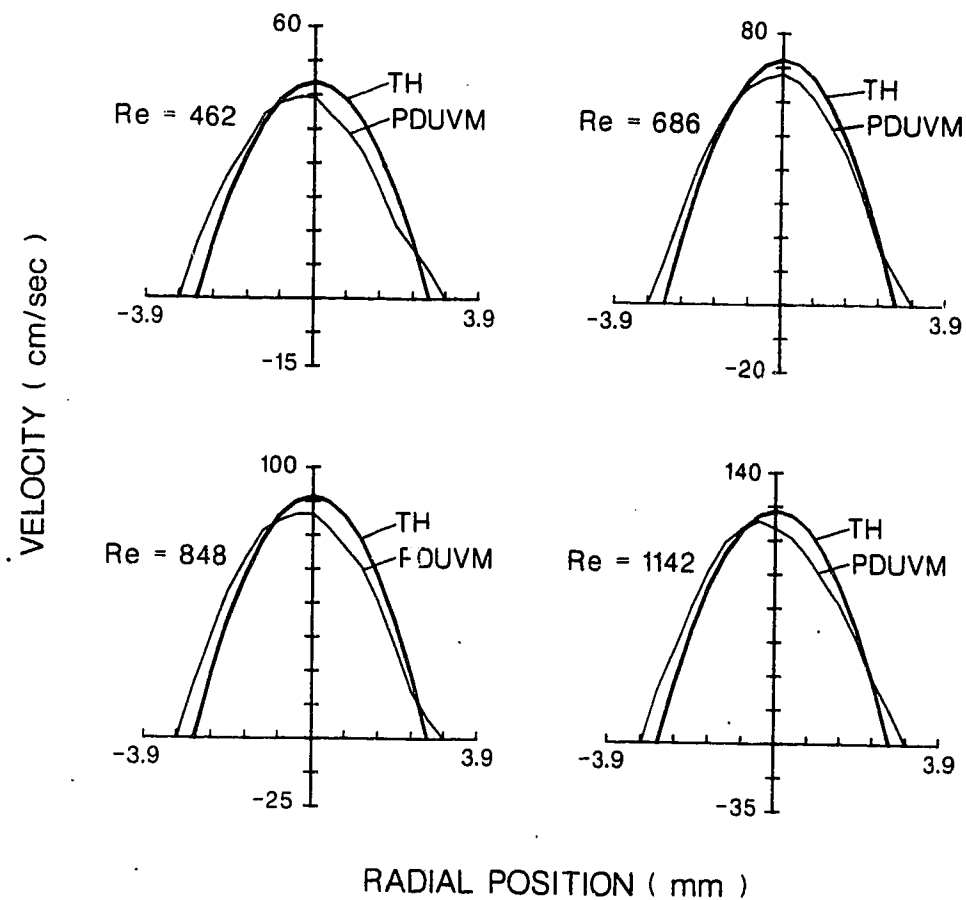


Figure 18. Steady flow velocity profiles recorded with the 20 MHz PDUVM and based on the spectral mean. Re - Reynolds number. TH - theoretical velocity profile.

along the radial position axis, consistently exceeded the real tube diameter, determined from the intercepts of the theoretical velocity profile. Third, the maximum Doppler velocity consistently underestimated the theoretical maximum. The latter observation is quantified for the spectral mean-based velocity profiles in table 2. The Doppler maximum velocities were obtained by fitting all 15 points of the velocity profile to a second order curve symmetric about the velocity axis and extracting the velocity intercept of the regression equation. The theoretical velocities were obtained from the measured tube flow and diameter as described in the methods section (equation (4)). As shown in the table the 20 MHz Doppler measured velocity maximum underestimated the theoretical velocity maximum by 7.2 to 10.7 percent. This is due to the fact that the single frequency PDUVM profile is a distorted 'image' formed by the space convolution of the PDUVM sample volume with the true velocity profile (Jorgensen *et al.*, 1973). To obtain the true velocity profile, the the Doppler profile must be deconvolved using the measured sample volume characteristic (Garbini, 1973; Jorgensen and Garbini, 1974).

The deconvolution procedure is not straightforward, and it was decided not to pursue it in this thesis. Instead, a simpler correction procedure was employed. At centrestream, underestimation of the peak velocity will

20 MHZ PDUVM: Spectral Mean

Re	Theoretical Vmax (cm/sec)	PDUVM Vmax (cm/sec)	Percent Deviation
462	47.8	42.7	10.7
686	72.3	67.1	7.2
848	89.3	81.9	8.3
1142	120.3	111.1	7.6

Table 2. Comparison of theoretical and 20 MHz PDUVM-measured maximum velocities (Vmax) at the four steady flow Reynolds numbers (Re). PDUVM velocities were calculated from the spectral mean.

occur when the PDUVM spectral mode or mean is used in the Doppler equation because neither of these frequencies estimates the highest velocity in the sample volume. A better estimate of the peak velocity is obtained with the maximum frequency. Possible spectral maximums include the frequency 8 dB above the mode or the frequency one standard deviation above the spectral mean. Use of a spectral maximum at all points in the velocity profile will shift the radial location of the points closer to centrestream due to the positive velocity gradient between the tube walls and centrestream. Furthermore, the two sample volumes adjacent to the centrestream sample volume contain the same spectral maximum as that in the centre, due to overlap (figure 19). By removing the two centre-adjacent points the Doppler velocity profile diameter is reduced, no velocity information is lost, and the shift in radial location of the spectral maximum points is incorporated into the velocity profile. This convolution correction procedure was carried out using the mode- and mean-related spectral maximums described above, and the resulting velocity profiles are presented in figure 20 for a Reynolds number of 686 along with the corresponding theoretical profiles. Both of the experimental profiles resemble the theoretical profile more closely than the mode- or mean-based PDUVM profiles. The spectral maximum profile based on the mean

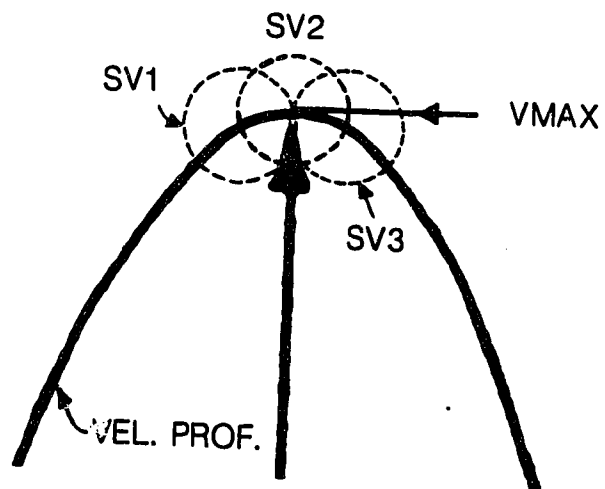


Figure 19. Illustration of the rationale for subtracting near centrestream velocity profile points. Sample volumes one (SV1) and three (SV3) contain the maximum velocity (VMAX) due to overlap with sample volume two (SV2). VEL. PROF. - velocity profile.

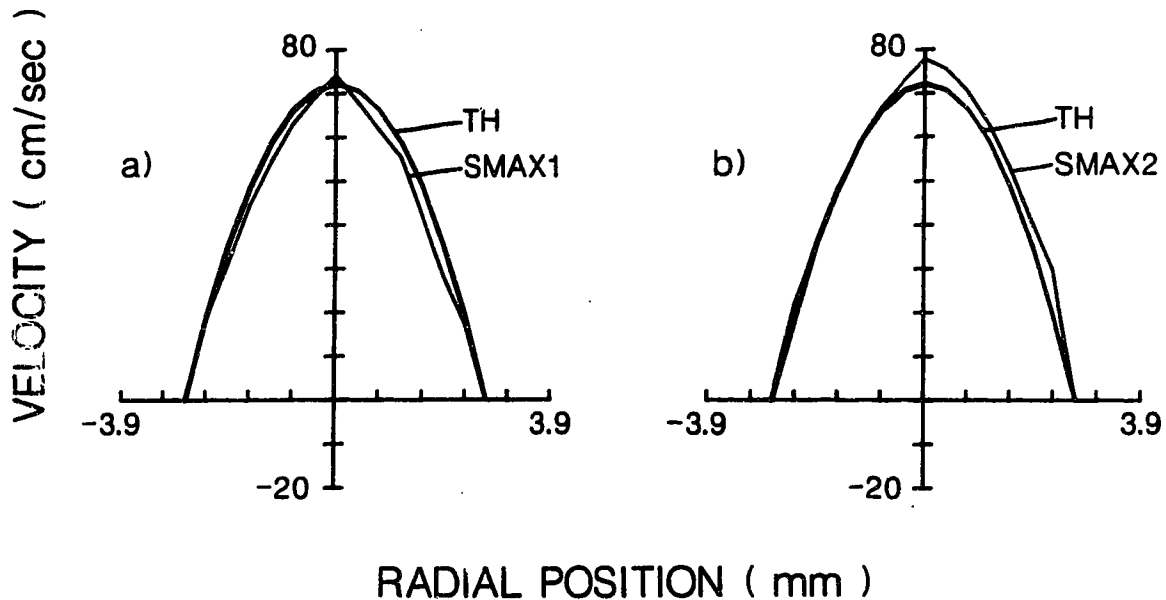


Figure 20. Comparison of 20 MHz PDUVM spectral maximum velocity profiles based on the mean plus one standard deviation (a) and the upper contour frequency (b) with the theoretical profile (TH) for steady laminar flow at a Reynolds number of 686. SMAX1 - spectral maximum profile based on the sum of the mean and one standard deviation. SMAX2 - spectral maximum profile based on upper contour (8 dB above mode).

plus one standard deviation has a peak velocity particularly close to the theoretical peak velocity. A quantitative comparison of the theoretical peak velocities and 20 MHz PDUVM mean plus one standard deviation spectral maximum peak velocities is given in table 3. The agreement is within 1.5 percent or less, a considerable improvement on the Doppler maximum velocities presented in table 2.

10 MHz PDUVM

The 10 MHz PDUVM was used to record velocity profiles under the same laminar flow conditions as were used with the 20 MHz PDUVM. Figure 21 depicts the 10 MHz velocity profiles obtained when the spectral mode was used as the representative frequency in the Doppler equation. Figure 22 presents 10 MHz velocity profiles calculated with the spectral mean as the representative Doppler frequency. In contrast to the results obtained with the 20 MHz PDUVM the 10 MHz spectral mean profiles were not appreciably smoother than the spectral mode profiles. In common with the 20 MHz profiles the 10 MHz mode and mean velocity profiles were generally parabolic in shape, overestimated the real tube diameters, and consistently underestimated the theoretical maximum velocity. Table 4 shows that the velocity underestimation using the 10 MHz spectral mean was substantially greater than that obtained with the 20 MHz PDUVM, ranging from 11.1 to 15.6 percent deviation.

20 MHZ PDUVM: Spectral Maximum

Re	Theoretical Vmax (cm/sec)	PDUVM Vmax (cm/sec)	Percent Deviation
462	47.8	47.1	1.5
686	72.3	73.0	1.0
848	89.3	89.2	0.1
1142	120.3	119.9	0.3

Table 3. Comparison of theoretical and 20 MHz PDUVM-measured maximum velocities (V_{max}) at the four steady flow Reynolds numbers (Re). The PDUVM velocities were calculated from the mean plus one standard deviation.

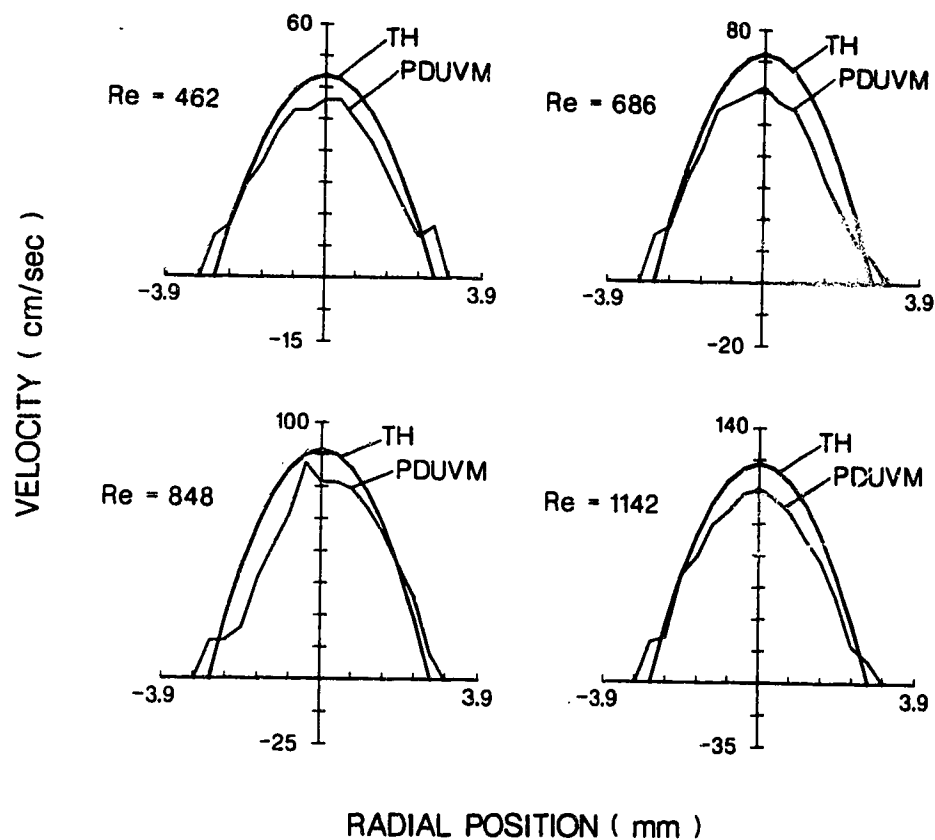


Figure 21. Steady flow velocity profiles recorded with the 10 MHz PDUVM and based on the spectral mode. For each Reynolds number (Re) the PDUVM profile is compared with the theoretical profile (TH) for the same flow and tube diameter.

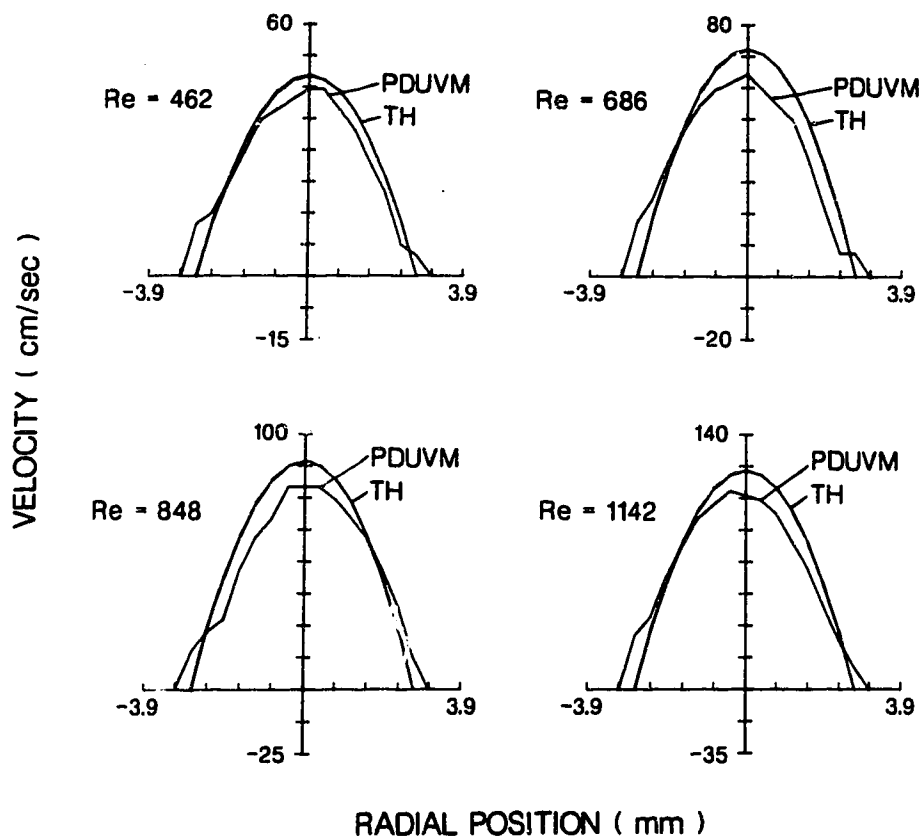


Figure 22. Steady flow velocity profiles recorded with the 10 MHz PDUVM and based on the spectral mean. For each Reynolds number (Re) the PDUVM profile is compared with the theoretical profile (TH) for the same flow and tube diameter.

Re	Theoretical Vmax (cm/sec)	PDUVM Vmax (cm/sec)	Percent Deviation
462	47.8	42.5	11.1
686	72.3	61.0	15.6
848	89.3	76.3	14.6
1142	120.3	105.1	12.6

Table 4. Comparison of theoretical and 10 MHz PDUVM-measured maximum velocities (Vmax) at the four steady flow Reynolds numbers (Re). PDUVM velocities were calculated from the spectral mean.

Analogous to the treatment of the 20 MHz data, the maximum Doppler velocities presented in table 4 were obtained from a second order regression of the 10 MHz PDUVM velocity profile points.

The convolution phenomenon was again apparent in the differences between the theoretical and 10 MHz PDUVM-measured velocity profiles. Likewise, the same convolution correction procedure used on the 20 MHz data was applied to the 10 MHz data. Results of the convolution correction procedure on the 10 MHz data using the same spectral maxima as were used with the 20 MHz data for a Reynolds number of 686 are shown in figure 23. As was observed in the analogous 20 MHz data, both profiles more closely followed the theoretical curve than the corresponding PDUVM profiles based on the spectral mode and mean. Table 5 shows the increased agreement between the 10 MHz spectral maximum (mean plus one standard deviation) peak velocity obtained by second order regression and the theoretical peak velocity at all four Reynolds numbers. The agreement was not as strong as that of the corresponding 20 MHz data (table 3).

Post-stenotic Flow with Steady Flow Upstream

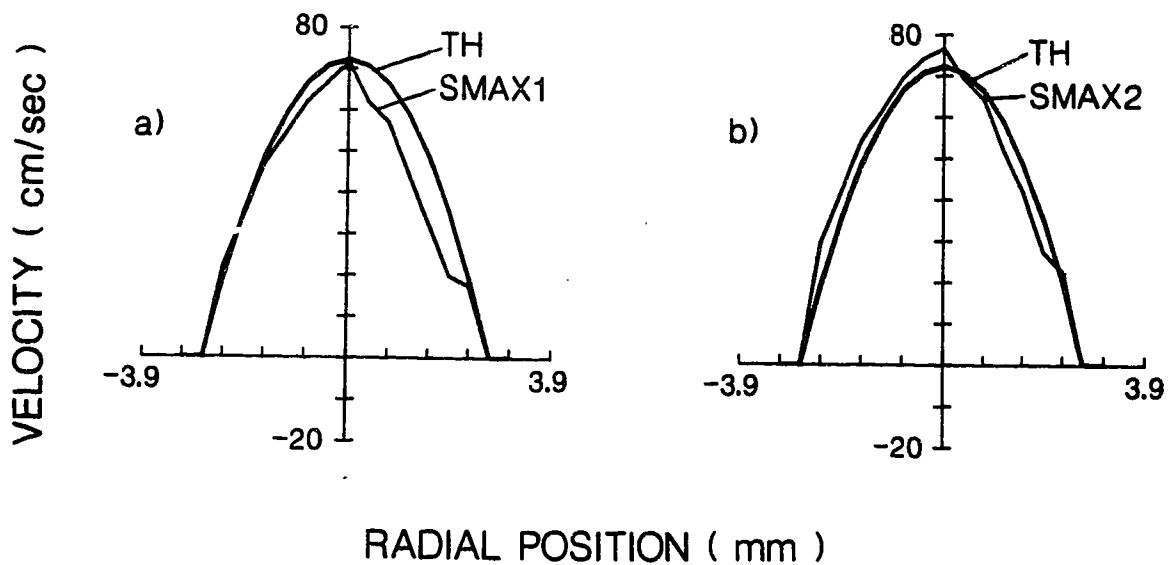


Figure 23. Comparison of 10 MHz PDUVM spectral maximum velocity profiles based on the mean plus one standard deviation (a) and the upper contour frequency (b) with the theoretical velocity profile (TH) for steady laminar flow at a Reynolds number of 686. SMAX1 - spectral maximum profile based on the sum of the mean and one standard deviation. SMAX2 - spectral maximum profile based on upper contour (8 dB above mode).

Re	Theoretical Vmax (cm/sec)	PDUVM Vmax (cm/sec)	Percent Deviation
462	47.8	47.6	0.4
686	72.3	68.2	5.7
848	89.3	84.6	5.3
1142	120.3	115.6	3.9

Table 5. Comparison of theoretical and 10 MHz PDUVM-measured maximum velocities (Vmax) at the four steady flow Reynolds numbers (Re). The PDUVM velocities were calculated from the mean plus one standard deviation.

Profiles Immediately Downstream: Comparison with Flow Visualization

Figure 24 is a close-up photograph of the test section immediately downstream of the 2.9 mm stenosis. It shows the direction of 20 MHz PDUVM sampling of the velocity field in the three experiments involving this stenosis as well as the six other post-stenotic experiments. Sampling sites across the tube diameter were separated by 0.5 mm as measured by the micromanipulator holding the PDUVM probe. Figure 25 illustrates a nine point velocity profile recorded 0.4 cm downstream of the 2.9 mm stenosis. The post-stenotic tube diameter was 5.5 mm and the flow rate was 4.56 ml/sec. For comparative purposes the theoretical velocity profile for unstenosed flow at the same Reynolds number (384) is superimposed on the post-stenotic velocity profile. The post-stenotic profile clearly contrasted with the laminar flow profile. The centrestream PDUVM velocities of the former were high in the forward direction while towards the tube walls velocities were much lower. Along one wall (-2.0 mm in figure 25) the velocity was low in the forward direction (labelled point v1 in figure 25). Along the opposite wall (+2.0 mm) the velocity was low in the reverse direction since point v9 lies below the zero velocity axis.

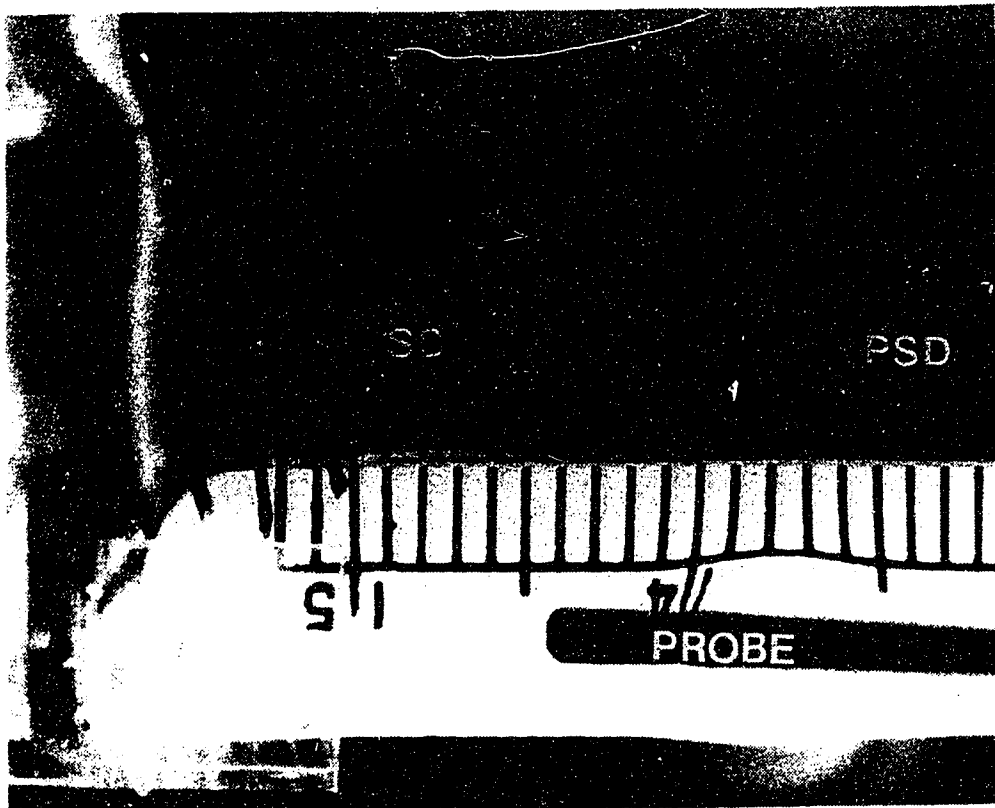


Figure 24. Test section close-up showing the 20 MHz PDUVM probe, a 2.9 mm stenosis diameter (SD), and 5.5 mm post-stenotic dialysis tubing diameter (PSD). The PDUVM probe was moved across the post-stenotic diameter in increments of 0.5 mm in the direction indicated by the arrow. The ruler divisions are in mm. Thus the distance between the points marked "14" and "15" is one cm.

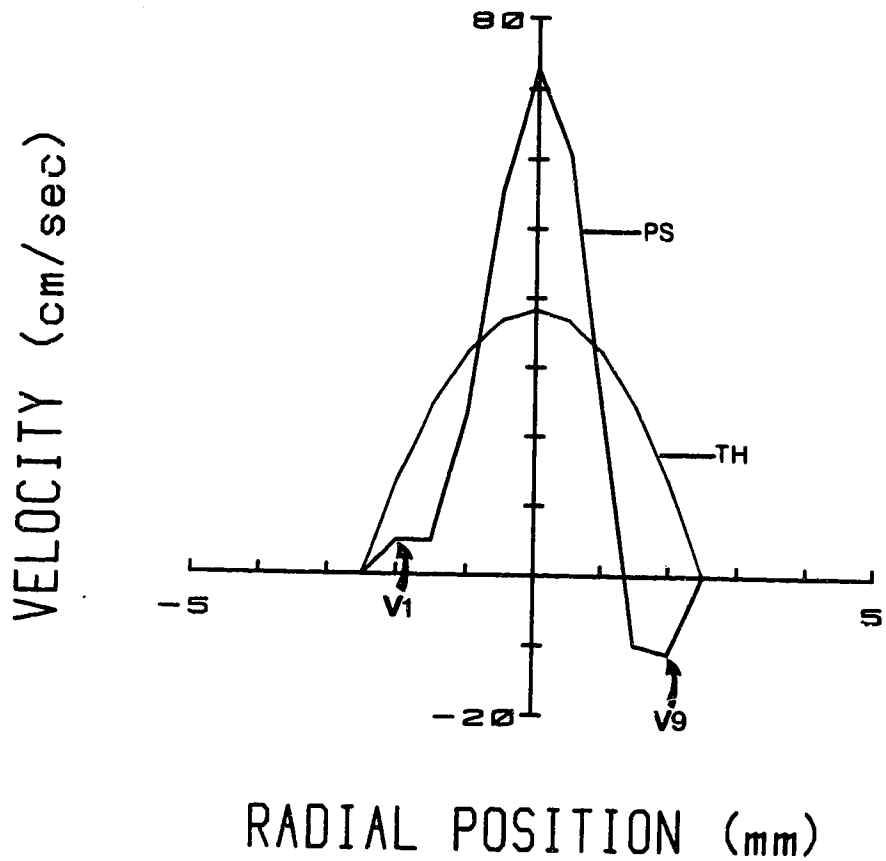


Figure 25. Nine point velocity profile recorded 0.4 cm downstream of the 2.9 mm stenosis (PS) at a Reynolds number of 384. Superimposed for comparison is the theoretical velocity profile (TH) for unstenosed flow at the same Reynolds number.

Figure 26 presents two successive frames of the cinecamera record of the same post-stenotic velocity field reported in figure 25. The light-reflecting particles emerging from the stenosis at centrestream were streaked, indicating high velocities. Thus a central post-stenotic jet was demonstrated by flow visualization. On either side of the jet the particles were spherical in shape, indicating low velocity, separated flow. The direction of both the fast and slow moving particles in the post-stenotic velocity field was determined by observing and recording their movements between cinefilm frames with a stop-frame projector. Figure 27 shows the type of analysis performed. It is a scaled diagram of figure 26 with position vectors drawn to salient particles across the tube diameter. The magnitude and direction of particle displacement was obtained by subtracting the position vectors corresponding to the first frame (figure 27(a)) from the vectors corresponding to the second frame (figure 27(b)).

The results of this analysis are illustrated in figure 28. Three different displacement vectors define three distinct post-stenotic flow regimes. There is a central region of particles with large forward displacements (the jet), and two peripheral regions (zones of flow separation) with small displacements; one in the forward direction and one in the reverse

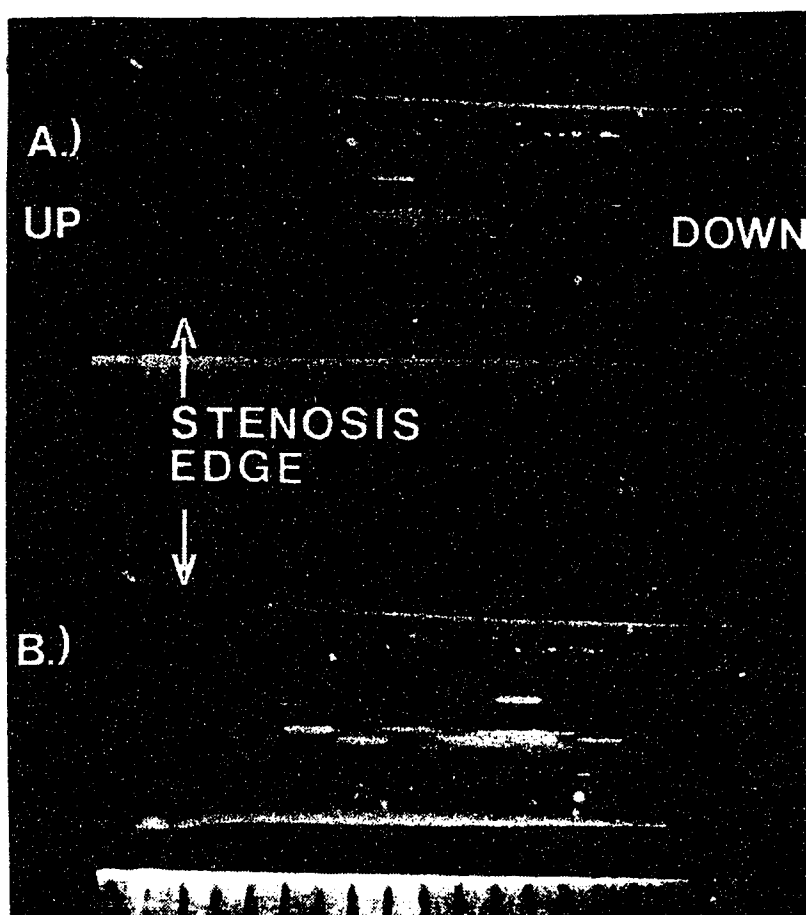


Figure 26. Two successive frames of the cinecamera record of the post-stenotic flow field of figure 25. Upstream and downstream ends of the illuminated test section are indicated by UP and DOWN, respectively. Also indicated is the downstream stenosis edge.

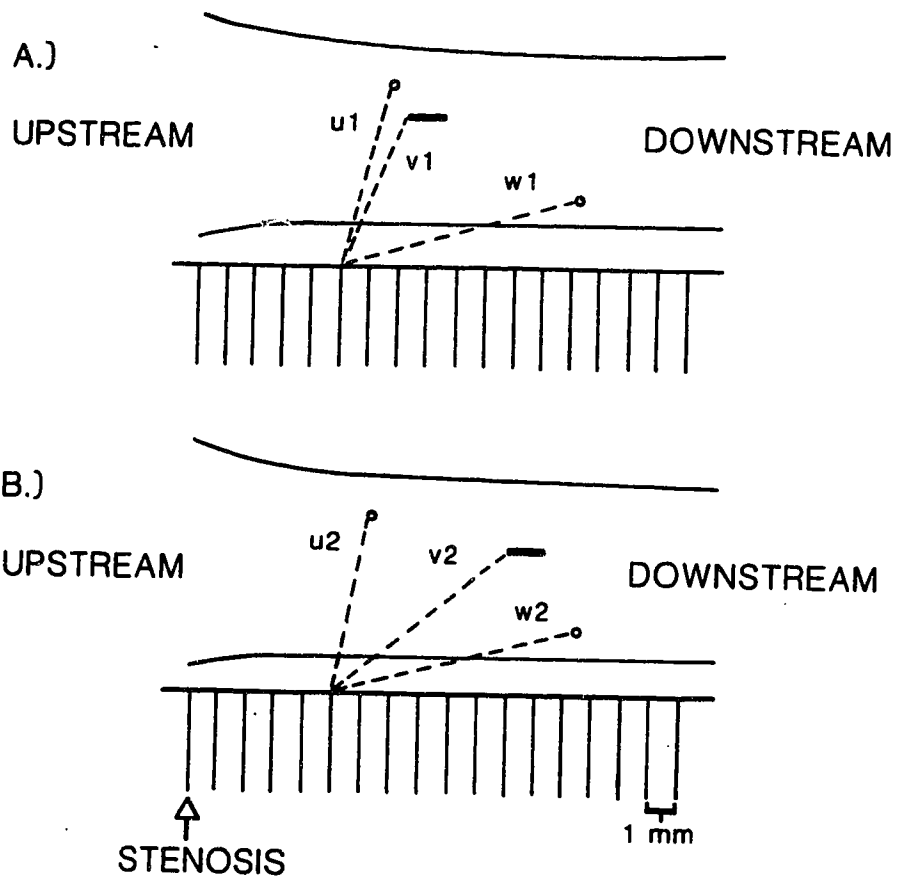


Figure 27. Scaled diagram of figure 26 with position vectors drawn to salient particles in the velocity field. Vectors u and w point to particles near to the tube walls on opposite sides of centrestream. Vector v points to a centrestream particle. Coefficient 2 denotes position vectors occurring 5 msec. after vectors labelled with coefficient 1.

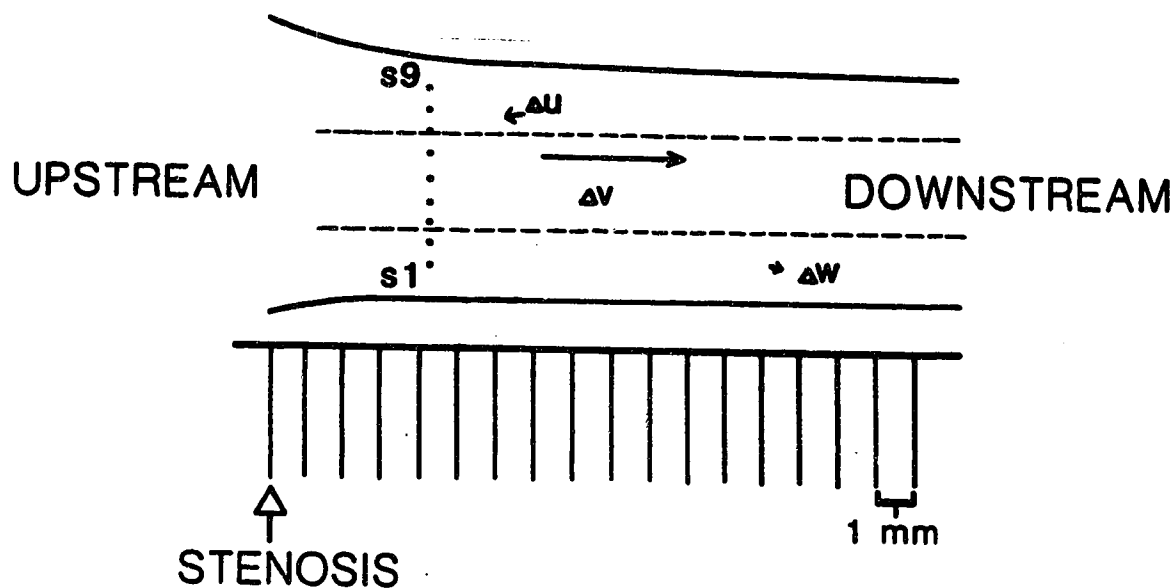


Figure 28. Three distinct post-stenotic flow regions identified by the flow visualization technique for the conditions of figure 25. The displacement vectors Δu , Δv , and Δw show the magnitude and direction of particle movements in each regime over the 5 msec. interval of figures 26 and 27. Also shown are the sample volume positions, S1 through S9, corresponding to the velocity profile of figure 25.

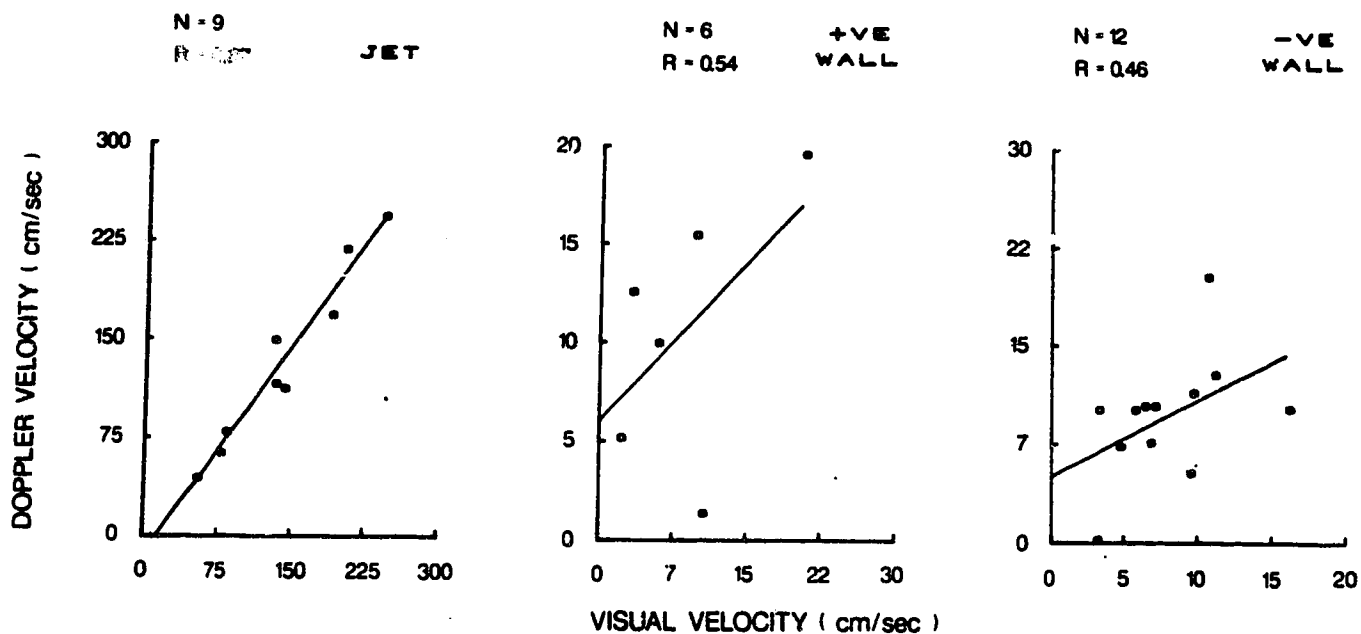
direction. Both zones of flow separation exhibited fluid recirculation which in two dimensional flow would result in reverse velocities along both walls. The observed low forward velocities along one wall probably were due to three-dimensional helical recirculation in which backward moving particles spiralled back on themselves in the forward direction. Thus a velocity profile with a low forward shoulder along one wall was still indicative of recirculation at that location. This asymmetric pattern of flow was typical of that observed in other experiments (five) where the Reynolds number was relatively low and the stenosis relatively wide. With higher flows and tighter stenoses both peripheral zones had slow, backward moving particles (three experiments). From the sample volume positions marked in figure 28 it can be seen that there is correspondance between the direction of flow regime motion determined by flow visualization and the direction recorded with the PDUVM (figure 25). In figure 25, for example, velocity v_9 at the ninth sample volume position is in the reverse direction. The visualized flow regime direction at the corresponding site (S9) in figure 28 is also reverse. This correspondance between visualized flow regime direction and PDUVM velocity direction was absolute in the nine post stenotic experiments. Since the time interval between cinefilm frames was known from the frame speed, it was possible to calculate the magnitudes

of the visualized particle velocities by dividing the displacement vector lengths by the frame to frame time interval.

The correlation between the PDUVM and visualized velocities was then determined for the three flow regimes as shown in figure 29. The peripheral flow separation regions are respectively denoted '-ve wall' for the region with reverse particle motion and '+ve wall' for the region with forward particle motion. There was a significant correlation between PDUVM and visualized velocity magnitudes for the jet flow regime ($r = 0.97$) but not the two regimes near the tube wall ($r = 0.54$, $r = 0.46$). As explained previously, there were six post-stenotic experiments with reverse motion along one wall and forward motion along the other wall, as well as three experiments with reverse motion along both walls. Thus 'n' for the '+ve wall' region was six and for the '-ve wall' region it was twelve.

Pattern of Axial Variation

Figure 30 shows a sequence of steady flow velocity profiles recorded at successively distal axial locations downstream of the 2.9 mm stenosis. The post-stenotic Reynolds number was 921. At each of the seven axial locations the profiles are plotted with respect to a horizontally drawn zero velocity axis, with positive (in the direction of upstream flow) velocities plotted above the zero axis. Thus at axial position one (0.6 cm



Correlation of post-stenotic flow regimes
 as determined by the 20 MHz PDUVM with the actual flow regimes
 identified by the flow visualization technique. Flow
 visualization velocities were calculated by dividing the
 frame to frame displacement vector magnitudes by their
 corresponding time intervals.

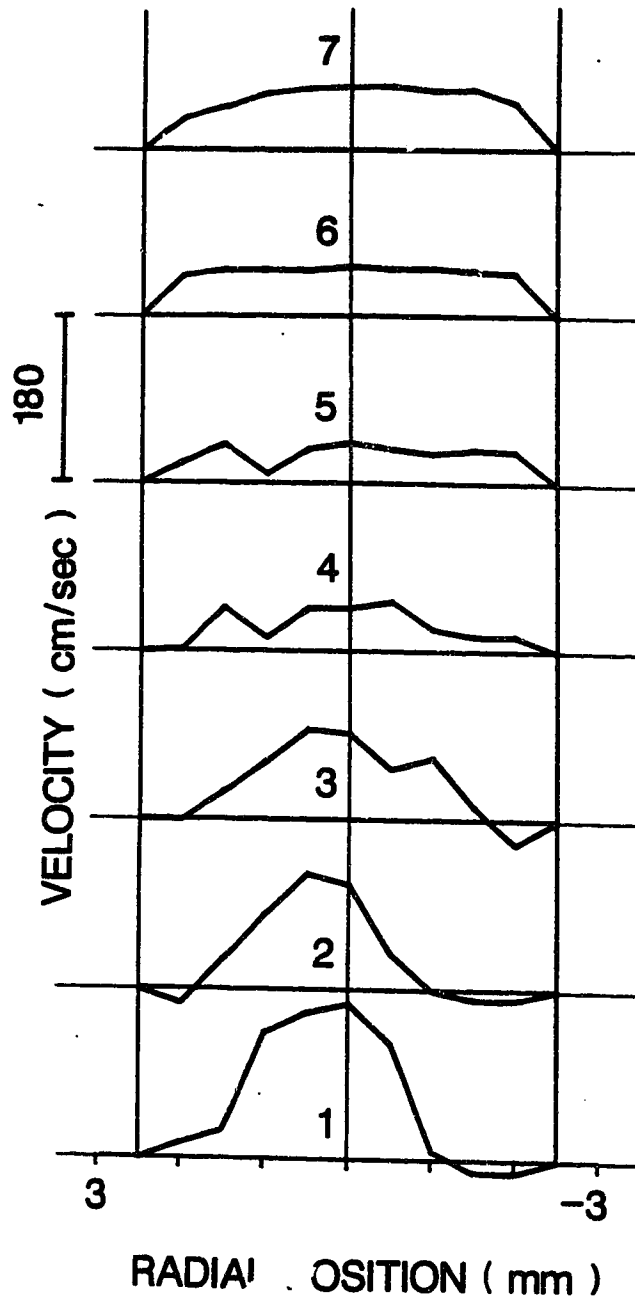


Figure 30. Plots of steady flow velocity profiles recorded with the 20 MHz PDUVM at seven axial locations downstream of the 2.9 mm model stenosis. The post-stenotic Reynolds number was 921 and each profile is plotted with respect to a horizontal zero velocity axis. Positive (in the direction of upstream flow) velocities lie above the zero velocity axis and negative velocities below. Axial positions are, in cm downstream of the stenosis: 1: 0.6; 2: 1.8; 3: 2.8; 4: 3.8; 5: 4.6; 6: 7.5; 7: 14.0.

downstream) there is a region of low magnitude, reverse direction velocity towards the right (-2.5 mm) wall. At the same axial location there is a shoulder of low forward velocities along the opposite wall (+2.5 mm), and the centrestream velocities are high in the forward direction. Thus a post-stenotic jet with peripheral flow separation zones is observed immediately downstream of the stenosis as was illustrated in figure 25. Similar velocity profiles may be seen at axial positions two and three (1.8 and 2.8 cm downstream, respectively) although there is a trend toward reduction in jet velocity and the separation zone velocities show some variation. At axial position four (3.8 cm downstream) the velocity varies erratically across the tube diameter, suggesting disturbed flow and jet breakup. This was confirmed by examination of the corresponding flow visualization record (not shown) which revealed a random distribution of spherical particles instead of the orderly axial streaking associated with laminar flow. The velocity profiles at axial positions five and six (4.6 and 7.5 cm downstream) are less erratic than that at axial position four, suggesting a dampening of the flow disturbance. Far (14 cm) downstream of the stenosis at axial position seven the velocity profile is nearly parabolic, suggesting recovery to laminar flow.

The axial velocity profile patterns of different steady flow post-stenotic experiments compared with the

experiment of figure 30 as follows. Downstream of the same stenosis at lower flow rates the jet velocities were lower, jet breakup occurred at the same axial location (3.8 cm downstream), and jet breakup was less intense (the velocity profiles were less erratic). Also, recovery to laminar flow occurred somewhat more proximally; 11.8 cm downstream at a post-stenotic Reynolds number of 635, and 12.0 cm downstream at a Reynolds number of 371. Downstream of the tighter (1.9 mm) stenosis at a similar flow rate to that of figure 30 the jet velocities were higher, jet breakup occurred more proximally (2.6 cm downstream), and the breakup was more intense (the velocity profile was more erratic). Downstream of the wider (4.0 mm) stenosis at a similar flow rate to that of figure 30 the jet velocities were lower, jet breakup occurred more distally (4.6 cm downstream), and the breakup was less intense (the velocity profile was less erratic). It was not possible to compare the sites of recovery to laminar flow of the different stenosis grades since velocity profiles were not always recorded far enough downstream of the stenoses.

The axial pattern of post-stenotic jet, jet breakup, and recovery to laminar flow demonstrated by the velocity profiles presented here is also demonstrated by the variation in post stenotic midline spectral width in a later section of this thesis (see

'Factors Affecting PDUVM Spectral Width').

Post-stenotic Flow with Pulsatile Flow Upstream

20 MHz PDUVM velocity profiles were recorded downstream of the model stenoses over a wide range of pulsatile flow conditions (see methods). The pattern of axial variation, illustrated in figure 31, was similar throughout. The data in figure 31 were obtained from an experiment where the pulse frequency was 3 Hz, the pulsatility index was 0.93, the mean post stenotic Reynolds number was 324, and the stenosis was 2.9 mm in diameter. At all illustrated times in the pulse cycle the velocities are highest at the first two axial positions (0.6 and 1.6 cm downstream) and are concentrated at centrestream, suggesting jet flow. Centrestream velocities, however, vary throughout the cycle and are at a minimum in panel A, increase in panel B, reach peaks in panels C and D, and progressively decline in panels E and F. On either side of the peak at these two axial positions there are low velocity shoulders indicating flow recirculation. This interpretation is supported by the flow visualization data in figures 51 and 52. The flow visualization patterns at these two axial locations show a central jet and peripheral zones of flow separation throughout the cycle. A variation in velocity with time in the pulse cycle similar to that indicated by the velocity profiles is demonstrated by variation in visualized streak lengths.

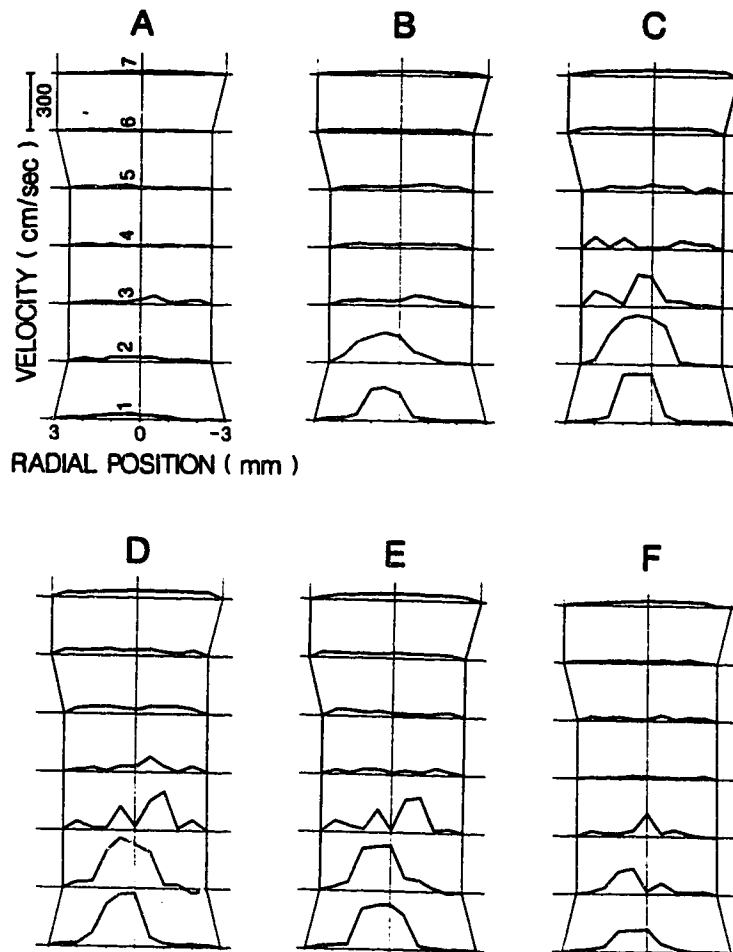


Figure 31. Plots of pulsatile flow velocity profiles at seven axial locations downstream of the 2.9 mm model stenosis recorded with the 20 MHz PDUVM at six different times in the pulse cycle. The pulse frequency was 3 Hz, the pulsatility index was 0.93, and the mean post-stenotic Reynolds number was 324. Axial positions are, in cm downstream of the stenosis, 1: 0.6, 2: 1.6, 3: 2.6, 4: 3.6, 5: 4.1, 6: 5.1, 7: 14.8. Times are, in msec after the sync pulse, A: 0, B: 50, C: 100, D: 150, E: 200, F: 250.

The velocity profiles at axial positions three and four (2.6 and 3.6 cm downstream) show sharp velocity fluctuations across the tube diameter, suggesting disturbed flow due to jet breakup throughout most of the pulse cycle. The corresponding flow visualization patterns (figures 53 and 54) exhibit random distributions of tracer particles across the post-stenotic tube. At one time in the pulse cycle, panel B in figure 31, flow does not appear to be disturbed at these axial locations (three and four) since the velocity profiles are smooth. This is the acceleration phase of the cycle, and the acceleration tends to stabilize the velocity field.

Far (14.8 cm) downstream of the stenosis at axial position seven, the velocity profiles in all panels of figure 31 are smooth across the tube diameter, suggesting laminar flow. The presence of laminar flow is supported by the flow visualization data of figure 55, where the particle patterns are orderly and show axial streaking. Thus, although the centrestream velocities fluctuated in time, the general post-stenotic flow patterns or regimes indicated by the velocity profiles in pulsatile flow were similar to those seen in steady flow. These flow regimes were, in summary, a jet with lateral zones of flow separation observed immediately downstream, followed by disturbed flow distal to the jet and by eventual recovery to laminar flow far downstream.

There is an apparent variation in the tube diameter indicated in figure 31. This occurs in part due to stretching of the soft dialysis tubing over the slightly wider outer wall of the stenosis. Thus the tube diameter is greater immediately (0.6 cm) downstream of where it is stretched over the acrylic stenosis than further downstream. At intermediate locations the increased flow velocity due to the jet results in a reduction in lateral pressure, thus decreasing the diameter to which the dialysis tubing is distended. Far downstream of the stenosis (axial position 7, 14.8 cm down) flow velocity has decreased due to jet dissipation. Consequently the lateral pressure is increased along with the diameter to which the dialysis tubing is distended.

There is also apparent asymmetry in the post-stenotic velocity profiles of figure 31. The asymmetry is most prominent in the post-stenotic jet, the profile tending to peak to the left of centreline. Although the stenosis itself was symmetric, it was very difficult to maintain the connection between the rigid stenosis and soft dialysis tubing perfectly symmetric. Indeed, effort was made only to make the connection roughly symmetric. It is thus probable that the observed velocity profile asymmetry was due to small deviations in the post-stenotic geometry influencing the velocity field.

Cross-sectional Profiles: Velocity Contours

The concept of a velocity contour was introduced in the chapter on materials and methods (see figures 11 to 13 there). It is briefly reviewed here to provide continuity between this section and the following one which presents velocity contour results from the dog aorta. Briefly, a velocity contour is a record of the velocity information from across the entire cross section of the vessel under study. This involves recording a grid of velocity points instead of recording a set of points along a single diameter as is done for a velocity profile. Figure 32 presents velocity contours obtained three cm downstream of a 42 percent diameter reducing stenosis in a dog common carotid artery at four different times in the pulse cycle. The centrestream contour velocities increase with pulse acceleration and decrease with deceleration. A consistent zone of reverse velocities in the right ventral quadrant of the artery is present throughout the pulse cycle. It is important to note that the contours do not necessarily represent the exact velocities measured with the PDUVM but are rather calculated from an interpolation of the points of the actual velocity grid recorded.

C. VELOCITY CONTOURS AT AORTIC BRANCHES

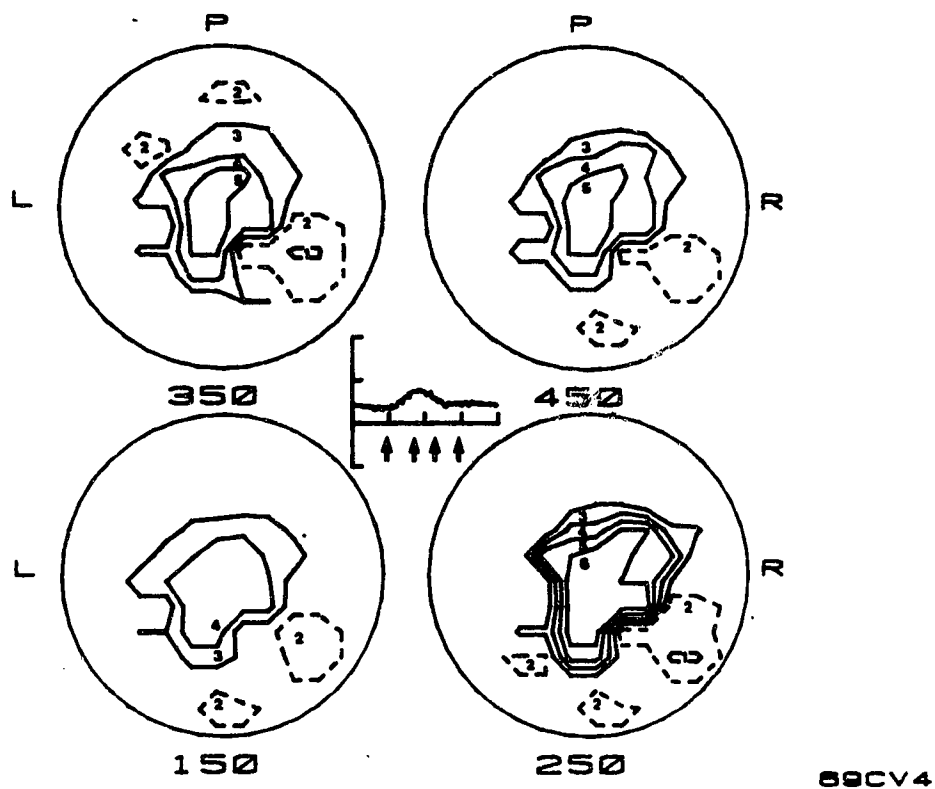


Figure 32. Cross-sectional velocity contours at 150, 250, 350, and 450 msec after the EKG R wave (indicated by the arrow below the velocity waveform at centre) three cm downstream of a 42 percent diameter reducing stenosis on a dog common carotid artery. Contour velocities are (1) -22.7, (2) -1.0, (3) 20.7, (4) 42.5, (5) 64.2, (6) 85.9 cm/sec. L: Left, R: Right, P: Posterior (dorsal).

Anaesthetized Dog Studies

Post Cranial Mesenteric Aortic Velocity Field

Cross-sectional velocity contours at 0.5 cm downstream of the cranial mesenteric artery of dog number 80 are presented in figures 33 and 34. Velocities were sampled at the peak of the pulse cycle (systole, figure 33) and at the post-systolic minimum (figure 34). In the aorta above the celiac artery mean flow was 266 ml/min and mean Reynolds number 136; peak values were 968 ml/min and 723 respectively. Flow divided 32 percent to the celiac and 26 percent to the mesenteric artery. The mesenteric artery had a cross-sectional area 15 percent of the aortic area. Aortic diameter at the measurement site was 0.93 cm. There is asymmetry in both sets of contours along a diameter from the right ventral to the left dorsal aspect of the artery. At peak systole there is a high velocity gradient at the right ventral aspect and a low velocity gradient at the left dorsal aspect. There are, however, no reverse velocities along this diameter. At the post-systolic minimum there is a zone of reverse velocities centered at the left dorsal aspect and a zone of forward velocities at the right ventral aspect of the aorta. In the six other aortae studied at this branch similar asymmetry was present at the post-systolic minimum of the cycle with all but one showing defined zones of both forward and reverse velocities. As in the typical experiment shown in

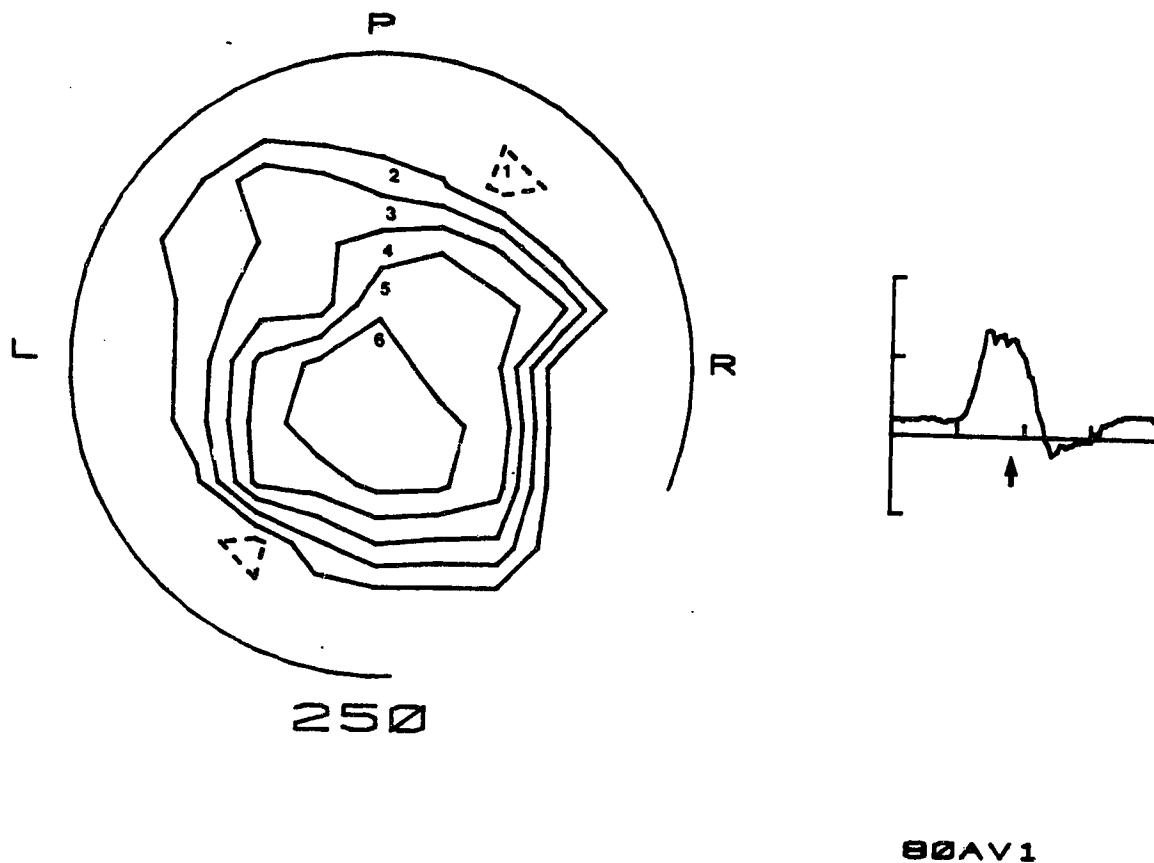
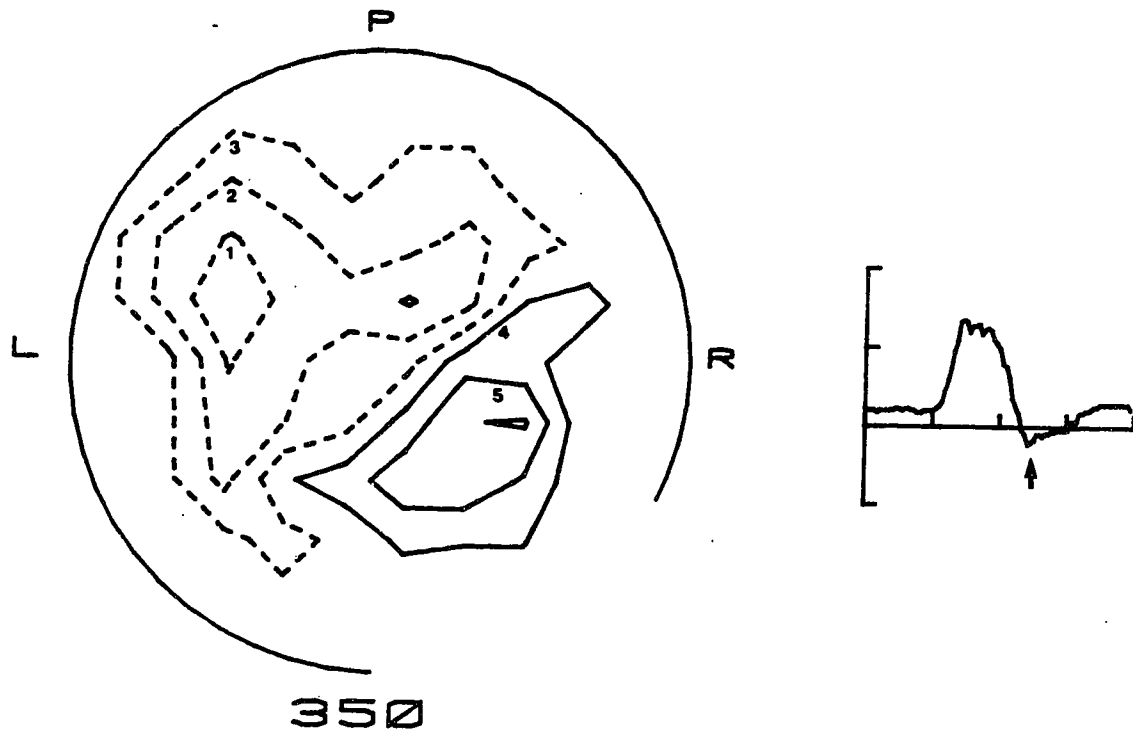


Figure 33. Cross-sectional aortic velocity contours at 250 msec after the EKG R wave (indicated by the arrow below the centrestream velocity waveform to the right) 0.5 cm downstream of the cranial mesenteric artery origin. Contour velocities are (1) -1.0, (2) 4.3, (3) 9.5, (4) 14.8, (5) 20.0, (6) 25.3 cm/sec. L: left, R: right, P: posterior (dorsal). The circular frame is broken to indicate the circumferential location and size of the origin of the upstream branch.



80AV2

Figure 34. Cross-sectional aortic velocity contours at 350 msec after the EKG R wave (indicated by the arrow below the centrestream velocity waveform to the right) 0.5 cm downstream of the cranial mesenteric artery origin. Contour velocities are (1) -8.5, (2) -4.8, (3) -1.0, (4) 2.8, (5) 6.7, (6) 10.5 cm/sec. L: left, R: right, P: posterior (dorsal). The circular frame is broken to indicate the circumferential location and size of the origin of the upstream branch.

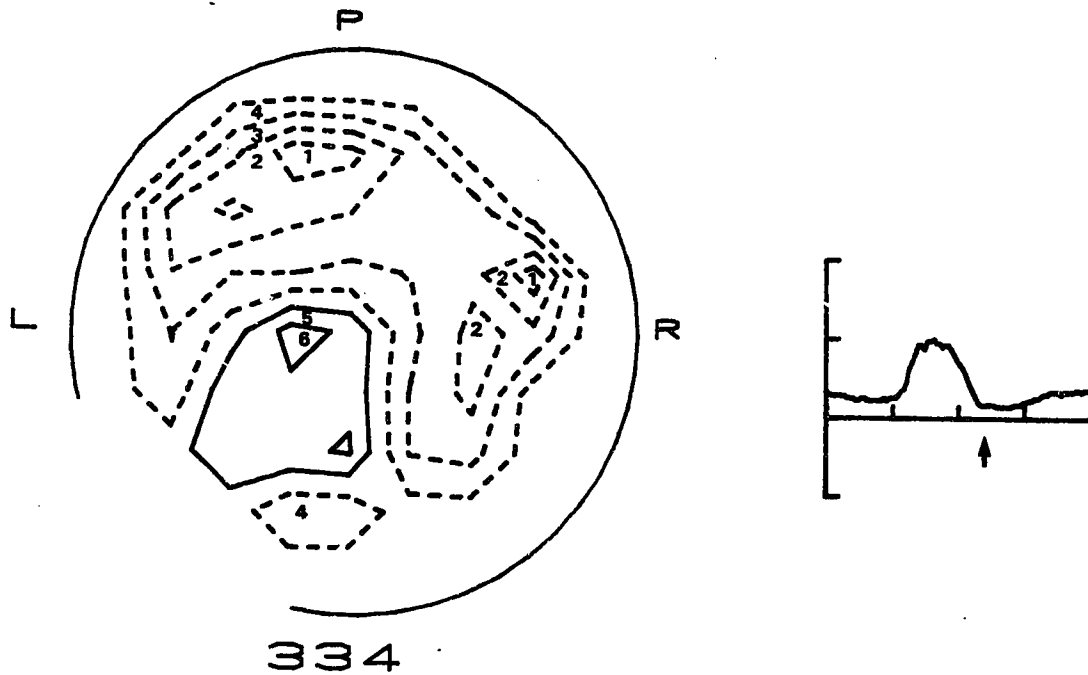
figures 33 and 34, the reverse velocities were centered opposite and the forward velocities were adjacent to the origin of the branch. Asymmetry at the peak of the cycle was present in only four of the other experiments and in none of them was there a defined zone of reverse velocities at this phase of the cycle. This indicates a zone of transient recirculation rather than a zone of recirculation which persists throughout most of the pulse cycle as found in the post-stenotic velocity field. In one experiment in which relative mesenteric flow was increased from 26 to 30 percent by shunting the mesenteric artery to the femoral vein there was an increase in the extent and amplitude of the reverse velocities but there was no marked change in the portion of the cycle occupied by them. Occlusion of the cranial mesenteric artery in one experiment resulted in loss of asymmetry at both peak systole and the post-systolic minimum.

Post Left Renal Aortic Velocity Field

Similar asymmetry of the aortic velocity field to that found downstream of the cranial mesenteric artery was also found 0.5 cm downstream of the left renal artery in five out of six experiments. In the five experiments there was asymmetry at both the peak systolic and post-systolic phases of the cycle. But, as was the case downstream of the mesenteric artery, reverse velocities were present only during the

post-systolic phase. The recirculation is transient and is not present during the systolic part of the cycle. The pattern here is therefore similar to that in the post cranial mesenteric velocity field and again contrasts with that found in the post-stenotic velocity field. The expectation that the asymmetry was localized to the region of the branch was confirmed in one experiment. In this experiment the velocity field was explored 3 cm downstream in addition to 0.5 cm downstream of the left renal artery. A symmetrical velocity field was found at the former location. As referred to above, in one of the six experiments there was no asymmetry. The lack of asymmetry in this experiment may be due to the fact that in this dog there was no axial separation between the origins of the right and left renal arteries. In this set of experiments relative flow in the left renal artery varied between individual experiments from 9 to 64 percent and peak aortic Reynolds number varied from 154 to 657.

Aortic velocity contours from 0.5 cm downstream of the left renal artery typical of the five experiments showing asymmetry are shown in figure 35. In this experiment mean aortic blood flow upstream of the renal arteries was 551 ml/min and Reynolds number was 287. Flow divided 27 percent to the right and 28 percent to the left renal artery. The cross sectional area of the right renal artery was 21 percent of the aorta while the



74AV1

Figure 35. Cross-sectional aortic velocity contours at 334 msec after the EKG R wave (indicated by the arrow below the centrestream velocity waveform to the right) 0.5 cm downstream of the left renal artery origin. Contour velocities are (1) -6.8, (2) -4.8, (3) -2.9, (4) -1.0, (5) 0.9, (6) 2.8 cm/sec. L: left, R: right, P: posterior (dorsal). The circular frame is broken to indicate the circumferential location and size of the origin of the upstream branch.

left was 24 percent. The aortic diameter at the measurement site was 0.91 cm. The forward velocities are grouped in the left ventral region of the cross section with the reverse velocities extending over the rest of the cross-section. The situation is therefore similar to that found downstream of the mesenteric artery in that peak forward shear is adjacent to the origin of the branch while the low and reverse shears are situated towards the aortic wall opposite the branch origin. As in the mesenteric study reverse velocities were only found in the post-systolic phase of the cycle so that recirculation was transient. In the animals studied, the origin of the renal arteries from the aorta was ventral with the left origin usually more ventrally situated than the right one. In this particular preparation because the axial separation of the origins of the two renal arteries was wide (1.8 cm) the aortic velocity fields were also recorded midway between the two origins and 0.5 cm below the right renal artery. Midway between the two renal arteries, where the aortic diameter was 0.95 cm., in the post-systolic phase of the cycle there is a centrally placed zone of forward velocity with reverse velocities surrounding it, figure 36. At the post-systolic minimum 0.5 cm downstream of the right renal artery, where the aortic diameter was 0.96 cm., there is a zone of forward velocity on the right ventral aspect of the aortic cross-section adjacent to the

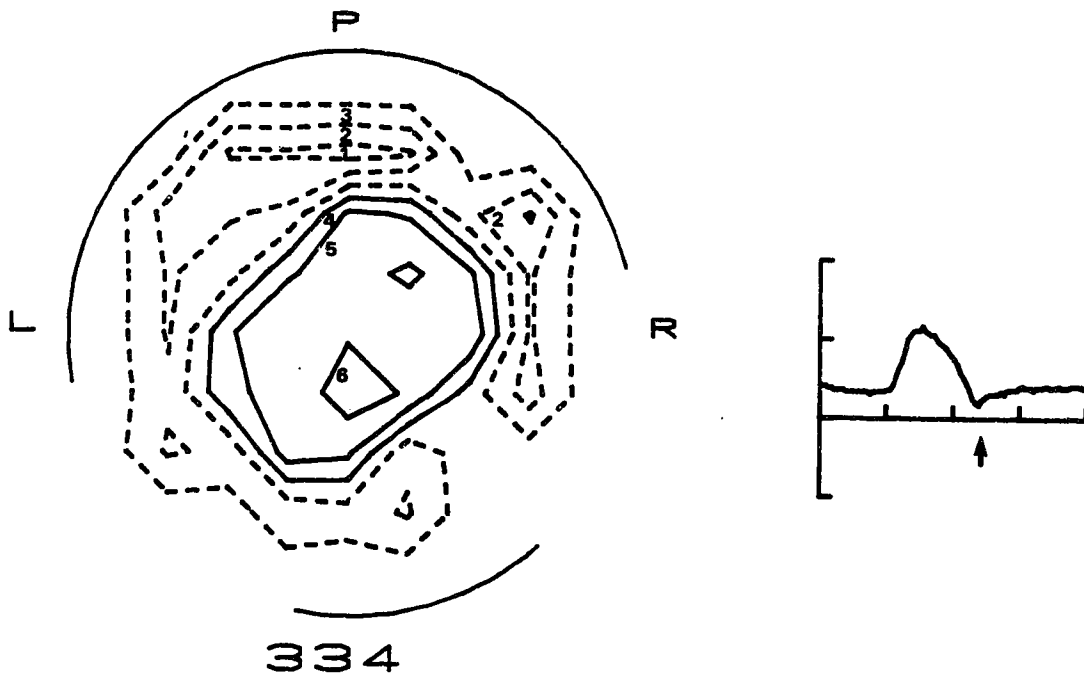


Figure 36. Cross-sectional aortic velocity contours at 334 msec after the EKG R wave (indicated by the arrow below the centrestream velocity waveform to the right) midway between the two renal artery origins (axial separation 1.8 cm). Contour velocities are (1) -4.6, (2) -2.8, (3) -1.0, (4) 0.8, (5) 2.6, (6) 4.5 cm/sec. L: left, R: right, P: posterior (dorsal). The circular frame is broken to indicate the circumferential location and size of the origins of the upstream (right) and downstream (left) branches.

origin of the right renal artery, figure 37. A zone of reverse velocity occupies the remaining three quarters of the cross section with the greatest reverse velocities concentrated in the left dorsal aspect opposite the origin of the right renal artery.

A consistent flow pattern of a region of high forward velocities adjacent to and a transient zone of reverse velocities in the post systolic phase opposite the origin of the branch is thus seen 0.5 cm below the cranial mesenteric, left renal, and right renal artery in the aortic cross section.

In Vitro Model Studies

Steady Flow

Figure 38 presents *in vitro* aortic velocity contours recorded 0.5 cm downstream of the right renal artery origin under conditions of steady upstream flow with varying right renal flow. With zero right renal flow (figure 38(A)) there is symmetry in the contours along the aortic diameter in the plane of the renal branch, i.e. along the aortic diameter from the right ventral to the left dorsal aspect of the model aorta. Thus a velocity profile along this diameter would be relatively symmetric, with steep velocity gradients at both the right ventral and left dorsal aspects, as is indicated by the closeness of adjacent contour lines. Furthermore, all the flow velocities are in the forward

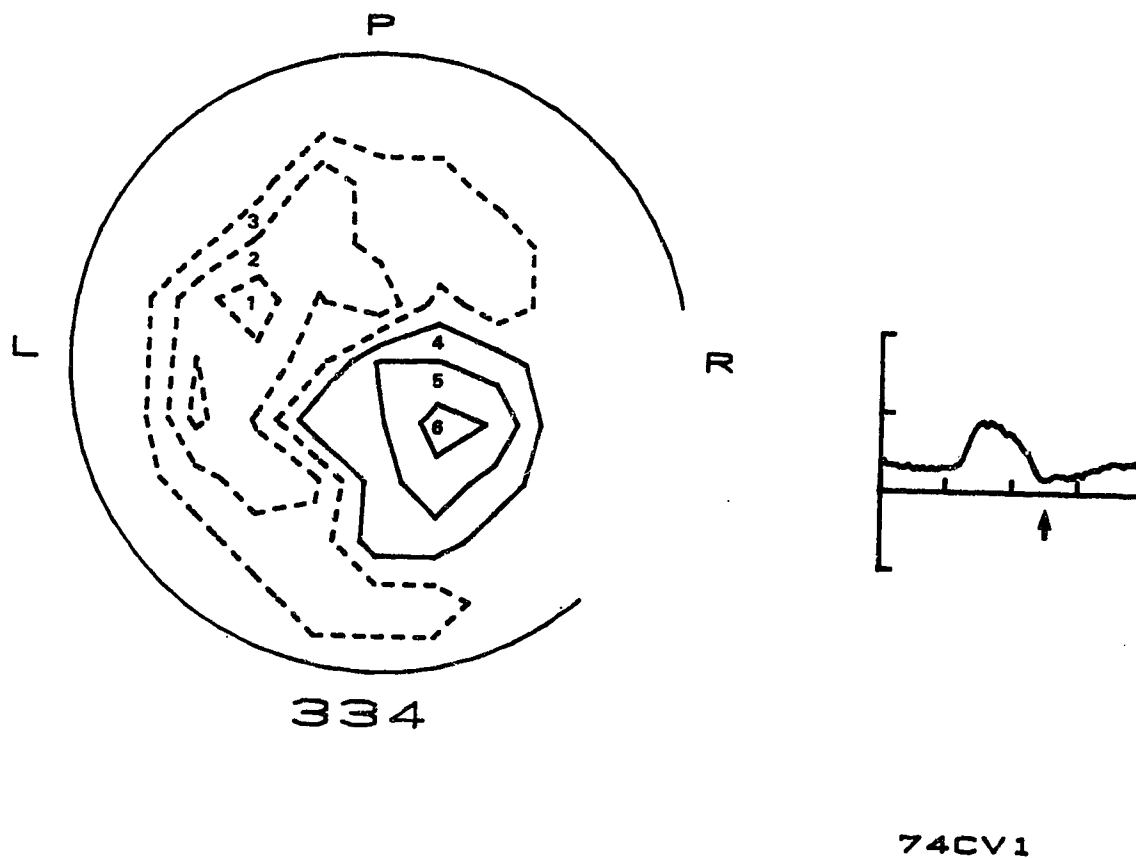


Figure 37. Cross-sectional aortic velocity contours at 334 msec after the EKG R wave (indicated by the arrow below the centrestream velocity waveform to the right) 0.5 cm downstream of the right renal artery origin. Contour velocities are (1) -5.4, (2) -3.2, (3) -1.0, (4) 1.2, (5) 3.4, (6) 5.7 cm/sec. L: left, R: right, P: posterior (dorsal). The circular frame is broken to indicate the circumferential location and size of the origin of the upstream branch.

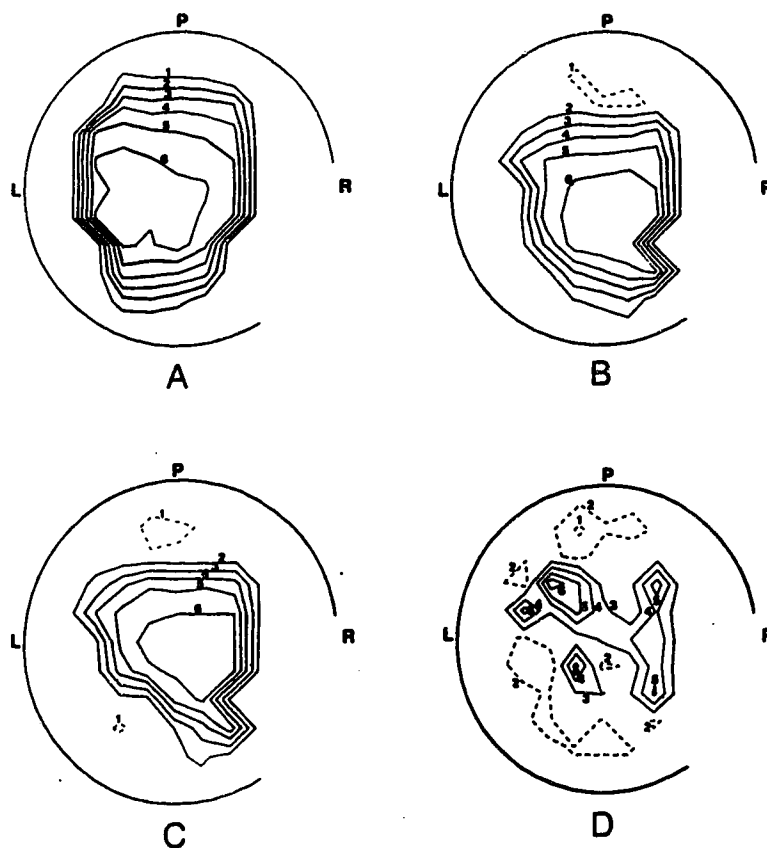


Figure 38. Cross-sectional model aortic velocity contours 0.5 cm downstream of the right renal artery origin under conditions of steady upstream flow (1197 ml/min) with right renal flows of zero(A), 28(B), 40(C), and 56(D) percent of upstream aortic flow. L: left, R: right, P: posterior(dorsal). The circular frame surrounding each set of contours is broken to indicate the circumferential location and size of the origin of the right renal artery. Contour velocities are, in cm/sec: A: 1:6.1, 2:11.6, 3:17.0, 4:22.5, 5:27.9, 6:33.4, B: 1:-1.7, 2:2.5, 3:6.7, 4:11.0, 5:15.2, 6:19.5, C: 1:-3.0, 2:2.5, 3:7.9, 4:13.4, 5:18.8, 6:24.3, D: 1:-10.0, 2:-0.9, 3:8.2, 4:17.3, 5:26.4, 6:35.5.

(positive) direction. With right renal flow at 28 percent of aortic flow (figure 38(B)) there is asymmetry in the contours along the aortic diameter in the plane of the renal branch. Now the contours adjacent to the branch are close while those opposite the branch (in the left dorsal aspect) are further apart. Thus a velocity profile along this diameter would be skewed toward the branch. In addition, at the most peripheral dorsal aspect there is a zone of reverse velocities (-1.7 cm/sec). A similar contour pattern is apparent in figure 38(C), where the right renal flow is now 40 percent of aortic flow. In this situation there is a toward-the-branch skewing of the velocity profile in the plane of the branch and a reverse velocity zone (-3.0 cm/sec) dorsally. In addition, there is a small zone of reverse velocities of the same magnitude along the left ventral aspect of the aorta. The peak reverse and forward velocities are higher with 40 percent right renal flow than with 28 percent flow.

A highly asymmetric contour pattern is shown in figure 38(D), where the right renal flow is 56 percent of aortic flow. The peak forward velocity of 35.5 cm/sec is well off centre in the left dorsal quadrant of the aorta. This finding is in contrast to the velocity pattern in the vicinity of centrestream in the three other steady flow experiments where the flow is always maximal and forward in direction. The peak reverse

velocity (-10.0 cm/sec) is located in the dorsal aspect of the aorta, as is the case in the experiments with lower right renal flows. A larger region of lower reverse velocity (-0.9 cm/sec) surrounds the peak reversal site. Finally, there is an extensive region of -0.9 cm/sec reverse velocity in the peripheral left ventral aspect of the aorta. Thus in figure 38(D), as in figure 38(C), there are two large zones of reverse velocity, one on either side of the aortic diameter in the plane of the renal branch. Furthermore, these reverse velocity zones are situated along the perimeter of the aorta roughly opposite to the ostium of the right renal artery.

The contours of figure 38(D) are suggestive of highly disturbed flow. This was indeed the case, as can be seen in the grid of velocity waveforms recorded under the high right renal flow conditions (figure 39). Unlike the flat waveforms typical of steady flow, most of the waveforms in figure 39 exhibit high frequency oscillations characteristic of disturbed flow. A reasonable question which arises in this situation is: given the unstable nature of the flow field depicted in figure 39, how representative is figure 38(D) of the predominant contour pattern over time? The answer to this question is provided in figure 40, which presents velocity contours derived from four different times in the waveform grid of figure 39. None of the contour

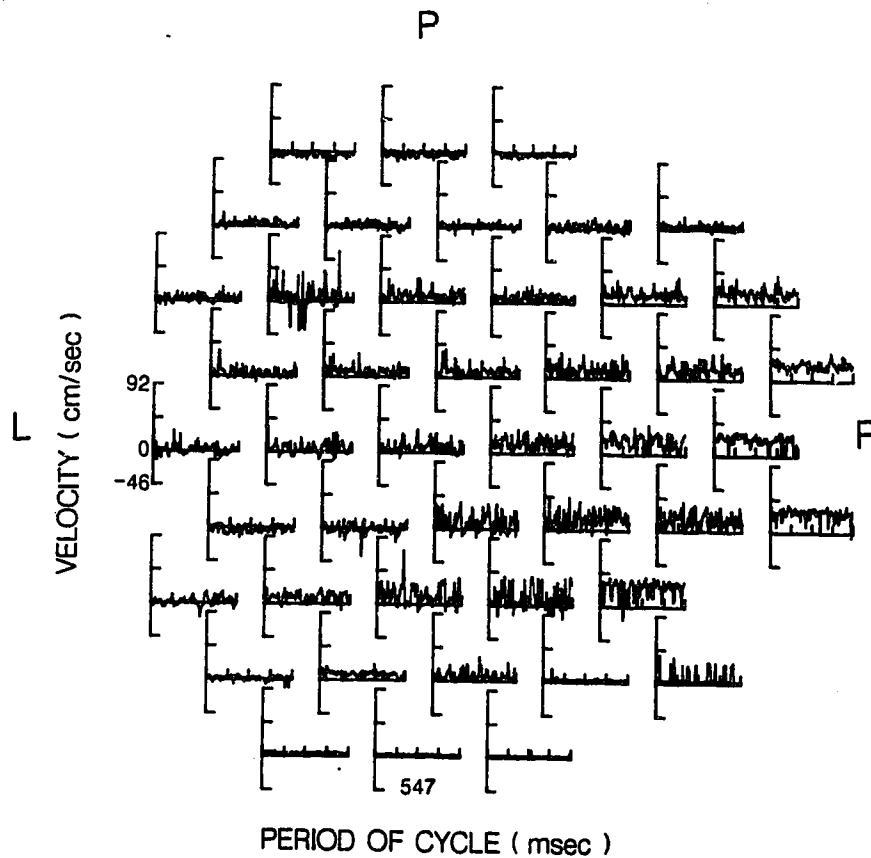


Figure 39. The grid of velocity waveforms from which the contours of figure 38(D) (maximum right renal branch flow) were derived and illustrating the unsteady, disturbed nature of the post-right renal flow. L: left, R: right, P: posterior(dorsal).

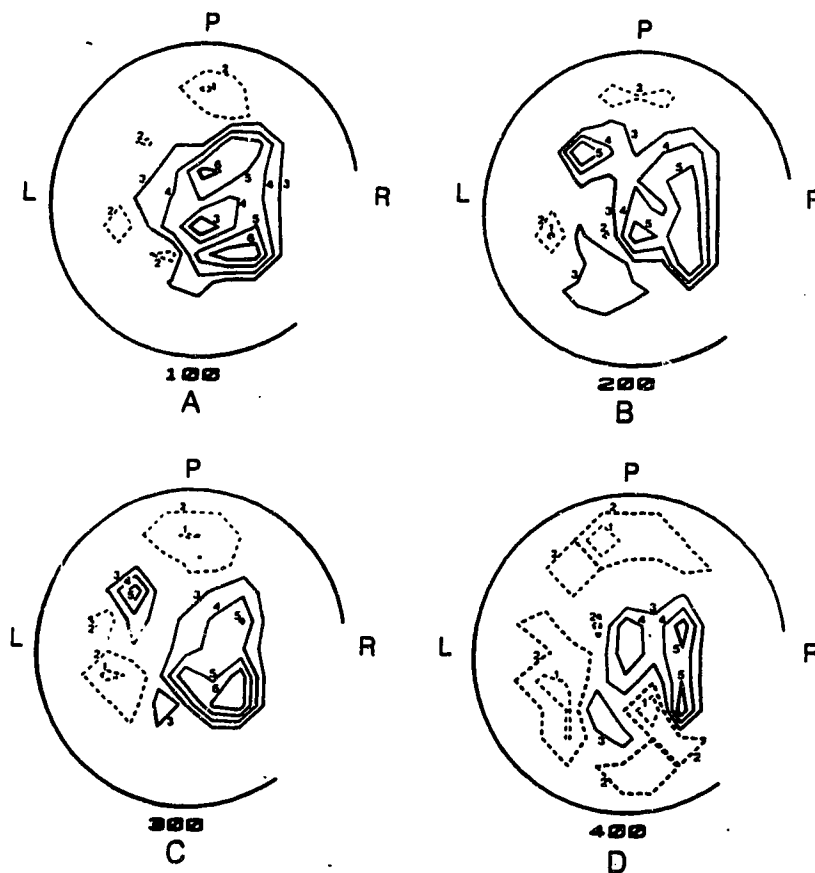


Figure 40. Cross-sectional model aortic velocity contours 0.5 cm downstream of the right renal artery origin under conditions of steady upstream flow (1197 ml/min). The right renal flow is 56 percent of the upstream flow and contours correspond to 100(A), 200(B), 300(C), and 400(D) msec after the triggering spike for waveform sampling. L: left, R: right, P: posterior(dorsal). The circular frame surrounding each set of contours is broken to indicate the circumferential location and size of the origin of the right renal artery. Contour velocities are, in cm/sec: A: 1:-14.0, 2:-5.5, 3:3.0, 4:11.5, 5:20.0, 6:28.4, B: 1:-15.0, 2:-6.9, 3:1.2, 4:9.3, 5:17.3, C: 1:-8.0, 2:-1.3, 3:5.3, 4:12.0, 5:18.7, 6:25.3, D: 1:-6.5, 2:-0.1, 3:6.4, 4:12.9, 5:19.3.

patterns in figure 40 is the same as that of figure 38(D). Therefore figure 38(D) is not completely representative of the velocity field in question. Nevertheless it has a number of features in common with the contour diagrams of figure 40. First, there is in all of the contour diagrams a zone of high forward velocity near the right renal branch ostium. Second, there is a common region of reverse velocity in the most peripheral dorsal aspect of the aorta. Third, and finally, each contour diagram has a region of reverse velocity along the left ventral aspect of the aorta. Thus although parts of the velocity field fluctuate with time certain features persist. The key persistent features are the previously described paired zones of reverse velocity on either side of the aortic diameter in the plane of the renal branch.

Pulsatile Flow

Figure 41 presents centrestream *in vitro* pulsatile aortic velocity waveforms for three different right renal branch flows. The increase in branch flow from zero to 32 percent of aortic flow appears to markedly reduce peak centrestream aortic velocity from well above 46 cm/sec (figure 41(A)) to well below 46 cm/sec (figure 41(B)). Part of this reduction may be due to a simultaneous decrease in mean aortic flow from 406 ml/min to 325 ml/min. However, the peak centrestream aortic velocity is still well below 46 cm/sec in figure

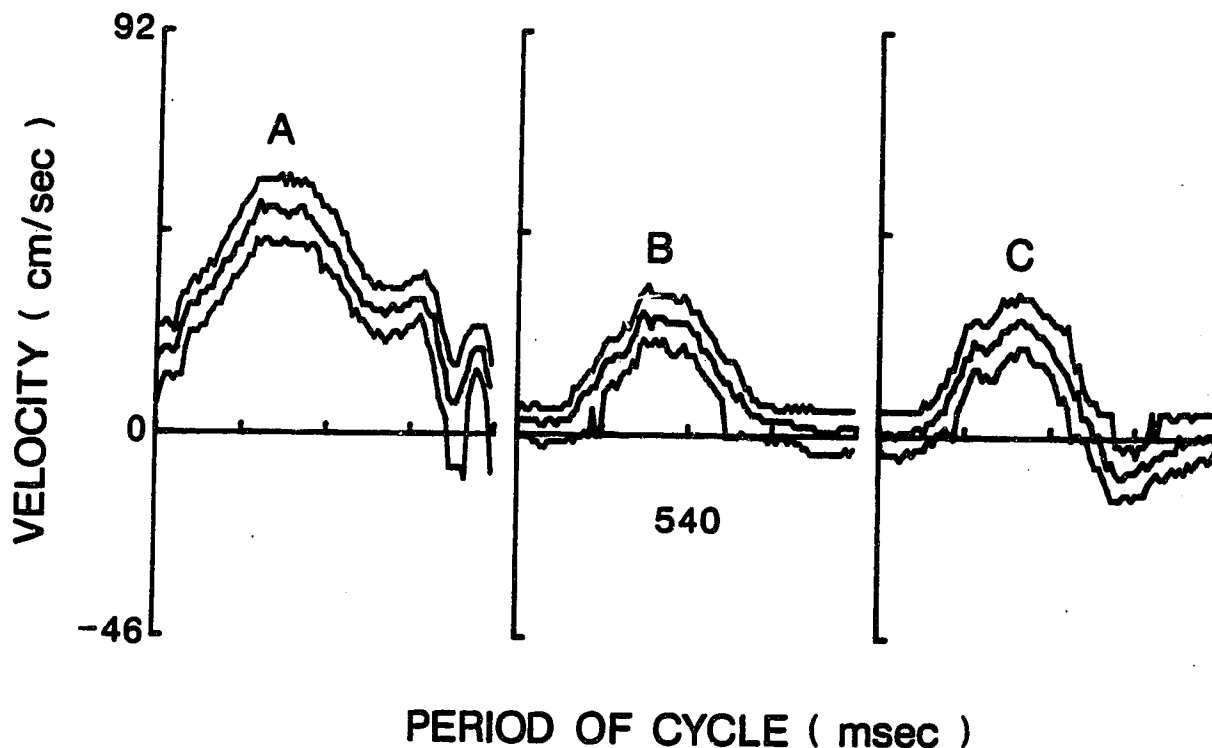


Figure 41. Centrestream model aortic velocity waveforms recorded 0.5 cm downstream of the right renal artery origin under conditions of pulsatile upstream flow with right renal flows of zero(A), 32(B), and 48(C) percent of mean aortic flow. In each case the velocity computed from the PDUVM mode frequency is surrounded by its 8 dB contour velocities. The pulse rate in each case is 105 beats per minute. The mean, peak, and minimum flowrates are, in ml per minute: A: 406, 1197, -385, B: 325, 1218, -487, and C: 390, 1218, -568.

41(C) where the aortic flow is only 16 ml/min below that of figure 41(A). This confirms the strong influence of right renal branch flow on centrestream aortic velocity. Also apparent in figure 41(C) is the increase in reverse flow velocity compared to the waveforms in figure 41(A) and 41(B).

Figure 42 presents model aortic velocity contours 0.5 cm downstream of the right renal artery origin recorded 200 msec after the sync pulse upslope with right renal flows of zero, 32, and 48 percent of mean aortic flow. The contours are all in the forward direction: this is not surprising since inspection of figure 41 reveals that the flow is near the peak of pulse acceleration at 200 msec into the pulse period. The contours of figure 42 show some correspondence with the waveforms of figure 41. For example, the peak velocity in figure 41(A) is above 46 cm/sec while the peak velocity in figure 41(B) and 41(C) is below 46 cm/sec. Similarly, in figure 42(A) the maximum contour velocity is about 34 cm/sec while figure 42(B) and 42(C) have maximum contour velocities near 23 cm/sec. The difference in velocity magnitudes between figures 41 and 42 is presumably due to the flow not being at the waveform peak in figure 42. As occurred in steady flow with zero branch flow there is symmetry in the contours along the aortic diameter in the plane of the renal branch in pulsatile flow (figure 42(A)). With 32 percent

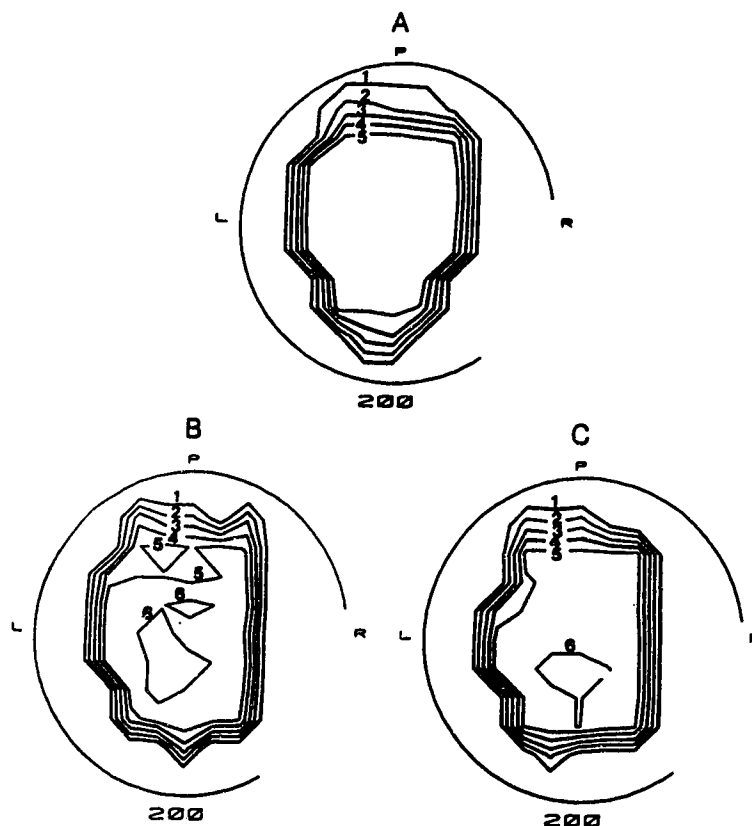


Figure 42. Cross-sectional model aortic velocity contours 0.5 cm downstream of the right renal artery origin under conditions of pulsatile upstream flow 200 msec after the sync pulse upslope with right renal flows of zero(A), 32(B), and 48(C) percent of mean aortic flow. L:left, R:right, P:posterior(dorsal). The circular frame surrounding each set of contours is broken to indicate the circumferential location and size of the origin of the right renal artery. Contour velocities are, in cm/sec: A: 1:1.3, 2:9.4, 3:17.5, 4:25.6, 5:33.6, B: 1:5.0, 2:8.6, 3:12.3, 4:15.9, 5:19.6, 6:23.2, C: 1:3.7, 2:7.5, 3:11.4, 4:15.2, 5:19.1, 6:22.9.

aortic flow through the right renal branch (figure 42(B)) there is a slight skewing of the contours toward the ventral aspect of the aorta. A similar contour skewing pattern is apparent with 48 percent of the aortic flow through the renal branch (figure 42(C)).

Figure 43 presents pulsatile flow model aortic velocity contours at four different times in the pulse cycle when the right renal branch flow is 32 percent of mean aortic flow. Reference to figure 41 makes it clear that the four times presented are well after the flow peak and the last two (figures 43(C) and 43(D)) are close to the minimum flow point of the pulse cycle. Thus it is not surprising that the minimum contour velocity decreases from -5.0 cm/sec in figure 43(A) to -7.4 cm/sec in figure 43(C). Similarly the centrestream zone of forward velocities decreases in size from figure 43(A) to 43(B), and is entirely absent in figure 43(C) and 43(D). Reverse velocities are present in all four contour diagrams and a feature common to all is a peaking of reverse velocities in the peripheral ventral and dorsal aspects of the aorta. These were the same regions where flow reversal occurred in steady flow, i.e. paired zones of reverse velocity opposite the right renal branch and lying on either side of the aortic diameter in the plane of the same branch.

Figure 44 is analogous to figure 43, the chief difference being that right renal branch flow has been

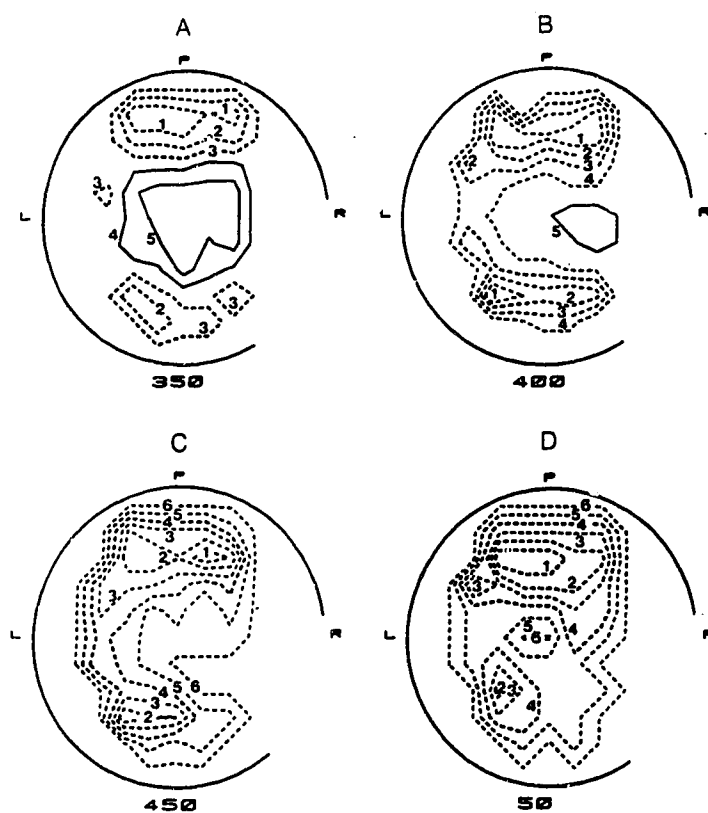


Figure 43. Cross-sectional model aortic velocity contours 0.5 cm downstream of the right renal artery origin under conditions of pulsatile upstream flow (peak 1218 ml/min, mean 325 ml/min) 350(A), 400(B), 450(C), and 50(D) msec after the sync pulse upslope with a right renal flow of 32 percent of mean aortic flow. L:left, R:right, P:posterior(dorsal). The circular frame surrounding each set of contours is broken to indicate the circumferential location and size of the origin of the right renal artery. Contour velocities are, in cm/sec: A: 1:-5.0, 2:-2.8, 3:-0.6, 4:1.7, 5:3.9, B: 1:-7.0, 2:-5.2, 3:-3.4, 4:-1.5, 5:0.3, C: 1:-7.4, 2:-6.0, 3:-4.6, 4:-3.2, 5:-1.8, 6:-0.3, D: 1:-4.1, 2:-3.3, 3:-2.5, 4:-1.7, 5:-0.9, 6:-0.1.

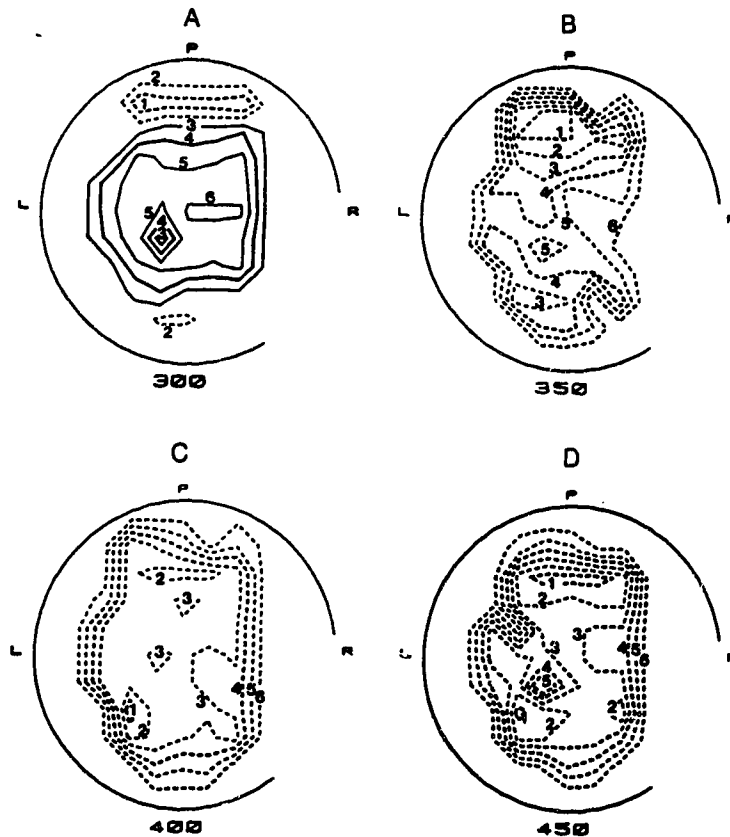


Figure 44. Cross-sectional model aortic velocity contours 0.5 cm downstream of the right renal artery origin under conditions of pulsatile upstream flow (peak 1218 ml/min, mean 390 ml/min) 300(A), 350(B), 400(C), and 450(D) msec after the sync pulse upslope with a right renal flow of 48 percent of mean aortic flow. L:left, R:right, P:posterior(dorsal). The circular frame surrounding each set of contours is broken to indicate the circumferential location and size of the origin of the right renal artery. Contour velocities are, in cm/sec: A: 1:-4.8, 2:-2.0, 3:0.9, 4:3.7, 5:6.5, 6:9.3, B: 1:-14.4, 2:-12.0, 3:-9.6, 4:-7.1, 5:-4.7, 6:-2.3, C: 1:-16.9, 2:-13.7, 3:-10.4, 4:-7.2, 5:-4.0, 6:-0.7, D: 1:-10.2, 2:-8.4, 3:-6.6, 4:-4.8, 5:-2.9, 6:-1.1.

increased to 48 percent of mean aortic flow. This increase clearly affects the the velocity field since the minimum contour velocities, which are reverse for both branch flows, are higher with 48 percent branch flow. As in figure 43 zones of forward flow disappear as the flow pulse decelerates. This disappearance occurs earlier in the pulse cycle (350 msec) in figure 44, indicating a more extensive flow reversal than was seen at the lower branch flow. Finally, as in figure 43, paired pockets of peak reverse flow persist over the four pulse times indicated. They are situated, again, opposite the right renal branch and lie on either side of the aortic diameter in the plane of the same branch.

D. FACTORS AFFECTING PDUVM SPECTRAL WIDTH

Steady Laminar Flow

In the frequency profile of figure 16 the width of the spectra increases, independent of the shift to higher frequencies towards centrestream, as the sample volume is range-gated across the tube. Three plots of mode-based spectral width, measured as described in the methods, are shown in figure 45. The first plot (diamond) represents the measurements from the 20 MHz PDUVM spectra illustrated in figure 16. In this experiment signal amplitude was maintained constant by increasing gain with increasing distance from the transducer. There is an apparent increase

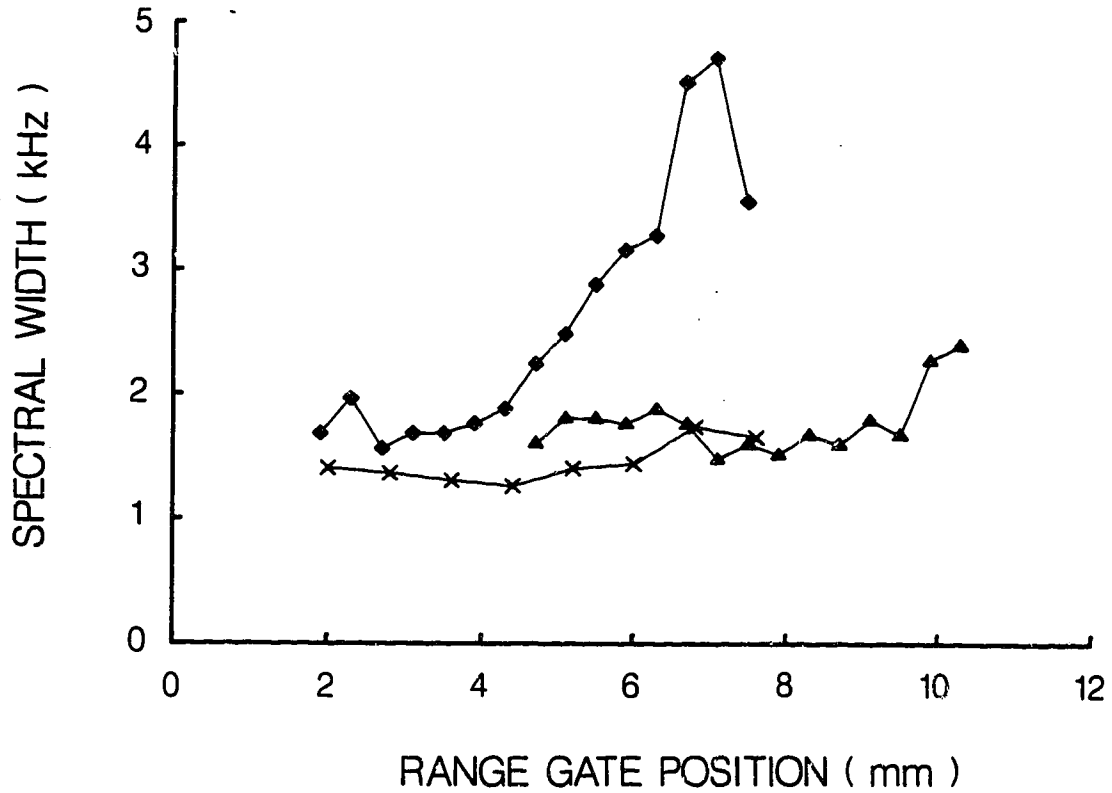


Figure 45. The variation of 20 and 10 MHz PDUVM spectral width across the test section vertical diameter under conditions of laminar flow at a Reynolds number of 462. 20 MHz PDUVM with constant signal amplitude (diamond). 20 MHz PDUVM with constant amplifier gain (hatch). 10 MHz PDUVM with constant signal amplitude (triangle).

in spectral width as the sample volume is ranged away from the probe. The second plot (hatch) was made with the 20 MHz PDUVM under the same flow conditions but with constant amplifier gain. Under these conditions there remains a slight increase in spectral width with increasing range. This effect was greatly amplified by the attempt to maintain a constant signal level. The effect is considered in the discussion and is thought to be due to noise introduced by use of the instrument towards the extremes of its range. The third plot (triangle) is that of the 10 MHz PDUVM spectral width recorded with constant signal amplitude. The 10 MHz spectral width clearly remains constant over a much more extensive range than the 20 MHz PDUVM width.

Post-stenotic Flow with Steady Flow Upstream

A composite illustration of the results from a flow visualization study downstream of the 0.19 cm (90 percent) stenosis using a tube Reynolds number of 316 is shown in figure 46. The central jet region of high velocity particles is shown by the centrally placed streaks. On either side of this, slow moving particles representing flow separation can be seen. Just downstream of the tip of the jet, the pattern of particle movement is complex and disturbed in the region of turbulence.

Data from an axial sampling site 0.6 cm (one diameter) downstream of the 0.19 cm (90 percent) stenosis is illustrated in figure 47. This site corresponds to the left

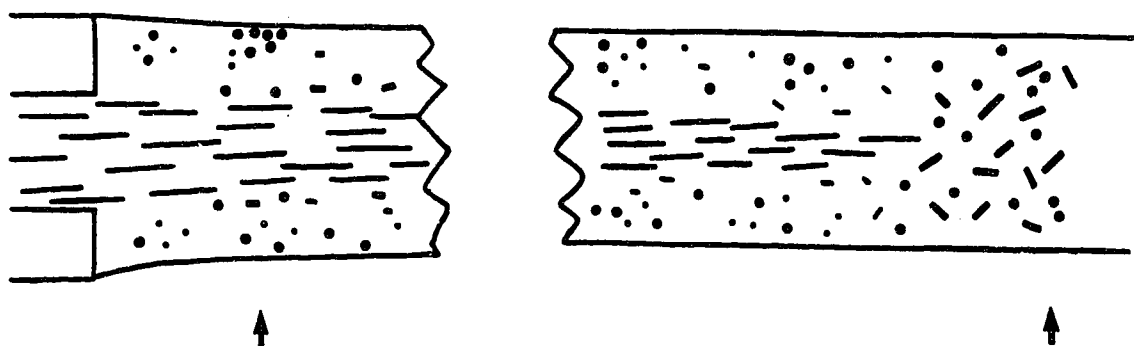


Figure 46. Schematic of the results of flow visualization downstream of the 0.19 cm (90 percent) stenosis at a tube Reynolds number of 316. The arrows point to key axial positions referred to in the text.

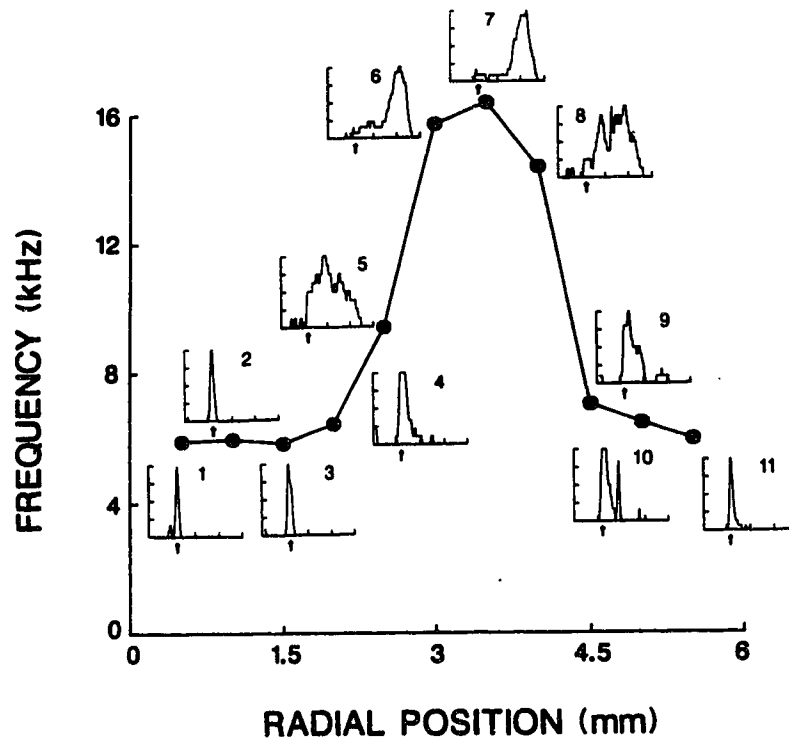


Figure 47. Mode frequency velocity profile across the tube 6 mm (one diameter) downstream of the 0.19 cm (90 percent) stenosis at a tube Reynolds number of 316. The spectra from which mode frequencies were derived are superimposed. For each spectrum the ordinate is relative amplitude normalized to each maximum. The abscissa is frequency in kHz with a 20 kHz maximum. The offset frequency of 6 kHz (zero velocity) is indicated by an arrow under each spectrum.

hand arrow in figure 46. The spectra recorded across the tube at a tube Reynolds number of 316 are shown superimposed on a velocity profile developed from mode frequencies. The low velocities close to the wall, on either side of the high jet velocities, represent the recirculation demonstrated in figure 46. The predominant direction of particle movement at the near wall is reverse. Mode frequencies are less than the shift frequency of 6 kHz at positions 1, 2, and 3. At the far wall, the direction of the low velocities in the separation region are mixed. They are forward at positions 9 and 10 but reverse at position 11.

The widths of the individual spectra in figure 47 vary across the tube. There is a bimodal distribution with two peaks on either side of the centre. This is more clearly seen in figure 48 which depicts the profile of relative spectral width for this experiment. Relative spectral width (spectral width/mode frequency) is used to compensate for the relationship of spectral width to velocity demonstrated with the laminar flow model. The highest spectral widths occur on either side of the two central spectra. Comparison with the flow visualization picture in figure 46 suggests that the broad spectra on either side of centre are due to the placement of the sample volume in the shear layer between jet and recirculation.

In figure 49 the variation of centrestream relative spectral width with post-stenotic axial position is shown for the 0.19 cm (90 percent) stenosis at a Reynolds number

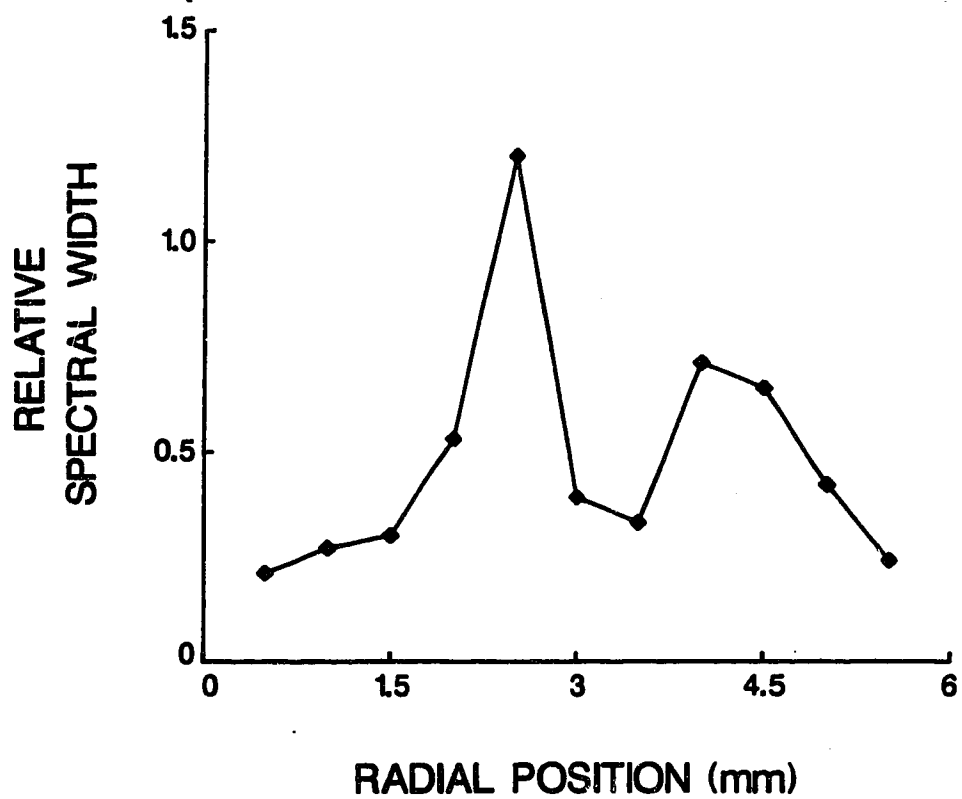


Figure 48. Relative spectral width profile across the tube 6 mm (one diameter) downstream of the 0.19 cm (90 percent) stenosis at a tube Reynolds number of 316.

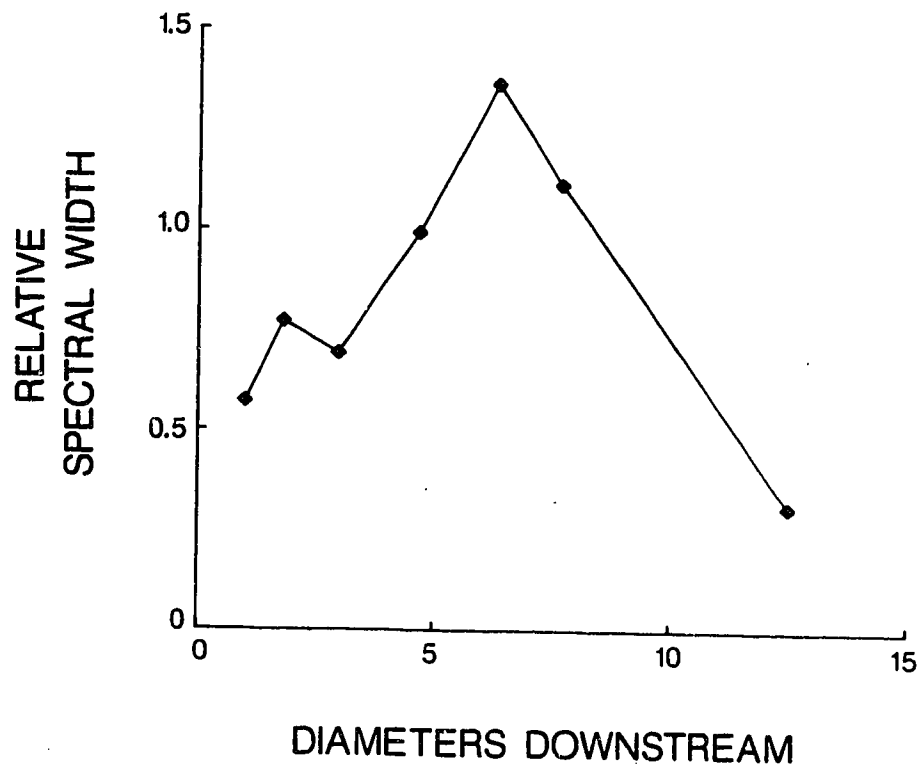


Figure 49. Axial variation of centrestream relative spectral width downstream of the 0.19 cm (90 percent) stenosis at a tube Reynolds number of 717.

of 717. Maximum centrestream spectral width occurs at 7 diameters downstream. A similar pattern occurred at all flow rates used with the 90 percent and 77 percent stenoses, Table 6. That is, maximum centrestream spectral width occurred at some finite distance downstream of the stenosis. Comparison with flow visualization showed that the point of maximum centrestream spectral width coincided with jet break up (right hand arrow, figure 46). With the lowest grade stenosis (56 percent), relative spectral width did not vary with downstream distance at the two lower flow rates. With the highest flow rate (Reynolds number 985) centrestream spectral width increased at 7.5 diameters downstream and was still similarly raised at 13.5 diameters downstream. This pattern was similar to that recorded for the 77 percent stenosis at the lowest flow rate.

Figure 50 shows the relationship between maximum centrestream spectral width and tube Reynolds number for both the laminar flow (zero stenosis) and post-stenotic experiments. For each stenosis grade, a linear relationship is suggested. At any given Reynolds number, spectral width is increased with increasing stenosis grade.

Post-stenotic Flow with Pulsatile Flow Upstream

Spectral Waveforms and Flow Visualization

Figures 51 to 55 show centrestream pulsatile flow spectral waveforms recorded with the 20 MHz PDUVM at 0.6, 1.6, 2.6, 3.6, and 14.8 cm downstream of the 1.9 mm

Sten. Area	Re. No.	Relative spectral width as a function of post-stenotic axial position (diameters downstream)													
		1.0	1.8	2.7	3.5	4.3	5.2	6.0	6.8	7.7	8.5	9.3	11.0	12.7	13.5
56%	349	0.27	0.30	-	0.26	-	-	-	0.26	-	-	-	-	-	0.28
56%	628	0.30	0.32	0.29	0.29	-	0.30	-	-	-	0.25	-	-	-	0.26
56%	985	0.25	0.30	0.29	-	0.27	-	0.34	-	0.55	-	0.48	-	<u>0.62</u>	<u>0.62</u>
77%	332	0.28	-	-	0.26	-	-	0.25	-	0.68	-	<u>0.86</u>	-	-	-
77%	656	0.63	0.51	<u>0.79</u>	-	0.77	-	0.54	-	-	-	0.56	-	0.37	-
77%	952	0.57	0.77	0.69	-	0.99	-	<u>1.36</u>	-	1.11	-	-	-	0.63	-
90%	316	0.33	-	0.45	-	0.56	-	-	-	<u>1.40</u>	-	-	0.63	-	-
90%	520	0.23	-	0.26	-	1.12	1.39	1.35	<u>1.54</u>	-	0.54	-	-	-	-
90%	717	0.64	0.82	1.08	-	<u>1.51</u>	-	0.85	-	0.57	-	-	-	0.24	-

Table 6. Variation of centrestream relative spectral width with axial location downstream of the three stenoses at three Reynolds numbers (Re. No.) each. Maximum values are underlined.

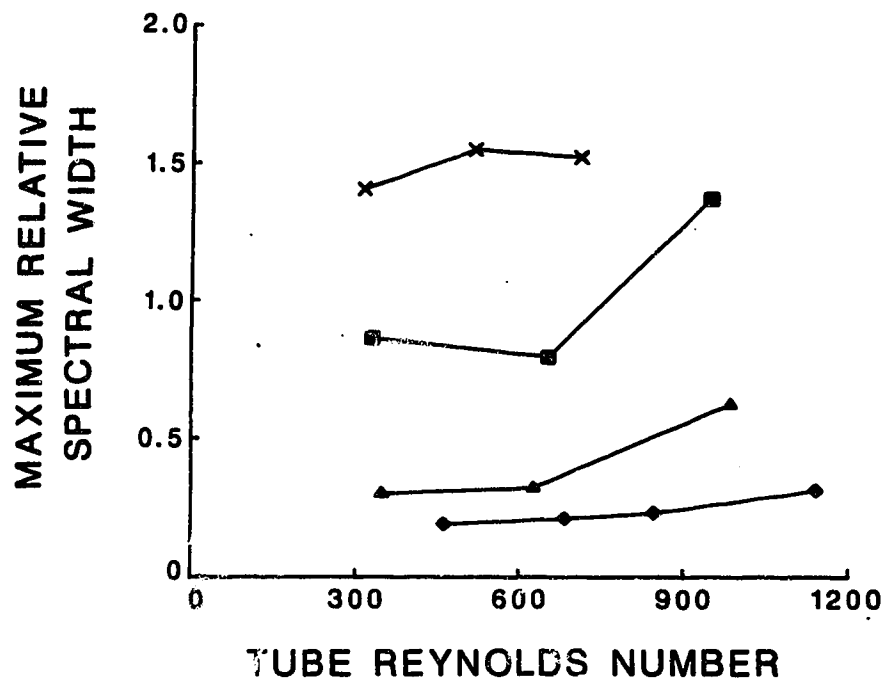
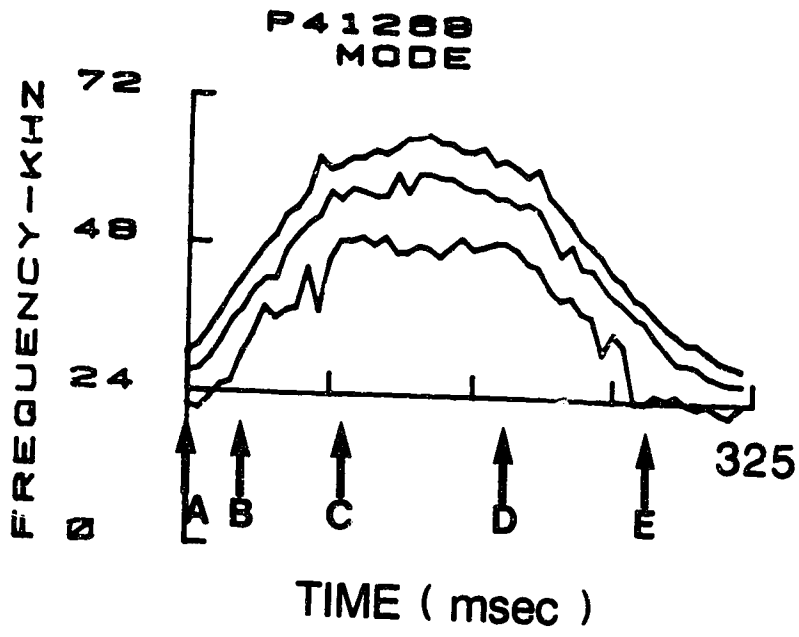


Figure 50. The variation of maximum relative spectral width with tube Reynolds number in the unstenosed tube (diamond), and downstream of the 0.4 cm (56 percent) stenosis (triangle), the 0.29 cm (77 percent) stenosis (square), and the 0.19 cm (90 percent) stenosis (hatch).

stenosis. Each spectral waveform consists of the recorded mode frequency surrounded by its 8 dB contours. Each figure contains a set of cinefilm frames taken from the flow visualization record for that axial location at five selected times in the pulse cycle. The times selected are varied between figures in order to illustrate specific features of the different waveforms. The selected times are marked with arrows along the time axis of each spectral waveform. In each figure the position of the PDUVM sample volume is indicated with a white circle in one of the post-stenotic cinefilm frames. The sample volume position is the same in each frame for a given figure.

Figure 51 shows a centrestream spectral waveform recorded immediately (0.6 cm) downstream of the stenosis. The chief features to be seen are the high magnitude (over 50 kHz) of the mode frequencies attained and the sinusoidal shape of the waveform. The spectral width remains relatively constant over the pulse cycle, increasing somewhat during the peak frequency phase. The increased absolute width at the waveform peak probably is due to the effect of increased flow velocity on the PDUVM spectrum. Since the mode frequency is also elevated at this point in the waveform, the relative spectral width (absolute width/mode frequency) is almost constant over the pulse cycle.

Figure 51. Centrestream spectral waveform recorded 0.6 cm downstream of the 1.9 mm stenosis accompanied by the flow visualization record at the same axial location (right, p. 144b). The flow visualization panels labelled A,B,C,D, and E correspond to the times marked in the pulse cycle with arrows and the same letters. The position of the PDUVM sample volume is indicated by a small circle in flow visualization panel C. The sample volume position is the same in the other four panels.

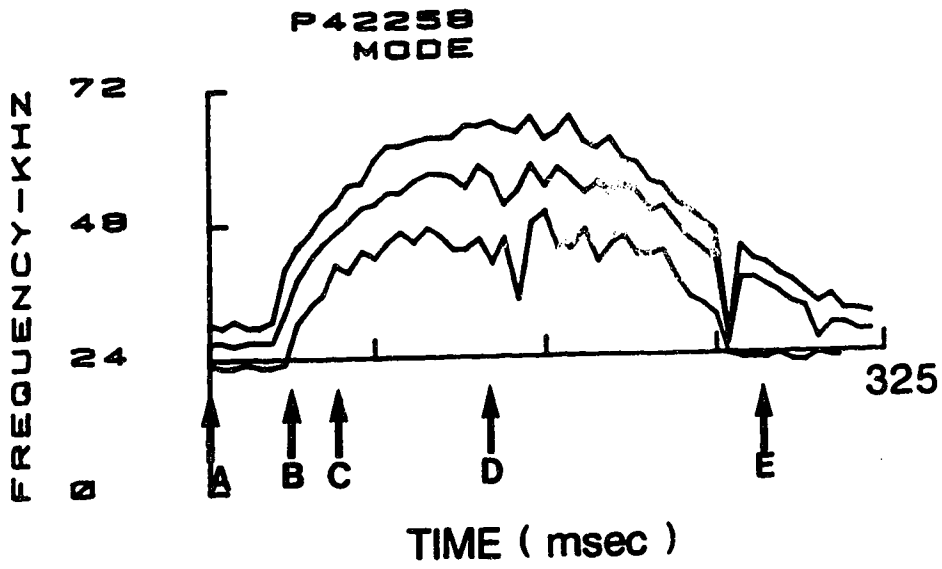


- A [REDACTED]
- B [REDACTED]
- C [REDACTED]
- D [REDACTED]
- E [REDACTED]

All frames of the corresponding flow visualization record show a central jet flanked by recirculation zones towards the walls, as previously described in the pulsatile velocity profiles section. The oscillatory nature of the flow is indicated by the varying lengths of the streaks in the central jet region from frame to frame. In frame A, at the beginning of the pulse cycle, the particles emerging from the stenosis make short axial streaks, indicating low jet velocities. In frame B, during the acceleration phase of the pulse cycle, the emerging particles make longer streaks, thus indicating increased jet velocities. In frames C and D, near the peak of the pulse cycle, the emerging particle streaks are so long that they merge with one another, indicating very high jet velocities. In frame E, during the deceleration phase, the jet particle streaks are shorter than those in the preceding frame, indicating that the jet velocity is decreasing. In all frames the major component of midline velocity is in the axial direction. There is no indication of disordered flow. Thus it is not surprising that the relative spectral width remains essentially constant through the waveform.

Figure 52 shows a centrestream spectral waveform recorded 1.6 cm downstream of the 1.9 mm stenosis. Again, mode frequencies over 50 kHz are attained at the waveform peak, indicating that the sample volume is still located in a jet velocity region. The waveform

Figure 52. Centrestream spectral waveform recorded 1.6 cm downstream of the 1.9 mm stenosis accompanied by the flow visualization record at the same axial location (right, p. 146b). The flow visualization panels labelled A,B,C,D, and E correspond to the times marked in the pulse cycle with arrows and the same letters. The position of the PDUVM sample volume is indicated by a small circle in flow visualization panel B. The sample volume position is the same in the other four panels.



- A [REDACTED]
- B [REDACTED]
- C [REDACTED]
- D [REDACTED]
- E [REDACTED]

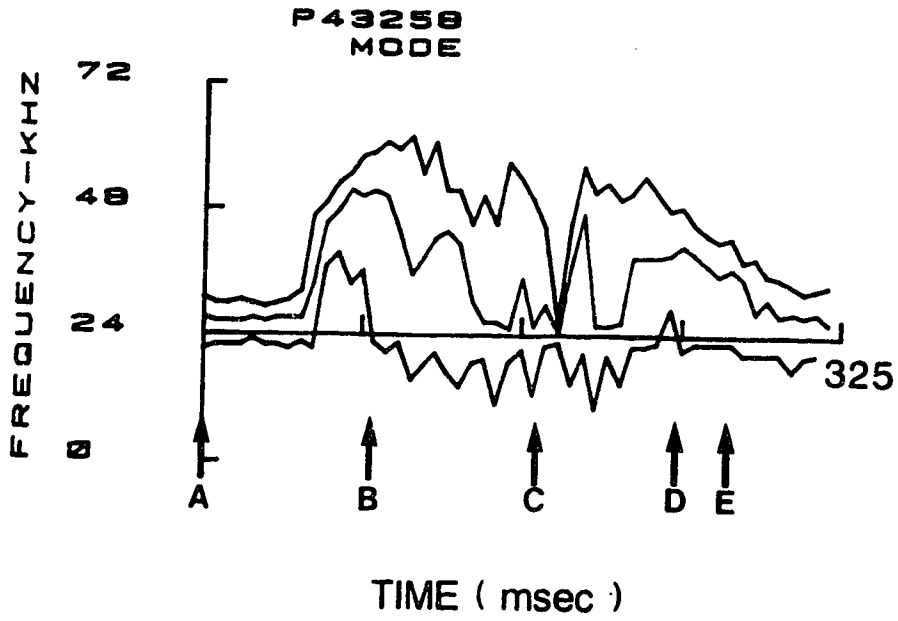
shape is somewhat distorted from the sinusoidal shape of the preceding figure. There is a flat region lasting about 30 msec before the onset of pulse acceleration. Spectral width varies more over the pulse cycle than in the waveform recorded at 0.6 cm downstream. In particular, there is a greater increase in absolute spectral width just past the peak of the pulse cycle. Thus the relative spectral width is increased more at this time in the pulse cycle in relation to the relative width at the same time 0.6 cm downstream of the stenosis.

The flow visualization record in figure 52 also differs from the visualization data of figure 51. In frame A the low velocities prior to flow acceleration are apparent in the short streak lengths of the centrestream particles. In frame B flow acceleration is readily apparent in the increased centrestream streak lengths relative to the previous frame. Frame B also gives the impression of a less organized jet than at 0.6 cm downstream. Frame C, exposed during late flow acceleration, shows high jet velocities in the fused streaking of centrestream particles. Frame D, exposed near the time of peak spectral broadening, shows a centrestream region with fused streaking that appears less axially oriented than the streaking revealed during late acceleration. There is a suggestion that the particles are moving radially, and they are out of

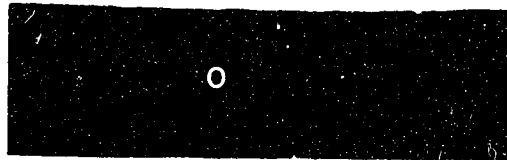
focus, as would be expected at a site of flow disturbance. In frame E deceleration of the flow is clearly evident in the shortness of the centrestream streaks relative to those in frame C. The single particle streak at the sample volume site is particularly demonstrative of the reduced velocity at this time in the pulse cycle. Also in frame E, reduction in flow disturbance is apparent in the increased axial orientation of the particle streaks relative to those in frame D.

Figure 53 shows a centrestream spectral waveform recorded 2.6 cm downstream of the 1.9 mm stenosis. Mode frequency varies markedly over the pulse cycle and does not exhibit the sinusoidal shape of the waveform at 0.6 cm downstream. Like the waveform at 1.6 cm downstream there is a short flat region before pulse acceleration. After acceleration the mode frequency begins to fall, eventually reaching a minimum of approximately 26 kHz near the time labelled C in figure 53. After a brief spike the mode climbs to about 36 kHz, stays there for about 40 msec, then gradually declines back to 26 kHz toward the end of the pulse cycle. Absolute spectral width also varies considerably over the pulse cycle: it is narrow before and during pulse acceleration, then broadens dramatically and remains broad for about 100 msec, decreases transiently, broadens again, and finally decreases during pulse deceleration at the end of the

Figure 53. Centrestream spectral waveform recorded 2.6 cm downstream of the 1.9 mm stenosis accompanied by the flow visualization record at the same axial location (right, p. 149b). The flow visualization panels labelled A,B,C,D, and E correspond to the times marked in the pulse cycle with arrows and the same letters. The position of the PDUVM sample volume is indicated by a small circle in flow visualization panel A. The sample volume position is the same in the other four panels.



A



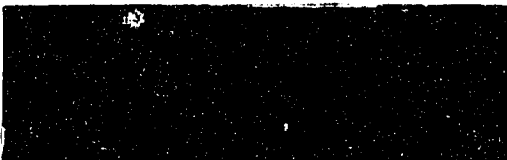
B



C



D



E



cycle. The dramatic broadening of the spectral width evident in this type of waveform will, in future, be referred to as 'bursting.' Compared to the two previous axial positions the absolute spectral width is considerably broader and remains broad for a longer period. Relative spectral width also is broader due to the effects of increased absolute width and decreased mode frequency. The corresponding velocity profiles which were presented in figure 31, parts (D) and (E), indicate that peak velocity is off centre when mode frequency is reduced in mid cycle.

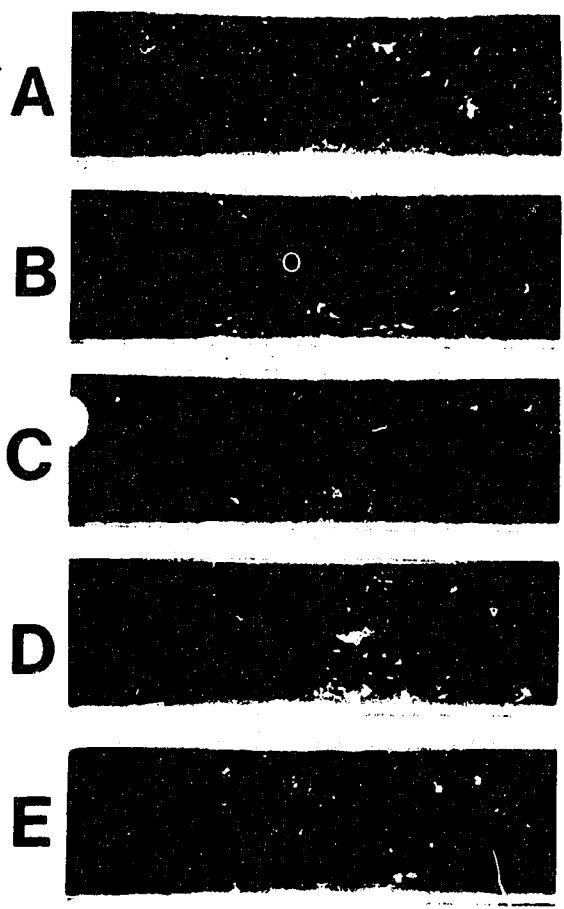
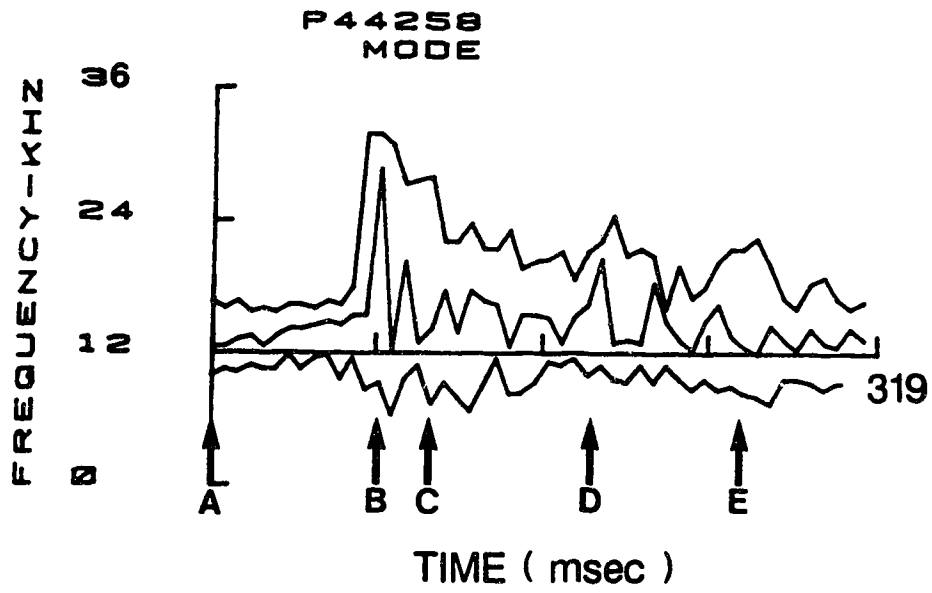
The flow visualization record reflects the disturbed features of the waveform at 2.6 cm downstream of the stenosis. In frame A flow velocities are very low, as demonstrated by the nearly spherical shape of the centrestream particles. In frame B, at the point of peak mode frequency, the high jet velocities are apparent in the long axial streaking of the centrestream particles. There is also evidence of flow disturbance causing the spectral broadening, since the axial streaks are out of focus. Frame C, exposed at a time of decreased mode frequency and spectral width, shows axial streaking of shorter length than that of frame B. Thus the reduction in flow velocity is demonstrated. Frame D, exposed at a time when the mode frequency is high again, exhibits centrestream streaks longer than those in frame C, as would be expected in a region of increased

velocity. The streaks are out of focus, however, indicating disturbed flow which would account for the broad spectrum. In frame E flow deceleration is apparent in the shorter centrestream streak lengths compared to those of frame D.

Figure 54 shows a centrestream spectral waveform recorded 3.6 cm downstream of the 1.9 mm stenosis. Like the waveform recorded at 2.6 cm downstream of the stenosis this waveform is not at all sinusoidal in shape. There is a slow rise in mode frequency from 13 kHz at time A until just before time B. At time B there is a rapid acceleration and deceleration spike. This is followed by a fluctuating, unstable frequency for the rest of the pulse cycle. The highest mode frequency reached is in the neighbourhood of 28 kHz, which is considerably less than at the preceding three axial locations. Absolute spectral width is narrow (about 5 kHz) prior to the major acceleration/deceleration spike, increases rapidly during acceleration, reaches a maximum at the spike peak, declines to about 10 kHz, and remains at that width for most of the remaining cycle. Thus there is considerable spectral broadening in this waveform, both absolute and relative. This increased spectral width is, however, not as great as that seen at 2.6 cm downstream of the stenosis.

This conclusion is supported by the corresponding flow visualization record. In all frames except B most

Figure 54. Centrestream spectral waveform recorded 3.6 cm downstream of the 1.9 mm stenosis accompanied by the flow visualization record at the same axial location (right, p. 152b). The flow visualization panels labelled A,B,C,D, and E correspond to the times marked in the pulse cycle with arrows and the same letters. The position of the PDUVM sample volume is indicated by a small circle in flow visualization panel B. The sample volume position is the same in the other four panels.



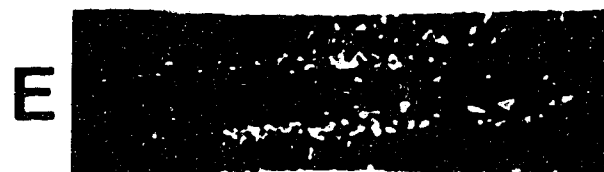
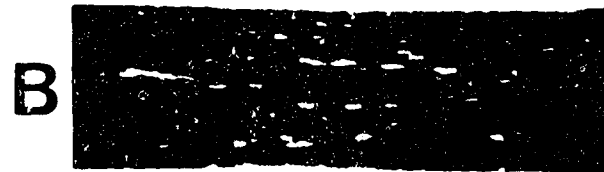
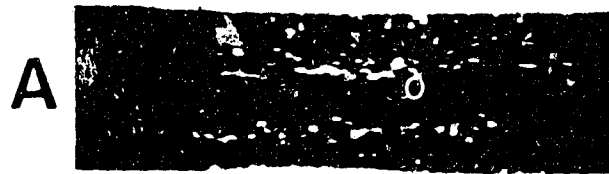
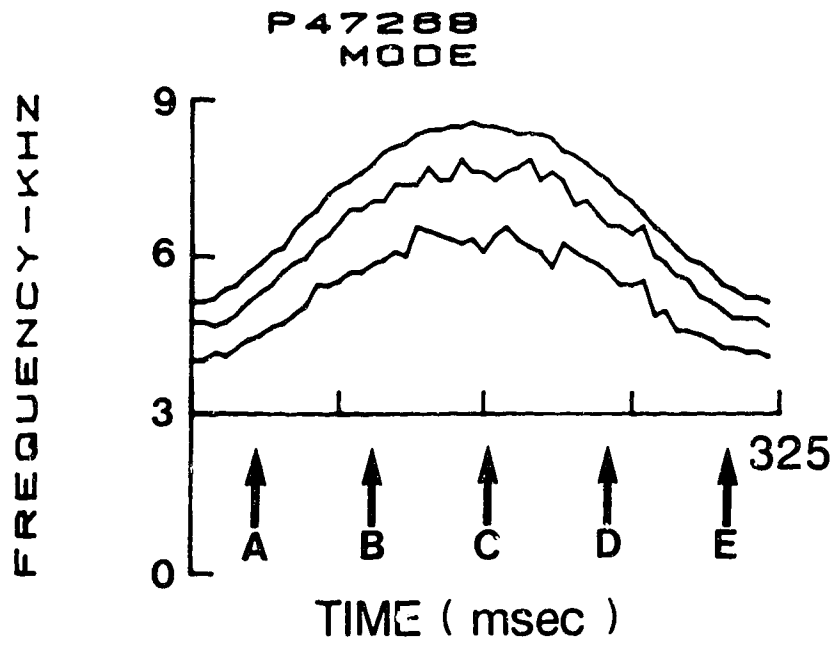
of the particles are not arranged linearly. Instead, they are highly disorganized. Furthermore, the apparent particle concentration across the tube is less than the concentration displayed far (14.8 cm) downstream of the stenosis in figure 55. The presence of disturbed flow can explain the apparent low particle concentration in figure 54 since turbulent flow would tend to distribute the particles across the whole tube cross section, away from the illuminated flow visualization slit. In frame A, prior to the major waveform spike, the centrestream particles are spherical in shape, thus suggesting low flow velocity, possibly directed at right angles to the flow axis. In frame B, at the point of peak mode frequency, there are centrestream axially oriented streaks indicative of high velocities. This is the only frame where axial streaks occur and is therefore the only frame with a suggestion of jet flow. The axial streaks are out of focus, though, suggesting flow disturbance. Frame C, exposed shortly after mode frequency has fallen from its peak, lacks centrestream axial streaks. The particles are spherical and randomly distributed. This would suggest flow disturbance and would explain the relatively high spectral width seen in the waveform. Frames D and E, exposed at later times in the pulse cycle, are very similar to frame C. Thus they confirm the prolongation of flow disturbance through the rest of the pulse cycle, as is suggested by the extended

broadening of the spectral waveform.

Figure 55 shows a centrestream spectral waveform recorded 14.8 cm downstream of the 1.9 mm stenosis. Flow disorder has clearly dissipated and the waveform has returned to a sinusoidal shape. High velocity jet flow has ceased, as evidenced by the low (approximately 7.5 kHz) peak mode frequency attained. Absolute spectral width exhibits a small increase in the region of the pulse peak but relative spectral width remains essentially constant over the pulse cycle.

The corresponding flow visualization record in figure 55 reflects the above suggestions of orderly flow. In all frames the particles are arranged in regular, axially oriented patterns. Frame A, exposed during early pulse acceleration, reveals short particle streaking. Later in the pulse cycle, in frame B, the particle streaks are longer, thus indicating increased velocity. Frame C, exposed at the peak of the pulse cycle, reveals even longer streaks, many of them overlapping with their neighbours. In frame D pulse deceleration is apparent in the reduced streak lengths relative to frame C. Frame E, exposed at the end of the pulse cycle, contains nearly spherical, slightly streaked particles indicative of further reduction in flow velocity.

Figure 55. Centrestream spectral waveform recorded 14.8 cm downstream of the 1.9 mm stenosis accompanied by the flow visualization record at the same axial location (right, p. 155b). The flow visualization panels labelled A,B,C,D, and E correspond to the times marked in the pulse cycle with arrows and the same letters. The position of the PDUVM sample volume is indicated by a small circle in flow visualization panel A. The sample volume position is the same in the other four panels.



Influence of Pulse Rate on Spectral Width

Figure 56 presents the centrestream spectral waveforms recorded with the 20 MHz PDUVM at all six post-stenotic axial positions for the three pulse rates studied with the cam-based pulsatile unit. Immediately apparent in the figure is the variation in pulse rate as demonstrated by the three different pulse cycle periods. The basic waveform shape is shown by the undisturbed waveforms far (15 cm) downstream of the stenosis. Inspection of these reveals that the 51 BPM waveform has the most sinusoidal shape. The other two waveforms have distorted sine wave shapes, especially the 105 BPM waveform. The distortion occurs partly because the cam follower did not always follow exactly the different cams used in the pulsatile unit. It was necessary to use different cams at each pulse rate due to a variation in pulsatility when only one cam was used. This variation in pulsatility may have been due to viscoelasticity in the flow circuit. Another factor contributing to distortion of the 105 and 240 BPM waveform shapes was the effect of sampling. Sampling was at a fixed rate (6.25 msec) at all three pulse rates. This resulted in a lower number of samples per pulse at the higher pulse rates and, consequently, a lower resolution in the sampled waveforms corresponding to the higher pulse rates. It is also apparent in figure 56 that the undisturbed waveforms at each pulse rate commence at a

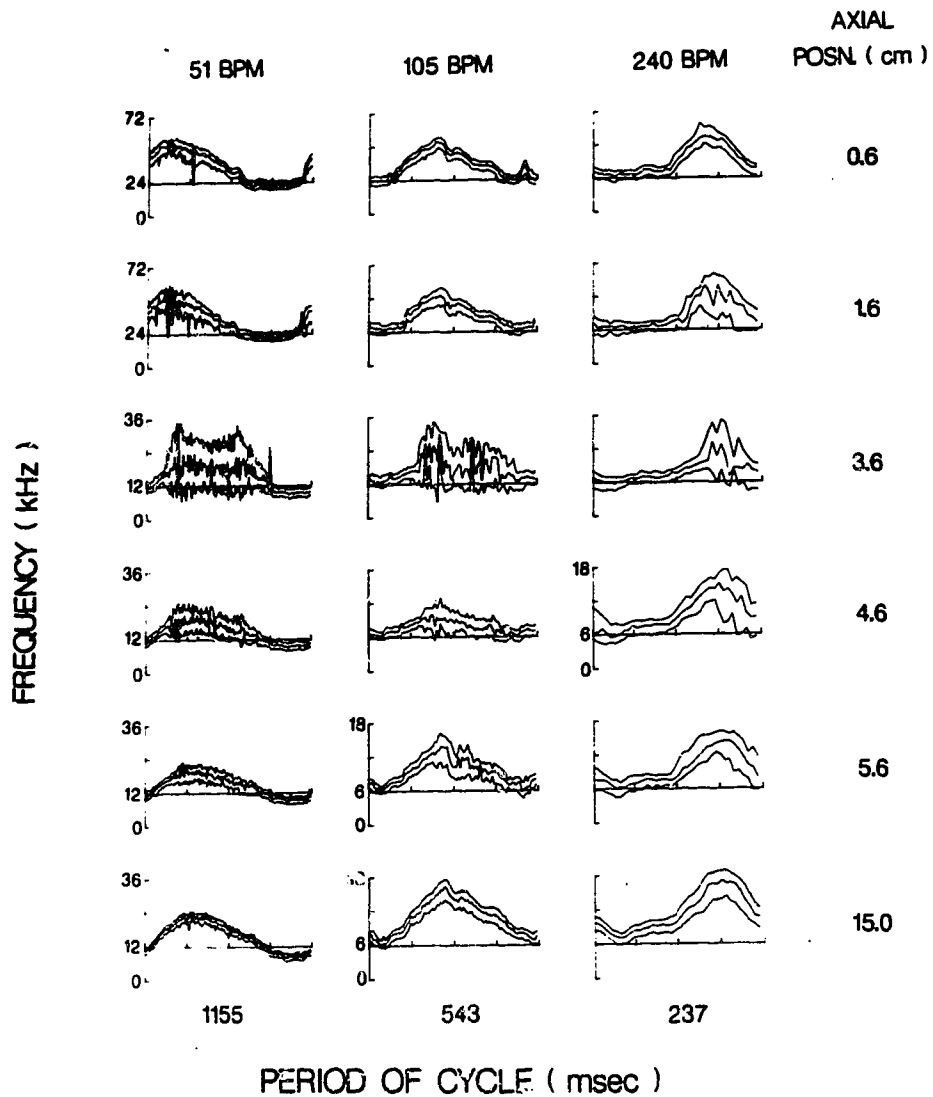


Figure 56. Centrestream spectral waveforms recorded with the 20 MHz PDUVM at all six post-stenotic axial positions (0.6 to 15 cm downstream) for the three pulse rates studied with the cam-based pulsatile unit. Pulse rates are indicated at the top of the figure in beats per minute (BPM).

different phase of the pulse cycle. This is due to the different cams generating sync pulses at different points in the pulse cycle. Figure 57 illustrates the different phase relationships between the electromagnetic flow waveforms and corresponding sync pulses generated by the cams of the three pulse rate experiments. The 51 BPM waveform at 15 cm downstream was triggered by the rising edge (arrow labelled A) of the corresponding sync signal. The 105 and 240 BPM waveforms at the same post-stenotic location were also triggered by their sync signal rising edges (arrows labelled C and D, respectively). Inspection of the three trigger arrows reveals that arrow A was closest to the start of its corresponding flow pulse acceleration, arrow C was next closest, and arrow D was farthest. Thus in figure 56 at 15 cm downstream of the stenosis the start of pulse acceleration is closest to the zero (trigger) time in the pulse cycle for the 51 BPM waveform and farthest from the zero time of the 240 BPM waveform. A final comment on the phase relationships of the spectral waveforms needs to be made. At 105 and 240 BPM the waveforms at all six axial positions start at the same point in the pulse cycle. This is not the case at 51 BPM where the waveforms at 0.6 and 1.6 cm downstream are out of sync with those at 3.6 to 15 cm downstream. This is because sampling of the waveforms at the former two locations was triggered by the falling edge of the sync

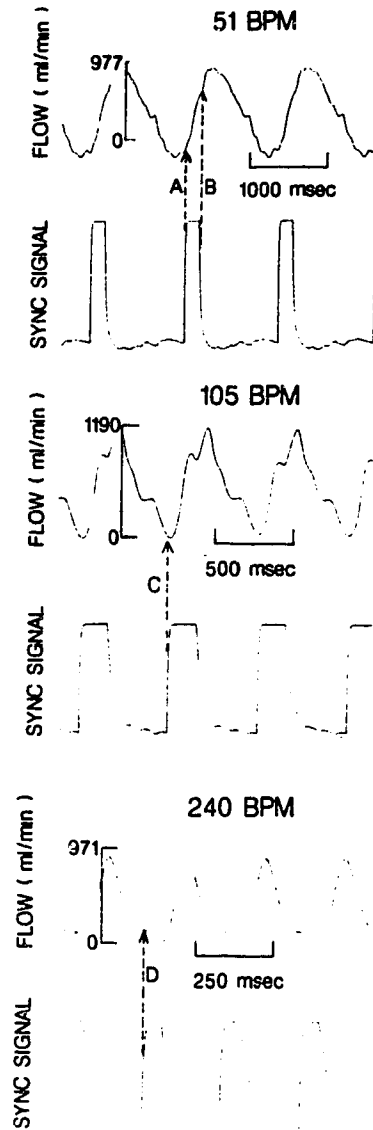


Figure 57. Simultaneous records of electromagnetic flow waveforms and corresponding sync pulses for the three pulse rate experiments using the cam-based pulsatile unit. Sampling of PDUVM waveforms was triggered by edges in the sync pulses labelled as arrows A,B,C, and D.

signal (arrow B in figure 57) as opposed to the usual triggering by the rising edge.

The axial variation of waveforms at all three pulse rates shares the basic features of the post-stenotic velocity field described in the section which compared spectral waveforms and simultaneous flow visualization. First of all, at 0.6 cm downstream of the stenosis, velocities are considerably elevated (the mode frequency is approximately 26 kHz above the offset frequency (24 kHz) at the pulse peak as compared to approximately 10 kHz above the offset frequency (12 kHz) at 15 cm downstream). This is due to jet flow emerging from the stenosis. Most important, for each pulse rate the spectral width 'bursts' at some finite distance downstream of the stenosis, as was demonstrated in figures 53 and 54. At more distal axial locations the flow disturbance gradually dissipates until at the sixth axial position (15 cm downstream) the waveforms are almost completely undisturbed. The bursting is most prominent at 3.6 cm downstream. At that location the amplitude of bursting is similar at all three pulse rates, but the duration is clearly greatest at 51 BPM and least at 240 BPM.

In order to determine if pulse rate affected post-stenotic turbulence production a computer program was used to analyze each spectral waveform of figure 56 with respect to the amplitude and duration of bursting

type flow disturbance. First, each waveform was subjected to ten passes through a symmetrical weighted average smoothing algorithm in order to reduce the noise in the Doppler waveform to a minimum. Figure 58 illustrates a smoothed spectral waveform and some of the parameters derived from it. A control spectral width (CW) was calculated just prior to pulse acceleration. Next, the program looked for the point at which the spectral width became greater than twice the control width. This point was called the burst start (BS). The program continued to search through the smoothed waveform until the spectral width fell below twice the control width. This point was called the burst end (BE). Thus the burst time (BE - BS) was the period between the burst start and the burst end. The mean absolute spectral width (MASW) over the burst was then calculated as the sum of the absolute spectral widths (ASW) over the burst divided by the burst time (BE - BS):

$$\text{MASW} = \Sigma \text{ASW} / (\text{BE} - \text{BS}) \dots \dots \dots (7)$$

The mean relative spectral width (MRELW) over the burst was calculated as the sum of the absolute spectral widths over the burst divided by the sum of the mode frequencies (M) over the burst:

$$\text{MRELW} = \Sigma \text{ASW} / \Sigma \text{M} \dots \dots \dots (8)$$

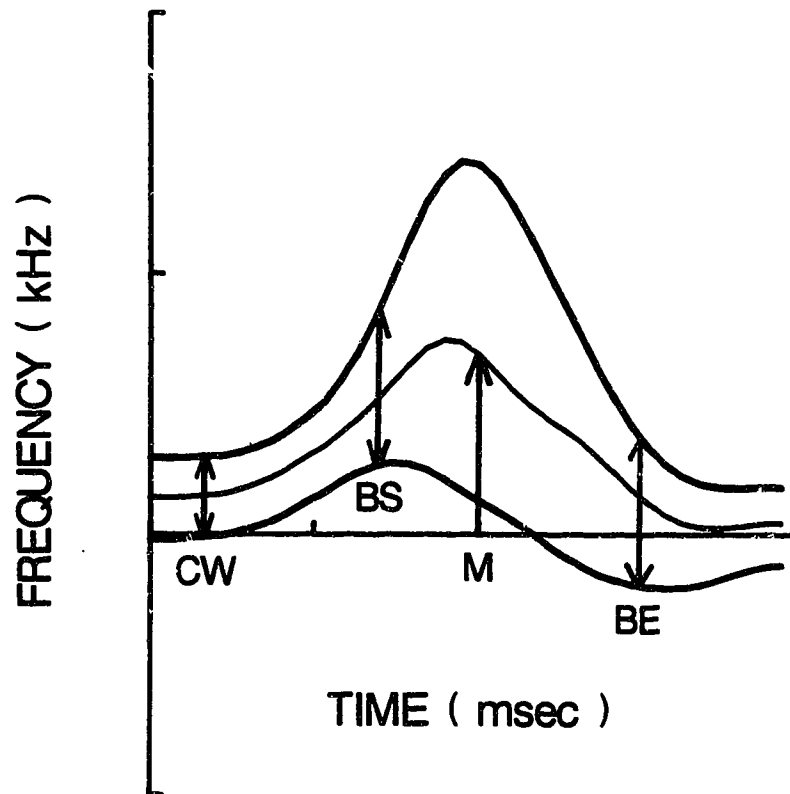


Figure 58. Diagram of smoothed PDUVM spectral waveform used to analyze the effect of pulse rate on post stenotic turbulence production. As in figures 6 and 51 to 55 the mode (M) frequency is surrounded by its 8 dB down contours which define the spectral width. CW - control spectral width, BS - turbulent burst start, BE - turbulent burst end.

If a burst start could not be found in a waveform, i.e. spectral width did not double, the waveform burst time, mean spectral width, and mean relative spectral width were set to zero.

For each spectral waveform two additional parameters were derived from those already calculated: the relative burst time (RELBT), and the time average relative spectral width (AVRLW). The former was calculated from the burst time divided by the pulse period (PP):

$$\text{RELBT} = (\text{BE} - \text{BS}) / \text{PP} \dots \dots \dots (9)$$

The time average relative spectral width was calculated from the product of the relative burst time and the mean relative spectral width in order to obtain a measure of the longterm exposure of the arterial wall to turbulent type flow disturbance:

$$\text{AVRLW} = \text{RELBT}(\text{MRELW}) \dots \dots \dots (10)$$

Table 7 displays the mean relative spectral width, relative burst time, and time average relative spectral width for each pulse rate at each post stenotic axial position. From the table it can be seen that mean relative spectral width peaks at 3.6 cm downstream of the stenosis at all three pulse rates, then decreases

Pulse Rate		51	105	240
Axial Posn.				
0.6	MRELW	0.7	0.0	0.5
	RELBT	0.89	0.0	0.08
	AVRLW	0.62	0.0	0.04
1.6	MRELW	0.7	0.6	1.4
	RELBT	0.50	0.09	0.59
	AVRLW	0.35	0.06	0.83
3.6	MRELW	2.6	2.1	2.2
	RELBT	0.64	0.65	0.45
	AVRLW	1.67	1.37	0.98
4.6	MRELW	1.6	1.7	1.5
	RELBT	0.52	0.46	0.41
	AVRLW	0.84	0.78	0.61
5.6	MRELW	0.8	0.8	1.1
	RELBT	0.26	0.31	0.30
	AVRLW	0.21	0.25	0.33
15.0	MRELW	0.0	0.4	0.6
	RELBT	0.0	0.12	0.35
	AVRLW	0.0	0.05	0.21

Table 7. Mean relative spectral widths (MRELW), relative burst times (RELBT), and time average relative spectral widths (AVRLW) obtained from the bursting analysis of the PDUVM waveforms of figure 56.

further downstream. A similar post-stenotic axial pattern of centrestream relative spectral width was observed when the upstream flow was steady (figure 49). Furthermore, as described previously, a comparison between post-stenotic PDUVM pulsatile waveforms and the corresponding flow visualization records revealed that spectral width increases to a maximum at some finite distance downstream, and at this location the visualized velocity field is highly disturbed (figures 53 and 54). Further downstream spectral width decreases in conjunction with a re-ordering of visualized flow elements (figure 55). The relative burst time in table 7 shows a similar rise to a peak followed by a decline at axial positions further downstream, except at 0.6 cm downstream of the stenosis at a pulse rate of 51 BPM. Thus the time average relative spectral width also peaks at 3.6 cm downstream of the stenosis. This pattern is illustrated in figure 59, which presents the variation of time average relative spectral width with post-stenotic axial position at all three pulse rates.

Table 7 also demonstrates that at the site of peak post-stenotic turbulence (3.6 cm downstream) the intensity of bursting flow disturbance, as reflected in the value of the mean relative spectral width, tends to decrease with increasing pulse rate. Since the relative burst time shows a similar pattern the time averaged turbulence, as reflected in the value of the time

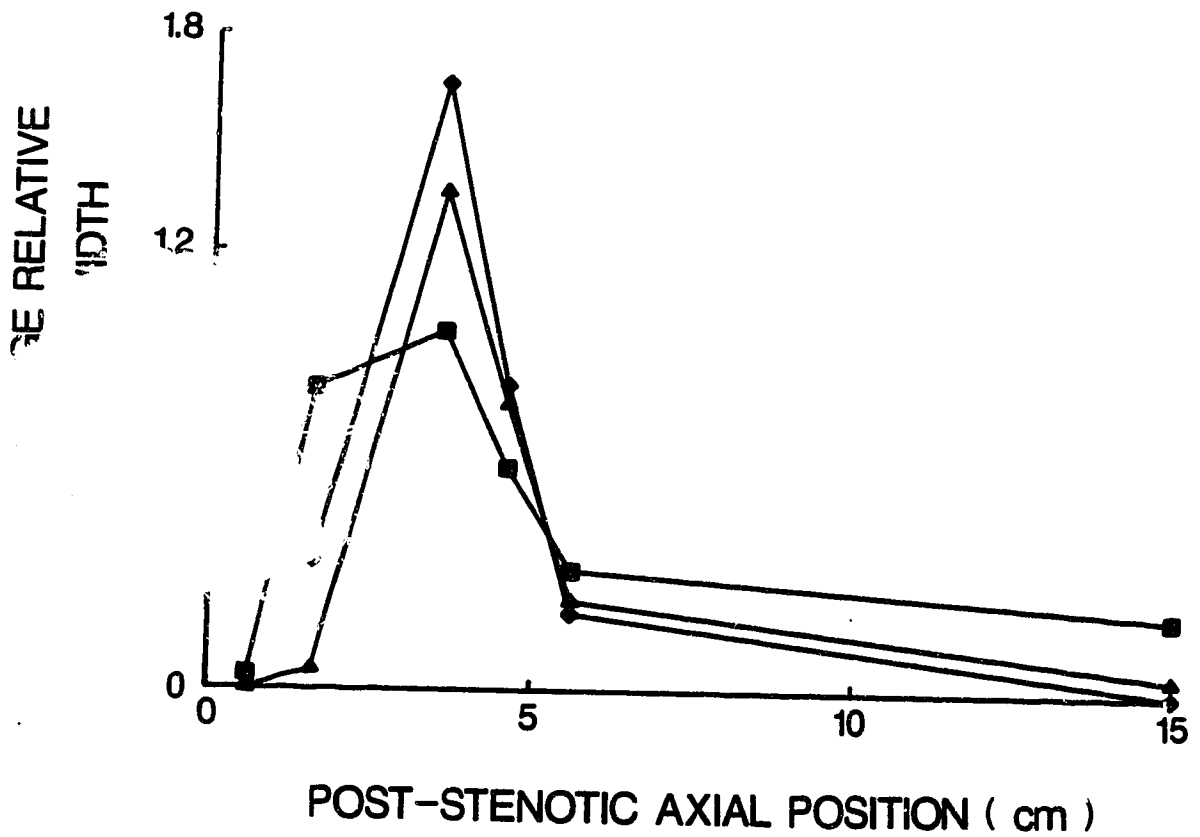


Figure 59. The variation of time average relative spectral width with post-stenotic axial position at the three pulse frequencies. Pulse frequencies are 51 BPM (diamond), 105 BPM (triangle), and 240 BPM (square).

average spectral width, decreases with increasing pulse rate (Table 7, Figure 59). Conversely, further downstream the reverse pattern is apparent. At 15 cm down all three parameters are greatest at 240 BPM and least at 51 BPM. This suggests that even though the intensity of turbulence is less at 240 BPM the axial propagation of turbulence at the same pulse rate is greater than at lower rates.

The above calculations concentrate on the bursting nature of post-stenotic turbulence in this *in vitro* model. *In vivo*, recordings suggest that turbulence often extends over most of the pulse cycle and the increase during the burst period is not as dramatic as in the *in vitro* results. A more appropriate measure of the time averaged disturbance in the *in vivo* situation would be the mean relative spectral width over the whole pulse cycle (WCMRW). This was calculated by another computer algorithm as the mean absolute spectral width over the whole cycle (WCMSW) divided by the mean mode frequency over the whole cycle (MMC).

$$\text{WCMRW} = \text{WCMSW}/\text{MMC} \dots \dots \dots (11)$$

The pattern observed using this parameter was similar to that of the time average relative spectral width. Thus whole cycle mean relative spectral width showed axial peaking at 3.6 cm downstream of the stenosis. The whole

cycle mean relative spectral width tended to decrease with increasing pulse rate at that location.

In addition, mean relative spectral width over the burst, relative burst time, and time average relative spectral width over the burst were recalculated with a modified computer program that used equations (8) to (10) and the same 200 percent burst width criterion, but an externally supplied control spectral width. The control spectral width was obtained by hand-measuring the minimum distance between contours at each axial location and pulse rate. The variation of these parameters with axial position and pulse rate was essentially the same as that obtained when the control spectral width was computed within the analysis program.

Influence of Pulsatility on Spectral Width

Figure 60 presents the centrestream spectral waveforms recorded with the 20 MHz PDUVM at six post-stenotic axial positions for the three pulsilities studied with the cam-based pulsatile unit. Immediately apparent in the figure is the variation in pulsatility as demonstrated by the three different peak-to-peak amplitudes of the undisturbed waveforms far (15 cm) downstream of the stenosis. The constancy of pulse rate is reflected in the closeness of all three cycle periods to 550 msec (approximately 105 BPM). The waveforms at 15 cm downstream are approximately sinusoidal in shape: deviations resulted from the use of

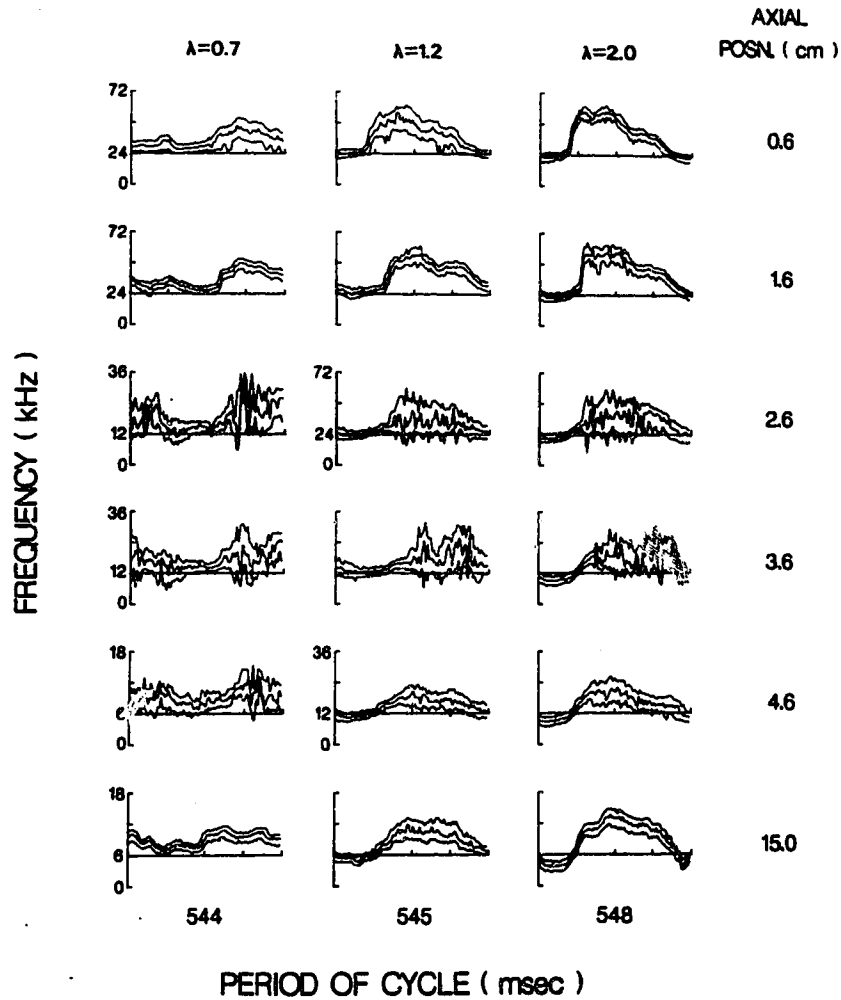


Figure 60. Centrestream spectral waveforms recorded with the 20 MHz PDUVM at six post-stenotic axial positions for the three pulsatilities studied with the cam-based pulsatile unit. The post-stenotic arterial wall was made of rigid acrylic plastic. Pulsatilities are indicated at the top of the figure with the greek letter lambda (λ).

cams of slightly different shape and inaccuracies of the cam follower tracking process. It is also apparent in figure 60 that the undisturbed waveforms at each pulsatility commence at different phases of the pulse cycle. As in the pulse rate experiments this is due to the use of different cams generating sync pulses at different points in the pulse cycle. The pulsatility waveforms, however, are in much closer synchrony than the pulse rate waveforms, presumably because the pulse rate was the same for each cam in the former.

The axial variation of waveforms at all three pulsilities, like the axial variation observed in the pulse rate experiments, shares the previously described features of the pulsatile post stenotic velocity field (see 'Spectral Waveforms and Flow Visualization'). Briefly, at 0.6 and 1.6 cm downstream of the stenosis velocities are considerably elevated, indicating jet flow (the mode frequency for $\lambda = 1.2$ is approximately 24 kHz above the offset frequency (24 kHz) at the pulse peak, as compared to approximately 5 kHz above the offset (6 kHz) at 15 cm downstream). Further downstream (2.6 cm), waveform bursting occurs. The bursting flow disturbance persists at 3.6 cm downstream, is partly dissipated at 4.6 cm downstream, and is fully dissipated at 15 cm downstream. The evidence for complete dissipation of the bursting flow disturbance at 15 cm downstream lies in the narrow width of the spectral

waveforms and their lack of erratic fluctuations.

In order to determine if pulsatility affected post-stenotic turbulence production each spectral waveform of figure 60 was input to the same computer program used to analyze the turbulent bursting properties of the different pulse rate waveforms of figure 56. The calculated mean relative spectral widths (MRELW), relative burst times (RELBT), and time average relative spectral widths (AVRLW) for each pulsatility at each axial location are presented in table 8. From the table it can be seen that mean relative spectral width rises to a peak at 2.6 cm downstream for $\lambda = 1.2$ and at 3.6 cm downstream for $\lambda = 0.7$ and 2.0. After these peaks, MRELW declines with increasing post-stenotic distance. Thus the axial pattern of variation of mean relative spectral width at different pulsilities (and a constant pulse rate of 105 BPM) was similar to that observed at different pulse rates; it was therefore consistent with the post-stenotic axial pattern of centrestream relative spectral width seen under steady flow conditions.

The relative burst time in table 8 shows axial peaking at 2.6 cm downstream for all three pulsilities. Because of the axial peaking of MRELW and RELBT, time average relative spectral width (AVRLW) also shows peaking. Figure 61 illustrates the variation of the latter with post-stenotic axial position for all

PULSATILITY		0.7	1.2	2.0
Axial Posn.				
0.6	MRELW	1.1	0.9	0.0
	RELBT	0.45	0.64	0.0
	AVRLW	0.49	0.57	0.0
1.6	MRELW	0.0	0.4	0.4
	RELBT	0.0	0.10	0.32
	AVRLW	0.0	0.04	0.13
2.6	MRELW	1.6	2.7	1.9
	RELBT	0.73	0.66	0.73
	AVRLW	1.17	1.78	1.38
3.6	MRELW	2.4	2.2	2.1
	RELBT	0.73	0.59	0.60
	AVRLW	1.76	1.29	1.26
4.6	MRELW	1.2	1.6	1.2
	RELBT	0.07	0.54	0.35
	AVRLW	0.08	0.87	0.42
5.6	MRELW	1.7	1.5	0.8
	RELBT	0.48	0.62	0.35
	AVRLW	0.81	0.94	0.28
15.0	MRELW	0.0	0.9	0.0
	RELBT	0.0	0.45	0.0
	AVRLW	0.0	0.40	0.0

Table 8. Mean relative spectral widths (MRELW), relative burst times (RELBT), and time average relative spectral widths (AVRLW) obtained from the bursting analysis of the PDUVM waveforms of figure 60.

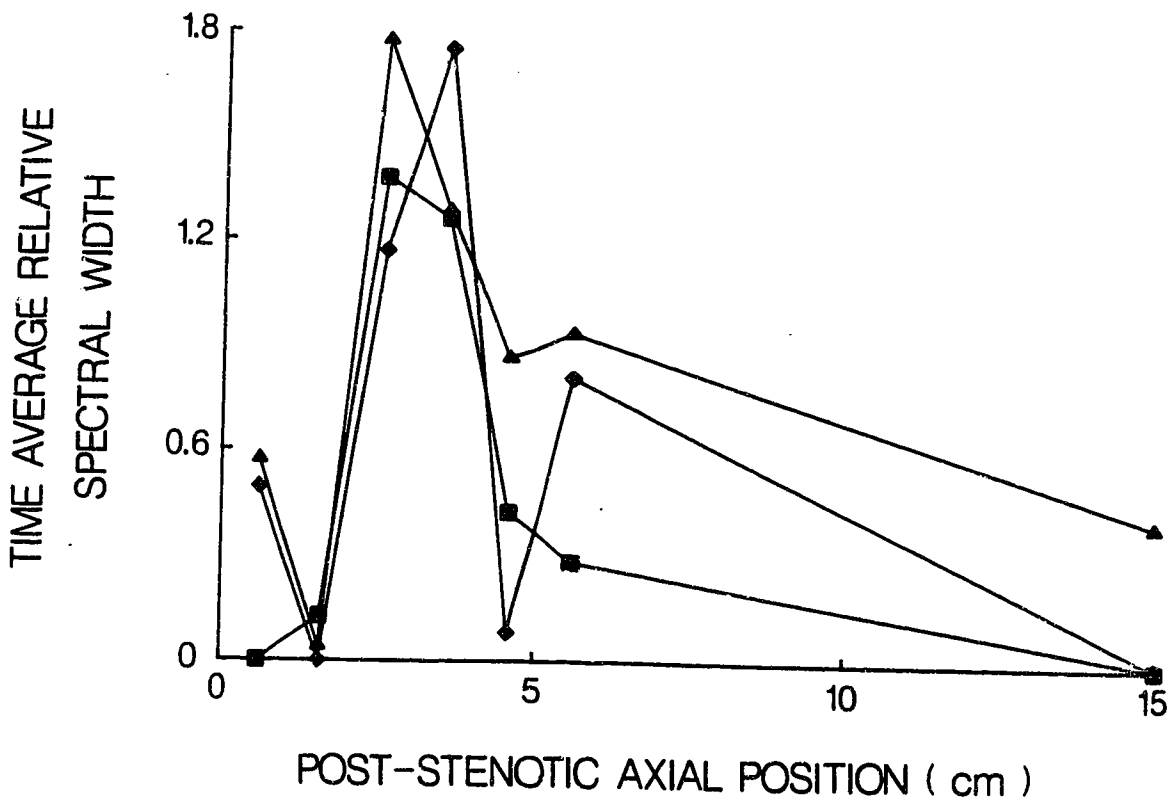


Figure 61. The variation of time average relative spectral width with post-stenotic axial position at three pulsilities. The downstream tubing was rigid acrylic material. Pulsilities are $\lambda = 0.7$ (diamond), $\lambda = 1.2$ (triangle), and $\lambda = 2.0$ (square).

three pulsatilities. This figure demonstrates that time average relative spectral width does not appear to be influenced by pulsatility at any axial position. The additional data of the pulse rate experiment conducted at 105 BPM and a mean pulsatility of 1.8 are consistent with this conclusion.

As was done with the post-stenotic pulse rate waveforms, the pulsatility waveforms were subjected to an additional analysis concerned with flow disturbance over the whole pulse cycle. Specifically, mean relative spectral width over the whole pulse cycle (WCMRW) was calculated for each pulsatility at each axial location. The pattern observed using this parameter was similar to that of the time average relative spectral width in the bursting analysis. Thus whole cycle mean relative spectral width showed axial peaking from 2.6 to 3.6 cm downstream of the stenosis. There was no clear effect of pulsatility on WCMRW at the points of peaking or at any other axial position.

In addition, mean relative spectral width over the burst, relative burst time, and time average relative spectral width over the burst were recalculated with a modified computer program. As for the pulse rate experiment analysis, the modified computer program used equations (8) and (10) and the same 200 percent burst width criterion, but an externally supplied control spectral width. The latter was obtained by hand

measuring the minimum distance between contours at each axial location and pulsatility. The variation of the above three parameters with axial position and pulsatility was mostly the same as that obtained when the control spectral width was computed within the other bursting analysis program.

In Vivo Aortic Branches

Spectral width in the waveforms from all locations was narrow and showed little intra-cycle or inter-location variation. There was no evidence therefore, of turbulent like flow disturbance in the *in vivo* abdominal aorta in the vicinity of the cranial mesenteric and renal arteries.

In Vitro Aortic Branches

Spectral width in the waveforms from most axial locations was narrow and showed little intra-cycle or inter-location variation. However, in the steady flow experiment with maximum renal branch flow spectral width was wider than normal at most locations across the aorta 0.5 cm downstream from the branch. This was the only evidence of turbulent like flow disturbance in the *in vitro* abdominal aorta.

IV. DISCUSSION

A. OPENING REMARKS

The purpose of this thesis was essentially twofold. First and foremost, the purpose was to improve the interpretation of the PDUVM signal originating in disturbed axial velocity fields. This was accomplished by comparing the PDUVM output under a variety of post-stenotic flow conditions with the actual velocity field revealed by flow visualization in an *in vitro* model. The second major purpose was to use the PDUVM to search for potentially atherogenic flow disturbances. This was accomplished by exploring the velocity fields in the vicinity of dog abdominal aortic branches, both *in vivo* and *in vitro*, and noting the conditions under which flow disturbance occurred. In a separate study under the same objective the effect of pulse rate and pulsatility on flow disturbance downstream of an *in vitro* stenosis was determined. In the process of pursuing the two main objectives it became necessary to assess the space resolving power of the PDUVM with respect to the velocity fields charted. Therefore, a third thesis objective was to determine the spatial resolution of the PDUVM's used. Another important question arose: how did the PDUVM velocity output compare with the absolute velocities in the charted velocity fields? Thus, a fourth thesis objective involved assessing the capacity of the PDUVM to measure velocities absolutely. The thesis results will now be discussed in the

context of the four objectives named above, beginning with the most straightforward purpose - determining the PDUVM spatial resolution, and concluding with the most theoretical purpose - investigating the hemodynamic basis of atherosclerosis.

B. PDUVM SPATIAL RESOLUTION

Sample Volumes

The moving string technique (Walker *et al.*, 1982) for measurement of PDUVM sample volume dimensions was chosen here to maximize convenience and minimize cost. Other techniques, such as the underwater jet (Baker and Yates, 1973; Jorgensen *et al.*, 1973), moving magnetic tape (Morris *et al.*, 1973), steel hemisphere point reflector (Knox *et al.*, 1982), and vibrating point reflector (Hoeks *et al.*, 1984) have been used by other workers. There is apparently a lack of consensus as to which technique is the best, although Hoeks *et al.* (1984) argue against the moving string method and favour the use of a vibrating point reflector.

The near field diameter of the ultrasonic beam emerging from an unfocussed PDUVM transducer is primarily determined by the transducer radius (Morris *et al.*, 1973; Zagzebski and Madsen, 1982). The beam is collimated in the near field but diverges from the beam axis in the so-called far field at an angle proportional to the arctangent of the ratio of the ultrasound wavelength to the transducer radius (Morris *et*

al., 1973). Thus, the lower the transmission frequency, or the smaller the transducer radius, the greater the beam divergence in the far field. Since the radius of the 20 MHz transducer was 0.5 mm, and that of the 10 MHz transducer was 1.5 mm, their near field lengths were 3.3 mm and 14.6 mm, respectively (assuming a speed of ultrasound in tissue of 1540 m/sec and using the field length equation quoted in Morris *et al.*, 1973). Using the same data, the calculated divergence angle for the 20 MHz far field is 8.8 degrees. The sample volume diameter measurements on the 20 MHz transducer were made at ranges (2.5 to 7.3 mm) which encompassed both the near and far fields. This was not the case with the 10 MHz transducer, the maximum range being 9.9 mm. Given that the sample volume diameter is essentially the ultrasonic beam diameter at a specified sound intensity, it follows that the above considerations can be used to explain the 20 and 10 MHz transducer sample volume diameters at the various range gate positions.

The variation of the 20 MHz sample volume diameter with range gate position is more easily explained than the 10 MHz variation. Only one (at the range gate position of 2.5 mm) of the 20 MHz sample volume diameter measurements is within the calculated near field so it is not possible to check for beam collimation. However, the remaining diameter measurements show a gradual increase at each successive range gate position, which is consistent with the theoretical prediction of a small divergence angle in the

far field. Furthermore, in laminar flow velocity profile experiments (see also below) the 20 MHz signal decreased in amplitude markedly with range gate positions beyond about five mm. This is also consistent with far field behaviour (Morris *et al.*, 1973). Because the variation in 20 MHz sample volume diameter was small it was concluded that a correction for variation was negligible and unnecessary for the present purposes. Thus the overall mean diameter of 0.69 mm was sufficient to describe the 20 MHz sample volume diameter between range gate positions of 2.5 and 7.3 mm.

The variation of the 10 MHz sample volume diameter with increasing range gate position was opposite in direction to the 20 MHz diameter variation. The observation that there was no divergence of the 10 MHz sample volume diameter between range gate positions of 2.8 and 9.9 mm is consistent with the theoretical prediction of a near field extending to 14.6 mm. In laminar flow experiments (see below) the 10 MHz signal was much stronger than the 20 MHz signal at approximately five mm or more. Thus at this range the 10 MHz signal was strong in the near field while the 20 MHz signal was weak due to far field reduction proportional to the inverse square of the distance from the transducer (Morris *et al.*, 1973). What was surprising was the observed reduction in 10 MHz sample volume diameter within the near field. Apparently some focussing (Zagzebski and Madsen, 1982) of the transducer was occurring which was not mentioned in the manufacturer's manual. Like the variation

of the 20 MHz sample volume diameter the variation of the 10 MHz diameter over the range studied was considered small and therefore not requiring a correction. Thus the 10 MHz overall mean sample volume diameter of 1.09 mm was considered representative of the diameter between range gate positions of 2.8 and 9.9 mm.

The sample volume results, ultrasonic beam geometry calculations, and laminar flow signal strength observations discussed above suggested that the useful range of the 20 MHz PDUVM was limited to five mm along the ultrasonic axis. By contrast, the corresponding considerations suggested that the 10 MHz PDUVM had a useful range of at least 9.9 mm and probably closer to 14.6 mm. Therefore it was decided that the 10 MHz PDUVM should be used for the relatively large diameter (10 mm) aortic velocity measurements which required range gate settings outside the useful limit of the 20 MHz PDUVM. The latter, with its smaller sample volume diameter and thus greater spatial resolution (Morris *et al.*, 1973; Knox *et al.*, 1982) was selected for investigation of the relatively small diameter (six mm) post-stenotic velocity fields.

Laminar Flow Velocity Profiles

At the outset of the laminar flow experiments it was decided to move the sample volume across the 5.4 to 5.5 mm tube diameter in increments of 0.4 mm using the electronic range gate control. This allowed comparison of the spatial

resolution of both velocimeters under real flow conditions when the 20 MHz device was operated outside of its near field and the 10 MHz unit was operated within its near field. Such a comparison would also reveal the respective capacities of these two velocimeters to measure flow velocity absolutely (see 'PDUVM Velocity Output' below). Using the 0.4 mm increment both the 10 and 20 MHz PDUVM's produced distinct increments in flow velocity between most of the sample volume positions. The 20 MHz PDUVM velocity profiles computed from the spectral mode followed more closely the theoretical profiles for laminar flow in the near half of the tube than in the far half. This emphasized the range limitation of the 20 MHz device and restricted its use mainly to a maximum depth of 4.5 to 5.0 mm (centrestream) in the post-stenotic experiments. Spatial information in the post-stenotic velocity field was obtained by moving the sample volume across the tube diameter in the horizontal plane with the range setting fixed.

The 10 MHz PDUVM velocity profiles did not follow the theoretical profiles as closely as the 20 MHz profiles, but they were more consistent across the whole tube. The former observation can be explained on the basis of the larger sample volume size of the 10 MHz device, thus giving it a poorer spatial resolution. The latter observation can be explained on the basis of the already described superiority of the 10 MHz PDUVM signal at range settings beyond five mm. Thus the extended range capability of the 10 MHz device was

emphasized and further directed its application toward the exploration of large diameter aortic velocity fields. Because of the distinct velocity increments produced by both PDUVM's between radial positions separated by 0.4 mm under laminar flow conditions it was concluded that both devices had spatial resolutions of 0.4 mm or better along the ultrasonic axis. From this, a more general conclusion was made: the functional spatial resolution of both PDUVM's was approximately 50 percent of their sample volume dimensions. Accordingly, when spatial increments of 0.5 and 1.0 mm were chosen for the exploration of post-stenotic and aortic velocity fields, respectively, the velocity results obtained were considered to have spatial resolutions well within the capacities of the PDUVM's used.

Comparative Spatial Resolutions

Five MHz PDUVM transducers are often used in clinical practice (Phillips *et al.*, 1983; Ku *et al.*, 1985b). They usually have large diameters, on the order of 10 mm (Baker and Yates, 1973; Knox *et al.*, 1982). Thus it is not surprising that the 5 MHz transducer used by Walker *et al.* (1982) had a much larger sample volume (diameter 3.7 mm, depth 2 mm) than the sample volumes reported here. Therefore the PDUVM's used here have spatial resolutions superior to the typical clinical device. Furthermore, because of their relatively small sample volumes, the PDUVM's used here provide a much better distinction of spectral broadening due

to post-stenotic turbulence from broadening due to jet/separation zone velocity gradients than the typical clinical PDUVM.

C. PDUVM VELOCITY OUTPUT

Having established the spatial resolutions of both PDUVM's, the next question considered was: to what extent can each device measure flow velocity absolutely? The answer was obtained by comparing the velocity profiles measured with both velocimeters under conditions of steady laminar flow with the theoretical profiles for the same flow conditions. There were two essential findings. First, the maximum (centrestream) PDUVM velocity consistently underestimated the theoretical maximum. Second, the tube diameter, as determined by the intercepts of the velocity profile with the zero velocity axis, was always overestimated. This distortion of the true velocity profile has been observed by other PDUVM users (Baker, 1970; Miller *et al.*, 1972; Garbini, 1973; Jorgensen *et al.*, 1973; Jorgensen and Garbini, 1974). The distorted velocity profile is an image formed by the mathematical operation of convolution between the PDUVM sample volume and the true velocity profile (Jorgensen *et al.*, 1973).

Perhaps the most precise statement on the relationship between the PDUVM sample volume and the PDUVM image profile has been made by Garbini (1973). He described the velocity resolution of his PDUVM in terms of the ratio of the sample

volume depth ('PL') to the tube diameter ('D') containing flow. Specifically, he stated that when the PL/D ratio is less than 0.1 the PDUVM velocity profile is 'a fairly good representation of the true profile.' When the PL/D ratio is greater than 0.2 the PDUVM profile becomes 'an increasingly poor approximation.' The minimum PL/D ratios for the PDUVM's used here are 0.125 for the 20 MHz device and 0.169 for the 10 MHz unit (using a tube diameter of 5.5 mm). On the basis of Garbini's guidelines these numbers suggest that the 20 MHz PDUVM velocity profiles should more closely approximate the true laminar flow profile than the 10 MHz PDUVM profiles. This was indeed the case at all four Reynolds numbers studied.

In order to make accurate volume flow or wall shear stress measurements from a PDUVM velocity profile the Doppler profile must represent the actual profile as closely as possible. The best method for correcting the distortion due to convolution is the deconvolution algorithm (Garbini, 1973; Jorgensen and Garbini, 1974). Application of this method to the present results was considered but not pursued due to its complexity. Instead, a simple correction based on the use of the maximum frequency in the PDUVM signal spectrum was performed.

It was reasoned that at centrestream underestimation of the peak velocity will occur when the spectral mode or mean is used in the Doppler equation because neither of these frequencies estimates the highest velocity in the sample

volume. The peak centrestream velocity can be recovered by substituting the spectral maximum eight dB above the mode (the upper contour frequency) or one standard deviation above the mean into the Doppler equation. As illustrated in the results section (figure 19), because of sample volume overlap the use of the spectral maximum results in a similar peak velocity estimate for the centrestream sample volume and the two volumes immediately adjacent to it. Since the space between points in the laminar flow experiments was 0.4 mm and the minimum sample volume depth was 0.69 mm it was obvious that sample volume overlap was occurring both for the 20 and 10 MHz PDUVM's.

It was reasoned that removal of the two centre-adjacent points from a spectral maximum based PDUVM velocity profile would not result in a loss of velocity information. Furthermore, such a manipulation, combined with a shifting of points toward centrestream, would adjust for the PDUVM overestimation of the tube diameter. When this convolution compensation procedure was performed, the improvement in the PDUVM velocity profiles was dramatic for both velocimeters. Such an improvement provides a means for enhancing the accuracy of volume flow measurement by velocity profile integration. Gill (1985) reviews the velocity profile integration technique and comments on its sources of error. The spectral maximum convolution compensation method reported here provides a means of reducing the error caused by the finite spatial resolution of the PDUVM when volume

flow is measured by the velocity profile integration technique. It must be emphasized, however, that the compensation method assumes sample volume overlap. This, in turn, requires a knowledge of sample volume size.

The convolution compensation procedure was not applied to the measurements of post-stenotic and aortic velocity fields since it was not applicable to situations other than steady laminar flow. Furthermore, absolute velocity measurements in these complicated flow situations were not desired. Instead, it was the nature of flow patterns and the sources of PDUVM spectral broadening which were sought after. Pursuit of the same objectives determined that the spectral mode rather than the spectral mean was used in the non-laminar flow velocity calculations and computations of spectral width. Despite the smoother laminar velocity profiles obtained with the spectral mean this parameter tends to mask any asymmetry present in the original PDUVM spectrum (Langlois *et al.*, 1984). The mode does not mask spectral asymmetry and therefore was chosen as the spectral parameter which best represents the Doppler signal.

PDUVM spectral asymmetry is a frequent clinical finding, for example the closing of the systolic window downstream of a high grade stenosis (Blackshear *et al.*, 1980). Three situations in which spectral asymmetry occurs, and the reason for each instance of asymmetry, are as follows. The PDUVM detects all velocity vectors traversing its sample volume. The vectors which deviate the least from

the ultrasonic axis will be recorded as the highest frequencies in the PDUVM spectrum and vice versa. In turbulent flow, which is known to occur downstream of a stenosis, some of the velocity vectors will be oriented along or close to the ultrasonic axis. However, most of the vectors will be randomly oriented away from the PDUVM axis, resulting in a preponderance of low frequencies in the signal spectrum. Thus the PDUVM spectrum will be asymmetric in turbulent flow, with the lower end of the spectrum being broader than the upper end. If the PDUVM sample volume is placed in the shear layer between a post-stenotic jet and the low velocity recirculation zone surrounding it spectral asymmetry may also occur. The part of the sample volume closest to the jet will detect high velocity, unidirectional flow. The part closest to the recirculation zone will detect low velocity flow. The part of the sample volume placed within the centre of the shear layer will detect a wide range of flow velocities. If the sample volume is closer to the jet, i.e. near centrestream, the mode frequency will be situated near the top of the spectrum, and the spectral band between the mode and the bottom of the spectrum will be broader than the band between the mode and the top of the spectrum. This would also result in closing of the systolic window and is a likely cause of this effect in the clinical situation since diagnosis is made with centrally placed sample volumes. By contrast, if the sample volume is closer to the recirculation zone, the PDUVM spectrum will be

asymmetric in the opposite direction. In particular, the mode frequency will be near the bottom of the spectrum and the spectral band between the mode and the top of the spectrum will be broader than the band between the mode and the bottom frequency.

D. PDUVM RECOGNITION OF POST-STENOTIC FLOW REGIMES

A Clinical Question

The previous discussion of the PDUVM velocity output in laminar flow may be of limited interest to the clinician who more frequently encounters disturbed flow downstream of arterial stenosis. A reasonable question for such an individual to ask is: what useful information does the PDUVM provide when its sample volume is placed in the post-stenotic velocity field? The results which presented a comparison of the PDUVM output with the actual post-stenotic velocity fields revealed by flow visualization provide an answer to this question. The essential answer is that three different types of post-stenotic flow regimes are readily identifiable with the PDUVM: jet flow, separated flow, and turbulent flow.

Jet and Separated Flow

Both the steady and pulsatile flow experiments pointed out the types of flow regimes identifiable with the PDUVM immediately downstream of stenoses. In steady flow

immediately downstream of stenoses a comparison of PDUVM velocity profiles and particle displacement vectors showed that the PDUVM was capable of detecting separated flow and jet flow. Short vectors located near the post-stenotic walls and which corresponded in direction with the the near wall components of the PDUVM velocity profile showed that flow separation was detectable. Long, forward-directed vectors located near centrestream indicated that the PDUVM was indeed recording jet flow at that location. Two different types of flow separation were identified, one with forward flow and one with reverse flow. As mentioned in the results section the former flow regime, which corresponded to a low forward shoulder on the PDUVM velocity profile, may be due to a complicated helical flow which turns back on itself after the initial separation and reversal. The cause of such a complicated flow may be asymmetry in the stenosis geometry, since such geometric factors are known to induce asymmetric velocity profiles (Lesvesque *et al.*, 1986). The reverse flow regime is typically expected in a separated flow downstream of a stenosis (Ahmed and Giddens, 1983a).

Steady flow visualization velocity vectors were computed from the displacement vectors by division by the time lapse over which displacement occurred. The magnitudes of the flow visualization and PDUVM velocity vectors for the jet and separation flow regimes taken from nine post-stenotic experiments were correlated and their directional correspondence checked. There was a significant

correlation for the jet regime but not for either of the separation regimes. This is probably because the jet flow was one dimensional and therefore accurately recordable with a single axis PDUVM. On the other hand, the separation flows were two or three dimensional and would therefore require multiple ultrasonic axes for accurate recording. Nevertheless there was 100 percent directional correspondence between all PDUVM and flow visualization vectors in both jet and separation flow regimes.

In pulsatile flow immediately downstream of stenoses results similar to those obtained in steady flow were achieved. Specifically, the high velocity, centrestream portions of the post-stenotic velocity profiles corresponded well with visualized long, straight particle streaks emerging from the stenoses. Thus PDUVM detection of jet flow was validated. The near wall, low velocity forward and reverse shoulders of the post-stenotic velocity profiles corresponded with visualized zones of spherical particles on either side of the visualized jet. The spherical shape of these flow visualization particles indicated low velocity, separated flow was being detected by the PDUVM. An additional result was obtained due to the time variation of the flow. There was a cyclic change in the streak length of the jet particles emerging from the stenoses. Early in the pulse cycle the streak lengths were relatively short, during pulse acceleration the lengths were increased, and at the pulse peak the lengths were at a maximum. Then, during pulse

deceleration the streak lengths decreased toward the lengths present at the start of the pulse cycle. The cyclic change in visualized streak length corresponded well with the pulsatile variation in PDUVM mode frequency and therefore velocity. Thus the PDUVM capacity to detect pulsatile jet flow was validated. The detection of pulsatile jet flow above 120 cm/sec ($Fd = 4$ kHz at 60 degrees, 5 MHz transducer) is an important diagnostic criterion for arterial disease (Fell *et al.*, 1981).

The detection of separated flow is important clinically since Ku *et al.* (1985b) have demonstrated that separation in the carotid bulb is a normal finding, not an indication of disease. Thus a healthy carotid bulb can be identified by a PDUVM flow separation signal along the bulb lateral wall. The carotid bulb separation demonstrated by Ku *et al.* (1985b) was manifested by reverse flow. The results presented here point out that a low, forward-directed shoulder on a PDUVM velocity profile is also suggestive of flow separation. Furthermore, whereas the present results showed by a direct method that the PDUVM can identify flow separation zones Ku *et al.* (1985b) obtained similar results by an indirect comparison of PDUVM flow signals *in vivo* with LDA flow signals *in vitro*.

Reasons for Variation in PDUVM Spectral Width

Jet Sources of Variation

The juxtaposition of jet and separated flows downstream of a stenosis has important effects on the ultrasonic spectral width detected. Briefly, the PDUVM spectral width will depend on the position of the sample volume relative to the separation zones. If the sample volume is placed within a separation zone then the spectral width will be narrow due to the small velocity gradients present. If the sample volume is placed within the jet then the spectral width will be broader due to the higher velocity gradients present. PDUVM spectral width will be broadest when the sample volume is placed in the shear layer between jet and separation zones since this is a situation where the velocity gradient within the sample volume is at a maximum.

The bimodal variation (figures 47 and 48) of spectral width with the sample volume positioned 0.6 cm (1 diameter) downstream of the 0.19 cm (90 percent) stenosis can be explained by the above arguments. The spectra obtained with the sample volume placed in the visualized (figure 46) separation zones (e.g. radial positions 1 to 4 and 9 to 11 in figure 47) were relatively narrow due to the small velocity gradients present. Because of the high velocities present in the more centrally situated jet the corresponding PDUVM spectra were relatively wide (radial positions 6 and 7, figure 47). With the sample volume centred on the

so-called 'shear-layer' between the jet and zones of separation (radial positions 5 and 8, figure 47) high velocities from the jet and low velocities from the separated flow were included in the the volume insonated. This increased the velocity gradient present in the sample volume at those positions and produced the greatest spectral widths across the radius at this axial location.

Forster (1977) has suggested that spectral width can be used as an index of turbulence and Hutchison and Karpinski (1985) have shown a close correlation between maximum centrestream spectral width downstream of stenoses *in vivo* with stenosis grade. The expected centrestream axial flow characteristics downstream of a stenosis are described by Young (1979). The post-stenotic jet eventually breaks up and high energy turbulent flow results. Even further downstream the turbulence decreases until the flow pattern upstream of the stenosis is re-established. These results are consistent with the observations illustrated in figure 49 and table 6. Immediately downstream of the 0.19 cm (90 percent) stenosis at the highest flow rate the centrestream relative spectral width was 167 percent wider than the width at the furthest downstream location. Relative spectral width increased to a maximum of 1.51 at the 4.3 diameters downstream location, then decreased to a minimum of 0.24 at 12.7 diameters down. A

similar axial variation of spectral width was observed with this stenosis and lower Reynolds numbers and with the 0.29 cm (77 percent) stenosis and two higher Reynolds numbers. The pattern of spectral width is somewhat different downstream of a stenosis when continuous wave Doppler velocimetry is used. Maximum spectral width is found immediately downstream of the stenosis (Morin *et al.*, 1988). This is in the region of the jet and flow separation rather than at the point of jet break up. With the continuous wave technique most of the artery is insonated and does not allow separation of the spectral width increases due to the high velocity gradient such as occurs between the jet and separation region from that due to turbulent flow at jet break up.

The fact that maximum spectral width, using continuous wave technology, is found in the location of jet and flow separation suggests that the increased velocity gradient in such regions is a more potent cause of spectral broadening than the turbulence of jet break up. The diagnosis of moderate stenosis using pulsed Doppler techniques is based on midline spectral broadening without an increase in peak velocity (Strandness, 1986). This situation is best modelled in these experiments with the 0.4 cm (56 percent) stenosis at the highest Reynolds number and the 0.29 cm (77 percent) stenosis at the lowest Reynolds number. In these two examples centrestream spectral broadening

remained low to 6 diameters downstream. Maximum midline spectral width, indicating jet break up, thus occurred relatively far downstream. Flow visualization showed that there were narrow zones of flow separation up to the point of spectral broadening. Jet break up then produced turbulent flow which persisted as far distally as observations were made. This leads to the speculation that minimal degrees of spectral broadening used to diagnose the low grades of stenosis at the carotid bifurcation using pulsed Doppler ultrasound may often be due to insonation of a shear layer between the jet and separation regions rather than due to the turbulence of jet break up which will be present further downstream. Many of the lesser grades are due to asymmetric plaques, so that the choice of the geometric midline may not be the hemodynamic centrestream and may be in the shear layer between jet and recirculation zones. The pattern of the position of maximum midline spectral width demonstrated in table 6, namely, that the distance downstream from the stenosis of jet break up varies inversely with Reynolds number and stenosis grade, is in agreement with other work (Yongchareon and Young, 1979; Ahmed and Giddens, 1983b). It is related to the longer lower velocity jets associated with lower Reynolds number and lower stenosis grade.

Other Sources of Variation

The increase in spectral width across centre line in the laminar flow model (figure 45) appears to be due to a decrease in signal to noise ratio in the 20 MHz PDUVM at ranges exceeding half the manufacturer's rated maximum. This makes sense in light of the earlier statement that the 20 MHz PDUVM near field ends at a range of 3.3 mm, beyond which the signal strength decreases very rapidly (see 'PDUVM Spatial Resolution: Sample Volumes' above). An apparent effect of amplifier gain is due to amplification of this effect. As noted above, the experiments with the post-stenotic model used the 20 MHz PDUVM at a range of 4.5 mm to avoid this effect.

Increase in spectral width with increasing Reynolds number (figure 50) is principally due to the transit time of scatterers through the sample volume (Newhouse *et al.*, 1980; Garbini *et al.*, 1982). There is also a contribution from an increasing velocity gradient within the sample volume (Baker *et al.*, 1978). Using the relevant velocity profiles and measured sample volume diameter the contribution of velocity gradient in the 20 MHz sample volume was estimated at 10 percent of the total spectral width. Figure 50 suggests that the velocity effect is relatively small in relation to the effect of stenosis grade when flow or Reynolds number changes by a magnitude of two. This is similar to the

conclusion of an *in vivo* study in dogs (Hutchison and Karpinski, 1988). Thus reproducibility will be little affected by flow variation in patients in whom measurements are made under basal resting conditions. This will be particularly true for extracranial carotid examinations because of the stability of cerebral blood flow due to autoregulation. It will, however, tend to reduce resolution between different diagnostic grades.

In conclusion, the spectral width results discussed above are in agreement with those of *in vivo* experiments which suggest that stenosis grade can be distinguished using maximum centrestream spectral width (Thiele *et al.*, 1983; Hutchison and Karpinski, 1985). However, the conditions of these measurements should be re-emphasized. The recordings were made with a constant sample volume range and a hemodynamic centrestream sample volume position. This means that sample volume size was kept constant and the shear layer between jet and flow separation was avoided. The effect of variation in volume flow is small compared to the effect of stenosis grade in the range likely to be encountered under basal conditions. The accurate estimation of stenosis grade from spectral width requires compensation for such variables.

Jet Breakup in Pulsatile Flow

The overall axial pattern of pulsatile flow regimes was very similar to that seen in steady flow. Immediately downstream of the stenosis there was a centrestream jet accompanied by peripheral regions of flow separation. Flow visualization verified that the jet velocity varied with the time in the pulse cycle. Further downstream the jet broke up into turbulent type flow. The turbulence diminished with increasing distance from the stenosis until laminar flow was reestablished. Turbulent jet break up occurred mainly during the period of pulse deceleration and was characterized by a sudden expansion in the PDUVM spectral width which was termed 'bursting.' The timing of the jet break up results reported here is consistent with that obtained by others, i.e. the flow disturbance occurred during pulse deceleration (Cassanova and Giddens, 1978; Khalifa and Giddens, 1981; Giddens and Khalifa, 1982; Talukder *et al.*, 1986). As was observed in steady flow the post-stenotic pulsatile spectral width peaked at the site of jet break up determined by flow visualization.

E. THE HEMODYNAMIC BASIS OF ATHEROSCLEROSIS

Wall Shear Stress

As was outlined in the introduction, several hemodynamic theories of atherogenesis are based on the exposure of arteries to abnormal levels of wall shear

stress. In order to test these theories it is necessary to measure wall shear stress in arteries undergoing atherogenic change. The PDUVM would appear to be the most suitable device for such an investigation because of its non-invasive nature. However, its spatial resolution has been questioned (Ku *et al.*, 1985a). In a series of steady laminar flow experiments the feasibility of wall shear stress measurement using the 10 and 20 MHz PDUVM was assessed.

The results are not reported in detail because of their tangency to the main results of this thesis. Initially, a linear regression of seven to eight near wall velocity points was used to obtain the velocity gradient. These points were all close to the wall, the increments being 0.1 mm for the 20 MHz PDUVM and 0.2 mm for the 10 MHz PDUVM. The PDUVM wall shear stress was then calculated by multiplying the wall velocity gradient by the previously measured fluid viscosity. This wall shear stress deviated from the theoretical shear by 31 to 46 percent for the 20 MHz velocimeter and 50 to 70 percent for the 10 MHz device. The best results were obtained when a complete 15 point (0.4 mm between points) velocity profile was fitted to a second order curve (3.7 to 7.5 percent deviation from the theoretical for the 20 MHz PDUVM, 4.8 to 11.4 percent deviation for the 10 MHz PDUVM) and the velocity gradient determined by differentiation. Thus it was concluded that it is possible to measure wall shear stress with the PDUVM in steady laminar flow.

In theory, there is the possibility of extending this successful method to the measurement of wall shear stress in disturbed or recirculating flow. It would require fitting the PDUVM-measured points to an appropriately shaped curve and differentiating the curve to obtain the velocity gradient at the wall. Such a method would obviously be much more labourious than fitting a few near wall points to a straight line as has been done with the laser Doppler anemometer *in vitro* (Bharadvaj *et al.*, 1982a). Nevertheless, the possibility that highly accurate wall shear stress measurements can be made with the PDUVM, especially after deconvolution of velocity profiles, cannot be discounted.

In the context of the hemodynamic theory of atherogenesis two major investigative approaches were taken. First, the relationship between pulse rate, pulsatility and arterial flow disturbance was investigated *in vitro*. The results of this investigation would allow indirect inferences to be made concerning the influence of these two important circulatory parameters on the possible atherogenic effects of flow disturbance. Flow disturbance was generated by the convenient means of a stenosis. In the second approach, the velocity fields in the vicinity of dog abdominal aortic branches were explored *in vivo* and *in vitro*. This would reveal whether or not flow disturbances were present at this frequent site of atherosclerosis.

Pulsatile Post-Stenotic Flow

Nerem and Seed (1972) and Nerem *et al.* (1972) in experiments in the dog aorta and D'Luna *et al.* (1982) in experiments downstream of *in vitro* stenoses found that arterial flow disturbance decreases with increasing pulse rate. Their conclusion is at variance with that of Yellin (1966), who found that increasing pulse rate increased turbulent flow disturbance in constant area rigid tubes. The conclusion of Hale *et al.* (1955) from work in the dog femoral artery would appear to agree with that of Yellin. The conclusion of the pulse rate experiments reported here was that flow disturbance decreased with increasing pulse rate. This was based on the finding that at the post-stenotic axial site where time average relative spectral width reached a maximum, this spectral width decreased with increasing pulse rate. Thus the conclusion reached here supports that of Nerem and Seed (1972), Nerem *et al.* (1972), and D'Luna *et al.* (1982). If such a position is correct then under exercise conditions when pulse rate and Reynolds number are increased the increased pulse rate might suppress the development of flow disturbances that would normally develop due to the increased Reynolds number.

Yellin (1966) found that increasing pulsatility decreased flow disturbance production. It should be noted, however, that the pulsilities studied by Yellin were quite low and lower than the minimum studied here. The conclusion of Yellin is perhaps the opposite to what one might expect.

A logical expectation would be that increasing the pulsatility would increase acceleration energy input to a given waveform. Assuming conditions were such that some flow disturbance was occurring, the greater the energy input the greater the expected output in the deceleration phase. Consequently the observed turbulent energy dissipation would be expected to be more intense at elevated pulsilities. Nerem and Seed (1972) mentioned pulsatility as being 'of interest' with respect to flow disturbance development but did not study it. Indeed, there appears to be no evidence in the literature to support the position of Yellin or the expected influence of pulsatility on flow disturbance as described above. The conclusion of the pulsatility experiments reported here was that, over the range studied, pulsatility did not influence the magnitude of time average relative spectral width. Therefore, no effect of pulsatility on flow disturbance was apparent.

Branched Aortic Flow In Vivo

The velocity contours in the dog aorta immediately downstream of the origin of the cranial mesenteric and renal arteries show a zone of reverse velocities during the post-systolic minimum of the pulse cycle. These reverse velocities occur opposite the branch and indicate transient recirculation. There was no evidence of recirculation during the peak systolic part of the cycle such as is found *in vivo* downstream of an arterial stenosis. This feature of the

post-stenotic velocity field has been previously demonstrated (Greene and Hestand, 1979; Hutchison and Karpinski, 1985) and is further illustrated by the results presented in figure 32 for comparison with the velocity fields downstream of the aortic branches. Recirculation zones have been described in steady flow model experiments in the parent vessel opposite branches (El Masry *et al.*, 1978; Karino *et al.*, 1979; Houle and Roach, 1981). Lutz *et al.* (1983) also demonstrated such zones of recirculation with steady flow in their double branching model. Persistent recirculation was not present, however, in their model of the canine celiac and cranial mesenteric arteries, when pulsatile flow was used. Instead, a transient velocity reversal occurred during the post-systolic phase of the cycle in the main vessel opposite the origin of the branches, similar to that found in these *in vivo* experiments. At peak systole they also described asymmetric velocity profiles without recirculation, similar to that occurring along the diameter from the branch origin in the present experiments. Aortic flow, Reynolds numbers, and flow distribution to the mesenteric artery in the present experiments were in the ranges used in their model experiments. The results reported here therefore support the caution of Lutz *et al.* (1983) against the applicability of results from steady flow model systems to *in vivo* arterial systems.

While the results of the experiments at the left renal artery supported the findings at the mesenteric branch two individual experiments are worthy of note. In one the renal arteries arose at the same axial position and in the other there was marked axial separation of the origin of the right and left renal arteries. A comparison of the results of these two experiments illustrates how individual variation in the site of arterial origins can affect velocity patterns. In the aorta in which the renal arteries arose at the same axial position there was no asymmetry of the velocity field and no suggestion of recirculation at any point in the cycle below the origin of the two arteries. Conversely, in the aorta with wide separation of the two renal arteries there was a transient zone of recirculation on opposite sides of the aorta below each of the arteries. Midway between the two arteries the velocity field was symmetrical but in the post-systolic phase of the cycle there was transient recirculation distributed around the circumference of the aorta. This would suggest that while models based on average anatomy (Zarins *et al.*, 1983; Ku *et al.*, 1985a) are useful, it is important to explore the range of geometry encountered *in vivo*.

While these experiments suggest a marked variation between the *in vivo* pulsatile situation and the steady flow model experiments of similar geometries there is evidence that the differences are not so dramatic at other sites. Ku *et al.*, (1985a) have shown that the recirculation zone

demonstrated at the outer wall of the carotid bifurcation in a model using steady flow (Zarins *et al.*, 1983) persists in the presence of pulsatile flow. The size of the recirculation zone does, however, fluctuate during each pulse cycle resulting in exposure of one area of the wall to marked oscillatory shear, a situation which was not of course indicated by the steady flow experiments. Similar persistence of a recirculation area with variation in size during the pulse cycle has been reported in glass models of symmetrical bifurcations (Malcolm and Roach, 1979). Evidence of recirculation at the normal human carotid bifurcation has also been reported (Phillips *et al.*, 1983).

These experiments also suggest that blood flow in the abdominal aorta of the anaesthetized dog is relatively stable and not subject to turbulent type flow disturbances. The narrow spectral width of the Doppler signal found in all the experiments reported here suggests that turbulence or transition to turbulence is not present at this site. This is at variance with the suggestion of turbulence in the rabbit abdominal aorta by McDonald (1952). In a number of midline Doppler velocity waveform recordings in the abdominal aorta of rabbits and cats Hutchison and Karpinski (personal communication) found that spectral widths are very narrow which suggests that blood flow is undisturbed at this location in these smaller animals (unpublished observations). Nerem and Seed (1972) have reported evidence of turbulence in the dog ascending and descending thoracic

aorta but only in occasional animals where peak Reynolds numbers were considerably in excess of those found in the present experiments in the abdominal aorta.

Branched Aortic Flow *In Vitro*

The cast-derived *in vitro* branch model provided an opportunity to study branched aortic velocity fields with different flow conditions but the exact same geometry as occurred *in vivo*.

The steady flow experiments furnished a number of useful conclusions with respect to abdominal aortic flow in the vicinity of the right renal branch. First of all it is clear that the aortic velocity field is strongly influenced by the presence and amount of renal branch flow. Thus in the absence of renal branch flow the aortic velocity contours were symmetric and all forward in direction. With increasing renal flow the forward contours skewed toward the branch ostium and zones of reverse flow appeared. The latter were situated opposite the branch opening as has been demonstrated in other steady flow experiments (El Masry *et al.*, 1978; Karino *et al.*, 1979; Houle and Roach, 1981). At the two highest renal flows there were paired zones of reverse velocity opposite the branch ostium; each member of the pair lying on either side of the aortic diameter in the plane of the branch. A similar observation was made by Karino *et al.* (1979) and Karino and Goldsmith (1985) in their *in vitro* steady flow experiments. They called their

reverse flow zones "paired vortices." The increased spectral widths and erratic waveforms seen in the aortic velocity field with the maximum (56 percent) renal branch flow are suggestive of turbulent flow. However, it is unlikely that turbulence due to this factor would occur *in vivo* since a 56 percent renal branch flow is probably not within the physiologic range. Moreover, as described below, a similar flow disturbance did not develop at the maximum renal branch flow under more physiological conditions of pulsatile flow.

The pulsatile *in vitro* branch experiments extended the results of the *in vivo* branch experiments to a broader range of branch flows. As observed *in vivo*, the *in vitro* aortic velocity contours recorded near peak systole (200 msec after the triggering sync pulse) showed no sign of reverse flow at any of the branch flow rates. The same contours, when there was a finite branch flow, exhibited asymmetry similar to that seen *in vivo* at peak systole. Reverse velocities were present in the post-systolic phase of the pulse cycle and occupied large regions within the aortic cross-section. The paired vortex pattern seen in the steady flow experiments was also apparent in the *in vitro* pulsatile flow velocity contours. Sometimes the paired vortex pattern was revealed in isolated contours on either side of the aortic diameter in the plane of the renal branch. Usually, however, there were no isolated reverse velocity contours. Instead, the paired vortex was made manifest in reverse velocity peaks on either side of the aortic diameter in the plane of the renal

branch. In contrast to the steady flow experiments there was no evidence of turbulence at the maximum branch flow. It is possible therefore that pulsatile flow suppresses turbulent type flow disturbances.

The abdominal aorta is a frequent site of atherosclerosis and many investigators have postulated that flow disturbances may influence or even initiate the development of atherosclerotic disease. The results presented here show that transient paired vortices similar to those observed by Karino *et al.* (1979) and Karino and Goldsmith (1985) occur just distal to canine abdominal aortic branches. This may give rise to alternating shear stress similar to that linked with atherogenesis at the human carotid bifurcation (Ku *et al.*, 1985a).

Abdominal aortic aneurysm is another frequent clinical problem which might be related to hemodynamic disturbances. The mechanism could be similar to that which generates post stenotic dilatation (Roach, 1979). Downstream of a stenosis turbulence resulting from jet breakup is thought to vibrate the arterial wall at frequencies which initiate structural fatigue. Thus the weakened post-stenotic wall begins to dilate. In the same way low frequency vibrations originating in the paired vortex demonstrated in the *visu* abdominal aortic branches could cause structural fatigue in the aortic wall which might lead to aneurysm.

V. CONCLUSION

This thesis was mainly concerned with improving the interpretation of the PDUVM signal in disturbed flow and with acquiring fresh evidence in support of the possible relationship between hemodynamics and atherosclerosis. In order to pursue these objectives steady and pulsatile *in vitro* post-stenotic velocity fields were explored with a 20 MHz PDUVM and branched *in vivo* and *in vitro* aortic velocity fields were explored with a 10 MHz PDUVM. To render reporting of the results of these explorations more rigorous the spatial and velocity resolutions of the two PDUVM's were investigated. In particular, the sample volumes of both PDUVM's were measured and the accuracy of velocity profiles measured with both devices was tested under conditions of steady laminar flow *in vitro*.

With respect to interpretation of the PDUVM signal, it was shown by flow visualization of steady and pulsatile post-stenotic flow that the PDUVM can detect jet, separated and turbulent flow regimes. Furthermore, in steady poststenotic flow four sources of PDUVM spectral broadening were demonstrated: placement of the sample volume in the shear layer between jet and separation zones; turbulence due to jet breakup; transit time of scatterers through the sample volume; and use of the PDUVM at the extremes of its range. The first two sources are expected to arise *in vivo* from pathological arterial stenosis. The third source is expected to result *in vivo* from physiological flow changes.

The fourth source is purely an instrument effect.

With respect to the possible relationship between hemodynamics and atherosclerosis, it was found that increasing pulse rate decreases PDUVM spectral width but pulsatility does not affect spectral width. Since changes in PDUVM spectral width can be interpreted as alterations in the level of flow disturbance it would appear that increasing pulse rate decreases flow disturbance. If flow disturbance is involved in atherogenesis then this result would suggest that increasing pulse rate would have an inhibitory effect on the disease process.

Also with respect to the possible relationship between hemodynamics and atherosclerosis, transient *in vivo* flow recirculation was observed in the post-systolic phase of the pulse cycle at the abdominal aortic wall opposite the branch artery. There was no recirculation at the systolic peak but there was asymmetry of the velocity contour. In a cast-derived, geometrically exact *in vitro* abdominal aortic model in steady and pulsatile flow paired recirculation zones (vortices) were detected along the aortic wall opposite the branch at moderate to high branch flow rates. These results offer an explanation as to why atherosclerotic disease tends to be localized near the branches of the abdominal aorta.

With respect to determining the limitations of the PDUVM method, measurement of the 20 MHz PDUVM sample volume dimensions and laminar flow velocity profiles confirmed that

its spatial resolution was well within the 0.5 mm increments used in the post-stenotic experiments. Similarly the 10 MHz sample volume and laminar flow velocity profile measurements confirmed that the 1.0 mm increments used in the branched aorta experiments did not exceed the spatial resolution of this device. The laminar flow velocity profiles measured with both PDUVM's were distorted in comparison to the expected theoretical profiles due to the convolution of the sample volumes with the actual velocity fields. A compensation for convolution restricted to laminar velocity profiles was developed, rendering these sufficiently accurate to be integrated. Such integration would allow the PDUVM to be used for the measurement of volume blood flow.

The overall conclusion is that the PDUVM can be used to accurately map arterial velocity fields. It is therefore a highly useful instrument in the diagnosis of arterial disease, in the testing of hemodynamic theories of atherogenesis and has the potential to measure volume blood flow.

BIBLIOGRAPHY

- Aaslid, R. (1986) The Doppler Principle Applied to Measurement of Blood Flow Velocity in Cerebral Arteries. In: Transcranial Doppler Sonography, Ed. R. Aaslid. Springer-Verlag, pp.22 - 38.
- Aaslid, R., and Lindegaard, K.F. (1986) Cerebral Hemodynamics. In: Transcranial Doppler Sonography, Ed. R. Aaslid. Springer-Verlag, pp. 60 - 85.
- Ahmed, S.A., and Giddens, D.P. (1983a) Velocity measurements in steady flow through axisymmetric stenoses at moderate Reynolds numbers. J. Biomech., 16: 505 - 516.
- Ahmed, S.A., and Giddens, D.P. (1983b) Flow disturbance measurements through a constricted tube at moderate Reynolds numbers. J. Biomech., 16: 955 - 963.
- Altobelli, S.A., and Nerem, R.M. (1985) An experimental study of coronary artery fluid mechanics. Trans. ASME. J. Biomech. Eng., 107: 16 - 23.
- Angelsen, B.A.J., and Brubakk, A.O. (1976) Transcutaneous measurement of blood flow velocity in the human aorta. Cardiovasc. Res., 10: 368 - 379.
- Azuma, T., and Fukushima, T. (1976) Flow patterns in stenotic blood vessel models. Biorheology, 13: 337 - 355.
- Baker, D. W. (1970) Pulsed Ultrasonic Doppler Blood-Flow Sensing. IEEE Trans. Sonics and Ultrasonics, SU-17: 170 - 185.
- Baker, D.W., and Yates, W.G. (1973) Technique for studying the sample volume of ultrasonic Doppler devices. Med. Biol. Eng., 11: 766 - 770.
- Baker, D. W., Forster, F. K., and Daigle, R. E. (1978) Doppler Principles and Techniques. In: Ultrasound: Its Applications in Medicine and Biology, Part 1. Ed. F. J. Fry Elsevier, pp. 161 - 287.

- Baker, D.W., Johnson, S.L., and Strandness, D.E. (1974) Prospects for quantitation of transcutaneous pulsed Doppler techniques in cardiology and peripheral vascular disease. In: Cardiovascular Applications of Ultrasound, Ed. Reneman, R.S., North-Holland. pp. 108 - 124.
- Barber, F.E., Baker, D.W., Nation, A.W.C., Strandness, D.E., and Reid, J.M. (1974) Ultrasonic duplex echo-Doppler scanner. IEEE Trans. Biomed. Eng., BME-21: 109 - 113.
- Barnes, R.W., and Garrett, W.V. (1978) Intraoperative assessment of arterial reconstruction by Doppler ultrasound. Surg. Gynecol. Obstet., 146: 896 - 900.
- Bascom, P.A.J., Cobbold, R.S.C., and Roelofs, B.H.M. (1986) Influence of spectral broadening on continuous wave Doppler ultrasound spectra: A geometric approach. Ultrasound Med. Biol., 12: 387 - 395.
- Beach, K. W., and Phillips, D. J. (1984) Doppler Instrumentation for the Evaluation of Arterial and Venous Disease. In: Vascular and Doppler Ultrasound, Ed. C. C. Jaffe, Churchill Livingstone, pp. 11 - 49.
- Berguer, R., and Hwang, N.H.C. (1974) Critical arterial stenosis: a theoretical and experimental solution. Ann. Surg., 180: 39 - 50.
- Berne, R.M., and Levy, M.N. (1981) Cardiovascular Physiology, fourth edition. The C.V. Mosby Co., Toronto.
- Bharadvaj, B.K., Mabon, R.F., and Giddens, D.P. (1982a) Steady Flow in a Model of the Human Carotid Bifurcation, Part II - Laser Doppler Anemometer Measurements. J. Biomech., 15: 363 - 378.
- Bharadvaj, B.K., Mabon, R.F., and Giddens, D.P. (1982b) Steady Flow in a Model of the Human Carotid Bifurcation, Part I - Flow Visualization. J. Biomech., 15: 349 - 362.

- Blackshear, W.M., Phillips, D.J., Thiele, B.L., Hirsch, J.H., Chikos, P.M., Marinelli, M.R., Ward, K.J., and Strandness, D.E. (1979) Detection of carotid occlusive disease by ultrasonic imaging and pulsed Doppler spectrum analysis. Surgery, 86: 698 - 706.
- Blackshear, W.M., Phillips, D.J., Chikos, P.M., Harley, J.D., Thiele, B.L., and Strandness, D.E. (1980) Carotid artery velocity patterns in normal and stenotic vessels. Stroke, 11: 67 - 71.
- Brech, R., and Bellhouse, B.J. (1973) Flow in branching vessels. Cardiovasc. Res., 7: 593 - 600.
- Brown, P.M., Johnston, K.W., Kassam, M., and Cobbold, R.S.C. (1982) A critical study of ultrasound Doppler spectral analysis for detecting carotid disease. Ultrasound Med. Biol., 8: 515 - 523.
- Caro, C.G., Fitz-Gerald, J.M., and Schroter, R.C. (1971). Atheroma and Arterial Wall Shear: Observation, Correlation, and Proposal of a Shear Dependent Mass Transfer Mechanism for Atherogenesis. Proc. R. Soc. Lond. (Biol.), 117: 109 - 159.
- Cassanova, R.A., and Giddens, D.P. (1978) Disorder distal to modeled stenoses in steady and pulsatile flow. J. Biomech., 11: 441 - 453.
- Casty, M., and Giddens, D. P. (1984) 25+1 Channel Pulsed Doppler Velocity Meter for Quantitative Flow Measurements and Turbulence Analysis. Ultrasound Med. Biol., 10: 161 - 172.
- Chapman, B.L.W., and Charlesworth, D. (1983) An Analysis of Ultrasound Velocity Waveforms In the Wake of a Stenosis. Vascular Diagnosis and Therapy, 14: 45 - 52.
- Clark, C. (1976a) The fluid mechanics of aortic stenosis - I. Theory and steady flow experiments. J. Biomech., 9: 521 - 528.

- Clark, C. (1976b) The fluid mechanics of aortic stenosis - II. Unsteady flow experiments. J. Biomech., 9: 567 - 573.
- Clark, C. (1976c) Turbulent velocity measurements in a model of aortic stenosis. J. Biomech., 9: 677 - 687.
- Clark, C. (1980) The propagation of turbulence produced by a stenosis. J. Biomech., 13: 591 - 604.
- Clark, C., and Schultz, D.L. (1973) Velocity distribution in aortic flow. Cardiovasc. Res., 7: 601 - 613.
- Clayton, B.R., and Massey, B.S. (1967) Flow visualization in water: a review of techniques. J. Sci. Instrum., 44: 2 - 11.
- Cornhill, J.F. (1983). Quantitative Arterial Wall Morphology. In: Fluid Dynamics as a Localizing Factor for Atherosclerosis, Eds. Schettler, G., Nerem, R.M., Schmid-Schonbein, H., Morl, H. and Diehm, C. Springer - Verlag, pp. 216 - 226.
- Creekmore, S.P., Graham, M.M., Jahn, G.E., Targett, R.C., and McIlroy, M.B. (1982) Comparison of methods of recording and analysis of Doppler blood velocity signals in normal subjects. Ultrasound Med. Biol., 8: 525 - 535.
- Deters, O.J., Mark, F.F., Barger, C.B., Friedman, M.H., and Hutchins, G.M. (1984) Comparison of steady and pulsatile flow near the ventral and dorsal walls of casts of human aortic bifurcations. Trans. ASME. J. Biomech. Eng., 106: 79 - 82.
- D'Luna, L.J., Newhouse, V.L., and Giddens, D.P. (1982). In Vitro Doppler Detection of Axisymmetric Stenoses From Transverse Velocity Measurements. J. Biomech., 15: 647 - 660.

- Eden, A. (1986) The Beginnings of Doppler. In: Transcranial Doppler Sonography, Ed. R. Aaslid. Springer-Verlag, pp. 1 - 9.
- El Masrey, O.A., Feuerstein, I.A., and Round, G.F. (1978) Experimental evaluation of streamline patterns and separated flows in a series of branching vessels with implications for atherosclerosis and thrombosis. Circ. Res., 43: 608 - 618.
- Evans, D.H. (1982) Some aspects of the relationship between instantaneous volumetric blood flow and continuous wave Doppler ultrasound recordings-I: The effect of ultrasound beam width on the output of maximum, mean, and rms frequency processors. Ultrasound Med. Biol., 8: 605 - 609.
- Falsetti, H.L., Kiser, K.M., Francis, G.P., and Belmore, E.R. (1972) Sequential velocity development in the ascending and descending aorta of the dog. Circ. Res., 31: 328 - 338.
- Farthing, S., and Peronneau, P. (1979) Flow in the thoracic aorta. Cardiovasc. Res., 13: 607 - 620.
- Fell, G., Philips, D.J., Chikos, P.M., Harley, J.D., Thiele, B.L., and Strandness, D.E. (1981) Ultrasonic duplex scanning for disease of the carotid artery. Circulation, 64: 1191 - 1195.
- Fish, P. J. (1981) A Method of Transcutaneous Blood Flow Measurement - Accuracy Considerations. In: Recent Advances in Ultrasound Diagnosis, Vol. 3. Eds. Kurjak, A., and Kratochwil, A. Elsevier North-Holland, pp. 110 -115.
- Forster, F. K. (1977) The applications and limitations of Doppler spectral broadening measurements for the detection of cardiovascular disorders. In: Ultrasound in Medicine, Vol. 3b. Eds. White, D., and Brown, R. E. Plenum Press, New York, pp. 1223 - 1226.

- Fox, J.A., and Hugh, A.E. (1966). Localization of Atheroma: A Theory Based on Boundary Layer Separation. Brit. Heart J., 28: 388 - 399.
- Freed, D., Hartley, C. J., Christman, K. D., Lyman, R. C., Agris, J., and Walker, W. F. (1979) High-Frequency Pulsed Doppler Ultrasound: A New Tool for Microvascular Surgery. J. Microsurgery, 1: 148 - 153.
- Friedman, M.H., Bargerion, C.B., Hutchins, G.M., Mark, F.F., and Deters, O.J. (1980) Hemodynamic measurements in human arterial casts, and their correlation with histology and luminal area. Trans. ASME. J. Biomech. Eng., 102: 247 - 251.
- Friedman, M.H., Hutchins, G.M., Bargerion, C.B., Deters, O.J., and Mark, F.F. (1981) Correlation between intimal thickness and fluid shear in human arteries. Atherosclerosis, 39: 425 - 436.
- Friedman, M.H., Deters, O.J., Mark, F.F., Bargerion, C.B., and Hutchins, G.M. (1983). Geometric Effects on the Hemodynamic Environment of the Arterial Wall: A Basis for Geometric Risk Factors ? In: Fluid Dynamics as a Localizing Factor for Atherosclerosis, Eds. Schettler, G., Nerem, R.M., Schmid-Schonbein, H., Morl, H. and Diehm, C. Springer - Verlag, pp. 71 - 78.
- Friedman, M.H., Bargerion, C.B., Deters, O.J., Hutchins, G.M., and Mark, F.F. (1987) Correlation between wall shear and intimal thickness at a coronary artery branch. Atherosclerosis, 68: 27 - 33.
- Friedman, M. H., O'Brien, V., and Ehrlich, L. W. (1975) Calculations of Pulsatile Flow Through a Branch. Circ. Res., 36: 277 - 285.
- Fry, D.L. (1968) Acute Vascular Endothelial Changes Associated With Increased Blood Velocity Gradients. Circ. Res. 22: 165 - 197.
- Fry, D.L. (1969) Certain Histological and Chemical Responses of the Vascular Interface to Acutely Induced Mechanical Stress in the Aorta of the Dog. Circ. Res. 24: 93 - 108.

- Fukushima, T., Homma, T., Harakawa, K., Sakata, N., and Azuma, T. (1988) Vortex generation in pulsatile flow through arterial bifurcation models including the human carotid artery. Trans. ASME. J. Biomech. Eng., 110: 166 - 171.
- Garbini, J.L. (1973) An Analytical Procedure of Calibration for the Pulsed Ultrasonic Doppler Flow Meter. M.Sc. Thesis, University of Washington.
- Garbini, J.L., Forster, F.K., and Jorgensen, J.E. (1982) Measurement of fluid turbulence based on pulsed ultrasound techniques. Part 1. Analysis. J. Fluid Mech., 118: 445 - 470.
- Garbini, J.L., Forster, F.K., and Jorgensen, J.E. (1982) Measurement of fluid turbulence based on pulsed ultrasound techniques. Part 2. Experimental investigation. J. Fluid Mech., 118: 471 - 505.
- Gessner, F. B. (1973) Hemodynamic Theories of Atherogenesis. Circ. Res., 33: 259 - 266.
- Giddens, D. P., and Khalifa, A. M. A. (1982) Turbulence Measurements with Pulsed Doppler Ultrasound Employing a Frequency Tracking Method. Ultrasound Med. Biol., 8: 427 - 437.
- Giddens, D.P., Mabon, R.F., and Cassanova, R.A. (1976) Measurements of Disordered Flows Distal to Subtotal Vascular Stenoses in the Thoracic Aortas of Dogs. Circ. Res., 39: 112 - 119.
- Gill, R.W., (1979a) Performance of the mean frequency Doppler modulator. Ultrasound Med. Biol., 5: 237 - 247.
- Gill, R.W. (1979b) Pulsed Doppler with B-mode imaging for quantitative blood flow measurement. Ultrasound Med. Biol., 5: 223 - 235.
- Gill, R. W. (1985) Measurement of Blood Flow by Ultrasound: Accuracy and Sources of Error. Ultrasound Med. Biol. 11: 625 - 641.

- Gilsbach, J., and Harders, A. (1986) Comparison of intraoperative and transcranial Doppler. In: Transcranial Doppler Sonography, Ed. R. Aaslid. Springer-Verlag, pp. 106 - 117.
- Greene, E.R., and Hestand, M.B. (1979). Ultrasonic Assessment of simulated atherosclerosis: *In vitro* and *in vivo* comparisons. Trans. ASME. J. Biomech. Eng., 101: 73 - 81.
- Greene, F.M., Beach, K., Strandness, D.E., Fell, G., and Phillips, D.J. (1982) Computer based pattern recognition of carotid arterial disease using pulsed Doppler ultrasound. Ultrasound Med. Biol., 8: 161 - 176.
- Gutstein, W.H., Farrell, G.A., and Schneck, D.J. (1970) *In vivo* demonstration of junctional blood flow disturbance by hot wire anemometry. Atherosclerosis, 11: 485 - 496.
- Gutstein, W.H., Schneck, D.J., and Marks, J.O. (1968) *In vitro* studies of local blood flow disturbance in a region of separation. J. Atherosclerosis Res., 8: 381 - 388.
- Gutstein, W.H., Farrell, G.A., and Armellini, C. (1973) Blood flow disturbance and endothelial cell injury in preatherosclerotic swine. Lab. Invest., 29: 134 - 149.
- Hale, J.F., McDonald, D.A, and Womersley, J.R. (1955) Velocity Profiles of Oscillating Arterial Flow, With Some Calculations of Viscous Drag and the Reynolds Number. J. Physiol., 128: 629 - 640.
- Hartley, C.J., Hanley, H.G., Lewis, R.M., and Cole, J.S. (1978) Synchronized Pulsed Doppler Flow and Ultrasonic Dimension Measurement in Conscious Dogs. Ultrasound Med. Biol., 4: 99 - 100.
- Hay, W.B. (1976) Effect of Downstream Resistance on the Pressure Drop Across Minor Stenoses. M.Sc. thesis, University of Alberta.

- Histand, M.B., Miller, C.W., and McLeod, F.D. (1973) Transcutaneous measurement of blood velocity profiles and flow. Cardiovasc. Res., 7: 703 - 712.
- Hoeks, A.P.G., Reneman, R.S., Ruissen, C.J., and Smeets, F.A.M. (1979) Possibilities and limitations of pulsed Doppler systems. In: Echocardiology, Ed. C.T. Lancee. Martinus Nijhoff, pp. 413 - 419.
- Hoeks, A.P.G., Ruissen, C.J., Hick, P., and Reneman, R.S. (1984) Methods to evaluate the sample volume of pulsed Doppler systems. Ultrasound Med. Biol., 10: 427 - 434.
- Holen, J., Wagg, R.C., and Gramiak, R. (1985) Representations of rapidly oscillating structures on the Doppler display. Ultrasound Med. Biol., 11: 267 - 272.
- Holland, S. K., Orphanoudakis, S. C., and Jaffe, C. C. (1984) Frequency-Dependent Attenuation Effects in Pulsed Doppler Ultrasound: Experimental Results. IEEE Trans. Biomed. Eng., BME-31: 626 - 631.
- Houle, S., and Roach, M.R. (1981) Flow studies in a rigid model of an aorto-renal junction. A case for high shear as a cause for localization of sudanophilic lesions in rabbits. Atherosclerosis, 40: 231 - 244.
- Hutchison, K. J., and Karpinski, E. (1982) Flow Disturbance Downstream of Moderate Stenosis in the Canine Common Carotid Artery. In: Biomedical Engineering 1: Recent Developments. Ed. Saha, S. Pergamen Press, pp. 103 - 106.
- Hutchison, K.J., and Karpinski, E. (1985) *In Vivo* Demonstration of Flow Recirculation and Turbulence Downstream of Graded Stenoses In Canine Arteries. J. Biomech., 18: 285 - 296.
- Hutchison, K.J., and Karpinski, E. (1988) Stability of flow patterns in the *in vivo* post-stenotic velocity field. Ultrasound Med. Biol., 14: 269 - 275.

- Hutchison, K. J., Oberle, K., Scott, J. A., and French, A. S. (1981) A Comparison of Doppler Ultrasonic Waveforms Processed by Zero Crossing and Spectrographic Techniques in the Diagnosis of Arterial Disease. Angiology, 32: 277 - 289.
- Jager, K.A., Phillips, D.J., Martin, R.L., Hanson, C., Roederer, G.O., Langlois, Y.E., Ricketts, H.J., and Strandness, D.E. (1985) Noninvasive mapping of lower limb arterial lesions. Ultrasound Med. Biol., 11: 515 - 521.
- Johnston, K.W., Maruzzo, B.C., and Cobbold, R.S.C. (1977) Errors and artifacts of Doppler flowmeters and their solution. Arch. Surg., 112: 1335 - 1342.
- Johnston, K.W., Maruzzo, B.C., and Cobbold, R.S.C. (1978) Doppler methods for quantitative measurement and localization of peripheral arterial occlusive disease by analysis of the blood velocity waveform. Ultrasound Med. Biol., 4: 209 - 223.
- Jorgensen, J.E., Campau, D.N., and Baker, D.W. (1973) Physical Characteristics and Mathematical Modelling of the Pulsed Ultrasonic Flowmeter. Med. Biol. Engng., 11: 404 - 420.
- Jorgensen, J.E., and Garbini, J.L. (1974) An analytical procedure of calibration for the pulsed ultrasonic Doppler flow meter. Trans. ASME. J. Fluids Eng., 96: 158 - 167.
- Kajiya, F., Koki, N., Tomonaga, G., and Nishihara, H. (1981) A laser-Doppler-velocimeter using an optical fiber and its application to local velocity measurement in the coronary artery. Experientia, 37: 1171 - 1173.
- Kaneko, Z. (1986) First Steps in the Development of the Doppler Flowmeter. Ultrasound Med. Biol., 12: 187 - 195.
- Karino, T., Kwong, H.H.M., and Goldsmith, H.L. (1979) Particle flow behaviour in models of branching vessels - I. Vortices in 90 degree T-junctions. Biorheology, 16: 231 - 248.

- Karino, T., and Goldsmith, H.L. (1985) Particle flow behaviour in models of branching vessels - II. Effects of branching angle and diameter ratio on flow patterns. Biorheology, 22: 87 - 104.
- Kassam, M.S., Cobbold, R.S.C., Johnston, K.W., and Graham, C.M. (1982) Method for estimating the Doppler mean velocity waveform. Ultrasound Med. Biol., 8: 537 - 544.
- Kempczinski, R.F. (1979) Role of the vascular diagnostic laboratory in the evaluation of male impotence. Am. J. Surg., 138: 278 - 282.
- Khalifa, A. M. A. (1978) The Role of Flow Disorder in the Non-invasive Detection of Atherosclerosis. Ph.D. thesis, Georgia Institute of Technology.
- Khalifa, A.M.A., and Giddens, D.P. (1981) Characterization and evolution of poststenotic flow disturbances. J. Biomech., 14: 279 - 296.
- Khalifa, A.M.A., and Giddens, D.P. (1978) Analysis of disorder in pulsatile flows with application to poststenotic blood velocity measurement in dogs. J. Biomech., 11: 129 - 141.
- Kim, B.M., and Corcoran, W.H. (1974) Experimental measurements of turbulence spectra distal to stenoses. J. Biomech., 7: 335 - 342.
- Kiser, K.M., Falsetti, H.L., Yu, K.H., Resitarits, M.R., Francis, G.P., and Carroll, R.J. (1976) Measurements of velocity waveforms in the dog aorta. Trans. ASME. J. Fluids Eng., 98: 297 - 304.
- Kjaernes, M., Svindland, A., Walloe, L., and Wille, S.O. (1981) Localization of Early Atherosclerotic Lesions in an Arterial Bifurcation in Humans. Acta. Pathol. Microbiol. Scand.(Sect.A), 89: 35 - 40.

- Knox, R.A., Greene, F.M., Beach, K., Phillips, D.J., Chikos, P.M., and Strandness, D.E. (1982) Computer based classification of carotid arterial disease: a prospective assessment. Stroke, 13: 589 - 594.
- Knox, R.A., Phillips, D.J., Breslau, P.J., Lawrence, R., Primozich, J., And Strandness, D.E. (1982) Empirical findings relating sample volume size to diagnostic accuracy in pulsed Doppler cerebrovascular studies. J. Clin. Ultrasound, 10: 227 - 232.
- Kock, W.E. (1973) Radar, Sonar, and Holography: An Introduction. Academic Press.
- Ku, D.N., and Giddens, D.P. (1983) Pulsatile flow in a model carotid bifurcation. Arteriosclerosis, 3: 31 - 39.
- Ku, D.N., Giddens, D.P., Zarins, C.K., and Glagov, S. (1985a). Pulsatile Flow and Atherosclerosis in the Human Carotid Biurcation: Positive Correlation Between Plaque Location and Low and Oscillating Shear Stress. Arteriosclerosis, 5: 293 - 392.
- Ku, D.N., Giddens, D.P., Phillips, D.J., and Strandness, D.E. (1985b) Hemodynamics of the normal carotid bifurcation: *In vitro* and *in vivo* studies. Ultrasound Med. Biol., 11: 13 - 26.
- Langlois, Y.E., Greene, F.M., Roederer, G.O., Jager, K.A., Phillips, D.J., Beach, K.W., and Strandness, D.E. (1984) Computer based pattern recognition of carotid artery Doppler signals for disease classification: prospective validation. Ultrasound Med. Biol., 10: 581 - 595.
- Lesvesque, M.J., Liepsch, D., Moravec, S., and Nerem, R.M. (1986) Correlation of endothelial cell shape and wall shear stress in a stenosed dog aorta. Arteriosclerosis , 6: 220 - 229.
- Levy, R.I. (1981). Declining Mortality in Coronary Heart Disease. Arteriosclerosis, 1: 312 - 325.

- Liepsch, D., Moravec, S., Rastogi, A.K., and Vlachos, N.S. (1982) Measurement and calculations of laminar flow in a ninety degree bifurcation. J. Biomech., 15: 473 - 485.
- Light, H., and Cross, G. (1972) Cardiovascular data by transcutaneous aortovelocity. In: Blood Flow Measurement. Ed. C. Roberts. Williams and Wilkins, Baltimore, pp. 60 - 63.
- Lindegaard, K.F., Grolimund, P., Aaslid, R., and Nornes, H. (1986) Evaluation of cerebral AVM's using transcranial Doppler ultrasound. J. Neurosurg., 65: 335 - 344.
- Ling, S.C., Atabek, H.B., Fry, D.L., Patel, D.J., and Janicki, J.S. (1968) Application of heated-film velocity and shear probes to hemodynamic studies Circ. Res., 23: 789 - 801.
- Logerfo, F.W., Crawshaw, H.M., Nowak, M., Serrallach, E.S., Quist, W.C., and Valeri, C.R. (1981a) Effect of flow split on separation and stagnation in a model vascular bifurcation. Stroke, 12: 660 - 665.
- Logerfo, F.W., Nowak, M.D., Quist, W.C., Crawshaw, H.M., and Bharadvaj, B.K. (1981b) Flow studies in a model carotid bifurcation. Arteriosclerosis, 1: 235 - 241.
- Lucas, C.L., Keagy, B.A., Hsiao, H.S., Johnson, T.A., Henry, G.W., and Wilcox, B.R. (1984) The velocity profile in the canine ascending aorta and its effects on the accuracy of pulsed Doppler determinations of mean blood velocity. Cardiovasc. Res., 18: 282 - 293.
- Lutz, R.J., Hsu, L., Menawat, A., Zrubek, J., and Edwards, K. (1983) Comparison of steady and pulsatile flow in a double branching arterial model. J. Biomech., 16: 753 - 766.
- Lye, C.R., Sumner, D.S., and Strandness, D.E. (1976) The accuracy of the supraorbital Doppler examination in the diagnosis of hemodynamically significant carotid occlusive disease. Surgery, 79: 42 - 45.

- Lyne, W.H. (1970) Unsteady viscous flow in a curved pipe. J. Fluid Mech., 45: 13 - 31.
- Malcolm, A.D., and Roach, M.R. (1979) Flow disturbances at the apex and lateral angles of a variety of bifurcation models and their role in development and manifestations of arterial disease. Stroke, 10: 335 - 343.
- Mark, F.F., Bargeron, C.B., Deters, O.J., and Friedman, M.H. (1985) Nonquasi-steady character of pulsatile flow in human coronary arteries. Trans. ASME. J. Biomech. Eng. , 107: 24 - 28.
- Martin, G.H. (1982) Kinematics and Dynamics of Machines, second edition. McGraw-Hill, Toronto.
- McDicken, W.N. (1986) A versatile test-object for the calibration of ultrasonic Doppler flow instruments. Ultrasound Med. Biol., 12: 245 - 249.
- McDonald, D.A. (1952) The occurrence of turbulent blood flow in the rabbit aorta. J. Physiol., 118: 340 - 347.
- McDonald, D.A. (1955). The Relation of Pulsatile Pressure to Flow in Arteries. J. Physiol., 127: 533 - 552.
- McDonald, D.A. (1974). Blood Flow In Arteries, second edition. Edward Arnold Ltd., London.
- Merzkirch, W. (1979) Making fluid flows visible. Amer. Scientist, 67: 330 - 336.
- Miller, C.W., Histan, M.B., Brooks, R.K., Brewster, R.D., and McLeod, F.D. (1972) The chronic measurement of local flow properties in the abdominal aorta of dogs. Med. Res. Eng., 11: 17 - 23.

- Miller, G. E., and Hollis, T. M. (1980) Wall Shear Stress in the Aorta. Chem. Eng. Commun., 7: 113 - 119.
- Morin, J.F., Johnston, K.W., and Law, Y.F. (1987) *In vitro* study of continuous wave Doppler spectral changes resulting from stenoses and bulbs. Ultrasound Med. Biol. , 13: 5 - 13.
- Morin, J.F., Johnston, K.W., and Law, Y.F. (1988) Factors affecting the continuous wave Doppler spectrum for the diagnosis of carotid arterial disease. Ultrasound Med. Biol., 14: 175 - 189.
- Morris, R.L., Hestand, M.B., and Miller, C.W. (1973) The resolution of the ultrasound pulsed Doppler for blood velocity measurements. J. Biomech., 6: 701 - 710.
- Naumann, A., and Schmid-Schonbein, H. (1983). A Fluid - Dynamicist's and a Physiologist's Look at Arterial Flow and Arteriosclerosis. In: Fluid Dynamics as a Localizing Factor for Atherosclerosis, Eds. Schettler, G., Nerem, R.M., Schmid-Schonbein, H., Morl, H., and Diehm, C. Springer - Verlag, pp. 9 - 25.
- Nerem, R.M. (1981). Arterial Fluid Dynamics and Interactions With the Vessel Walls. In: Structure and Function of the Circulation. Ed. Schwartz, C.J., Werthessen, N.T., and Wolf, S. Plenum Press, pp. 719 - 835.
- Nerem, R.M., and Seed, W.A. (1972) An *in vivo* study of aortic flow disturbances. Cardiovasc. Res., 6: 1 - 14.
- Nerem, R.M., Seed, W.A., and Wood, N.B. (1972) An experimental study of the velocity distribution and transition to turbulence in the aorta. J. Fluid Mech. , 52: 137 - 160.
- Nerem, R.M., Rumberger, J.A., Gross, D.R., Hamlin, R.L., and Geiger, G.L. (1974) Hot film anemometer velocity measurements of arterial blood flow in horses. Circ. Res. , 34: 193 - 203.

- Nerem, R.M., Rumberger, J.A., Gross, D.R., Muir, W.A., and Geiger, G.L. (1976) Hot film coronary artery velocity measurements in horses. Cardiovasc. Res., 10: 307 - 313.
- Nerem, R.M., and Levesque, M.J. (1983). The Case for Fluid Dynamics as a Localizing Factor in Atherogenesis. In: Fluid Dynamics as a Localizing Factor for Atherosclerosis. Eds. Schettler, G., Nerem, R.M. Schmid-Schonbein, H., Morl, H. and Diehm, C. Springer - Verlag, pp. 26 - 37.
- Newhouse, V.L., Nathan, R.S., and Hertzler, L.W. (1982) A proposed standard target for ultrasound Doppler gain calibration. Ultrasound Med. Biol., 8: 313 - 316.
- Newhouse, V.L., Furgason, E.S., Johnson, G.F., and Wolf, D.A. (1980) The dependence of ultrasound Doppler bandwidth on beam geometry. IEEE Trans. Sonics Ultrason., SU-27: 50 - 59.
- Nippa, J. H., Hokanson, D. E., Lee, D. R., Sumner, D.S., and Strandness, D.E. (1975) Phase rotation for separating forward and reverse blood velocity signals. IEEE Trans. Sonics Ultrasonics, SU-22: 340 - 346.
- Nowicki, A., Karlowicz, P., Piechocki, M., and Secomski, W. (1985) Method for the measurement of the maximum Doppler frequency. Ultrasound Med. Biol., 11: 479 - 486.
- O'Connell, R. G. (1986) The Role of Doppler Ultrasound in Cardiac Diagnosis. Hewlett-Packard J., 37: 20 - 25.
- Pelot, R. (1981) Flow Characteristics In The Aortic Arch. M.Sc. Thesis, University of Alberta.
- Peronneau, P., Sandman, W., and Xhaard, M. (1977). Blood Flow Patterns In Large Arteries. In: Ultrasound In Medicine, Vol. 3b. Eds. White, D., and Brown, R.E. Plenum Press, pp. 1193 - 1208.

- Phillips, D.J., Greene, F.M., Langlois, Y., Roederer, G.O., and Strandness, D.E. (1983) Flow velocity patterns in the carotid bifurcations of young presumed normal subjects. Ultrasound Med. Biol. , 9: 39 - 49.
- Philpot, E., Yoganathan, A.P., Sung, H-W, Woo, Y-R, Franch, R.H., Sahn, D.J., and Valdez-Cruz, L. (1985) *In vitro* pulsatile flow visualization studies in a pulmonary artery model. Trans. ASME: J. Biomech. Eng. , 107: 368 - 375.
- Poots, J. K., Johnston, K. W., Cobbold, R. S. C., and Kassam, M. (1986) Comparison of CW Doppler Ultrasound Spectra with the Spectra Derived from a Flow Visualization Model. Ultrasound Med. Biol., 12: 125 - 133.
- Reneman, R.S., and Spencer, M.P. (1974) Difficulties in processing of an analogue Doppler flow signal; with special reference to zero-crossing meters and quantification. In: Cardiovascular Applications of Ultrasound. Ed. Reneman, R.S. North Holland, pp. 32 - 42.
- Reneman, R. S., Van Merode, T., Hick, P., and Hoeks, A. P. G. (1986) Cardiovascular Applications of Multi-Gate Pulsed Doppler Systems. Ultrasound Med. Biol., 12: 357 - 370.
- Rittgers, S.E., Fei, Ding-yu, Kraft, K.A., Fatouros, P.P., and Kishore, P.R.S. (1988) Velocity profiles in stenosed tube models using magnetic resonance imaging. Trans. ASME: J. Biomech. Eng., 110: 180 - 184.
- Rittgers, S.E., Norris, C.S., and Barnes, R.W. (1985) Detection of renal artery stenosis : experimental and clinical analysis of velocity waveforms. Ultrasound Med. Biol., 11: 523 - 531.
- Roach, M.R. (1979) Hemodynamic factors in arterial stenosis and poststenotic dilatation. In: Hemodynamics and the Blood Vessel Wall. Ed. Stehbens, W.S., Charles C. Thomas Pub., pp. 439 - 464.

- Robbins, S.L., and Angell, M. (1976). Basic Pathology, second edition, W.B. Saunders Co., Toronto.
- Roberson, J.A., and Crowe, C.T. (1980). Engineering Fluid Mechanics, second edition. Houghton Mifflin Co., Boston.
- Rodkiewicz, C.M. (1975) Localization of early atherosclerotic lesions in the aortic arch in the light of fluid flow. J. Biomech., 8: 149 - 156.
- Rodkiewicz, C.M., and Roussel, C.L. (1973). Fluid Mechanics in a Large Arterial Bifurcation. Trans. ASME : J. Fluids Eng., 95 (Series I): 108 - 112.
- Ross, R., and Glomset, J.A. (1976a). The Pathogenesis of Atherosclerosis. New Eng. J. Med., 295: 369 - 377.
- Ross, R., and Glomset, J.A. (1976b). The Pathogenesis of Atherosclerosis. New Eng. J. Med., 295: 420 - 425.
- Ross, R. (1981). Atherosclerosis: A Problem of the Biology of Arterial Wall Cells and Their Interaction With Blood Components. Arteriosclerosis., 1: 293 - 311.
- Ross, R. (1986). The Pathogenesis of Atherosclerosis - An Update. New Eng. J. Med., 314(8): 488 - 500.
- Sabbah, H.N., Hawkins, E.T., and Stein, P.D. (1984a) Flow separation in the renal arteries. Arteriosclerosis , 4: 28 - 33.
- Sabbah, H.N., Walburn, F.J., and Stein, P.D. (1984b) Patterns of flow in the left coronary artery. Trans. ASME. J. Biomech. Eng., 106: 272 - 279.

- Satomura, S. (1957) Ultrasonic Doppler method for the inspection of cardiac function. J. Acoust. Soc. Amer., 29: 1181 - 1185.
- Seed, W.A., and Wood, N.B. (1971) Velocity patterns in the aorta. Cardiovasc. Res., 5: 323 - 330.
- Seiler, R.W., Grolimund, P., Aaslid, R., Huber, P., and Nornes, H. (1986) Cerebral vasospasm evaluated by transcranial ultrasound correlated with clinical grade and CT-visualized subarachnoid hemorrhage. J. Neurosurg., 64: 594 - 600.
- Sigel, B., Gibson, R.J., Amatneek, K.V., Felix, W.R., Edelstein, A.L., and Popky, G.L. (1970) A Doppler ultrasound method for distinguishing laminar from turbulent flow. J. Surg. Res., 10: 221 - 224.
- Smith, F.T. (1975) Pulsatile flow in curved pipes. J. Fluid Mech., 71: 15 - 42.
- Spain, D. M.. (1966) Atherosclerosis. Sci. Amer., 215: 48 - 56.
- Spencer, M.P. (1986) Frequency Spectrum Analysis in Doppler Diagnosis. In: Introduction to Vascular Ultrasonography, second edition. Ed. Zwiebel, W.J., Grune and Stratton, pp. 53 - 80.
- Spencer, M. P., and Zwiebel, W. J. (1982) Frequency Spectrum Analysis in Doppler Diagnosis In: Introduction to Vascular Ultrasonography, Ed. Zwiebel, W. J., Grune and Stratton, pp. 151 - 177.
- Stehbens, W.E. (1975). The Role of Hemodynamics in the Pathogenesis of Atherosclerosis. Progr. Cardiovasc. Dis., 18: 89 - 103.
- Stehbens, W.E. (1974) Haemodynamic production of lipid deposition, intimal tears, mural dissection and thrombosis in the blood vessel wall. Proc. R. Soc. Lond. B., 185: 357 - 373.

Stehbens, W.E. (1973) Experimental arteriovenous fistulae in normal and cholesterol-fed rabbits. Pathology, 5: 311 - 324.

Stehbens, W.E. (1968) Blood vessel changes in chronic experimental arteriovenous fistulas. Surg. Gynec. Obstet. , 127: 327 - 338.

Strandness, D.E., and Bell, J.W. (1965) Peripheral vascular disease: diagnosis and objective evaluation using a mercury strain gauge. Ann. Surg. (Suppl.), 161: 1 - 35.

Strandness, D.E., and Bell, J.W. (1966) Ankle pressure responses after reconstructive surgery. Surgery, 59: 514 - 516.

Strandness, D. E. (1986) Ultrasound in the study of atherosclerosis. Ultrasound Med. Biol., 12: 453 - 464.

Sumner, D.S., and Strandness, D.E. (1969) The relationship between calf blood flow and ankle blood pressure in patients with intermittent claudication. Surgery, 65: 763 - 771.

Talbot, L., and Gong, K.O. (1983) Pulsatile entrance flow in a curved pipe. J. Fluid Mech., 127: 1 - 25.

Talukder, N., Fulenwider, J.T., Mabon, R.F., and Giddens, D.P. (1986) Post-stenotic flow disturbance in the dog aorta as measured with pulsed Doppler ultrasound. Trans. ASME : J. Biomech. Eng., 108: 259 - 265.

Tarbell, J.M., Chang, L.J., and Hollis, T.M. (1983) A Note on Wall Shear Stress in the Aorta. Trans. ASME. J. Biomech. Eng., 104: 343 - 345.

- Taylor, D.E.M. (1983) Introduction. In: Blood Flow, Theory and Practice. Eds. Taylor, D.E.M., and Stephens, A.L. Academic Press, pp. 3 - 5.
- Texon, M. (1957) A Hemodynamic Concept of Atherosclerosis With Particular Reference to Coronary Occlusion. AMA Arch. Int. Med., 99: 418 - 427.
- Thiele, B. L., Hutchison, K. J., Greene, F. M., Forster, F. K., and Taylor, D. E. (1983) Pulsed Doppler Waveform Patterns Produced by Smooth Stenosis in the Dog Thoracic Aorta. In: Blood Flow, Theory and Practice. Eds. Taylor, D. E. M., and Stevens, A. L., Academic Press, pp. 86 - 104.
- Verhoef, W. A., Cloostermans, M. J. T. M., and Thijssen, J. M. (1985) Diffraction and Dispersion Effects on the Estimation of Ultrasound Attenuation and Velocity in Biological Tissues. IEEE Trans. Biomed. Eng., BME-32: 521 - 529.
- Vieli, A., Jenni, R., and Anliker, M. (1986) Spatial Velocity Distributions in the Ascending Aorta of Healthy Humans and Cardiac Patients. IEEE Trans. Biomed. Eng., BME-33: 28 - 34.
- Voyles, W.F., Altobelli, S.A., Fisher, D.C., and Greene, E.R. (1985) A comparison of digital and analog methods of Doppler spectral analysis for quantifying flow. Ultrasound Med. Biol., 11: 727 - 734.
- Walburn, F.J., and Stein, P.D. (1980) Flow in a symmetrically branched tube simulating the aortic bifurcation: the effects of unevenly distributed flow. Ann. Biomed. Eng., 8: 159 - 173.
- Walker, A. R., Phillips, D. J., and Powers, J. E. (1982) Evaluating Doppler Devices Using A Moving String Test Target. J. Clin. Ultrasound, 10: 25 - 30.
- Wells, M.K., Winter, D.C., Nelson, A.W., and McCarthy, T.C. (1977) Blood velocity patterns in coronary arteries. Trans. ASME. J. Biomech. Eng., 99: 26 - 32.

- Wells, P.N.T., and Skidmore, R. (1985) Doppler developments in the last quinquennium. Ultrasound Med. Biol., 11: 613 - 623.
- Wesolowski, S.A., Fries, C.C., Sabini, A.M., and Sawyer, P.N. (1965) The Significance of Turbulence in Hemic Systems and in the the Distribution of the Atherosclerotic Lesion. Surgery, 57: 155 - 162.
- White, D.N. (1982) Johann Christian Doppler and his effect. Ultrasound Med. Biol., 8: 583 - 591.
- Willis, F.H. (1947) Measurements of Ultrasonic Absorption and Velocity in Liquid Mixtures. J. Acous. Soc. Am., 19: 242 - 248.
- Winsor, T., Haumschild, D.J., Winsor, D., and Mikail, A. (1989) Influence of local and environmental temperatures on cutaneous circulation with use of laser Doppler flowmetry. Angiology, 40: 421 - 428.
- Womersley, J.R. (1955) Method for the Calculation of Velocity, Rate of Flow and Viscous Drag in Arteries when the Pressure Gradient is Known. J. Physiol., 127: 553 - 563.
- Yamaguchi, T., Kikkawa, S., Yoshikawa, T., Tanishita, K., and Sugawara, M. (1983) Measurement of turbulence intensity in the center of the canine ascending aorta with a hot film anemometer. Trans. ASME. J. Biomech. Eng., 105: 177 - 187.
- Yao, J.S.T., Hobbs, J.T., and Irvine, W.T. (1969) Ankle systolic pressure measurements in arterial diseases affecting the lower extremities. Br. J. Surg., 56: 676 - 679.
- Yellin, E. L. (1966) Laminar-Turbulent Transition Process in Pulsatile Flow. Circ. Res., 19(4): 791 - 804.
- Yongchareon, W., and Young, D.F. (1979) Initiation of turbulence in models of arterial stenoses. J. Biomech. , 12: 185 - 196.

- Young, D.F. (1979) Fluid mechanics of arterial stenoses. Trans. ASME. J. Biomech. Eng., 101: 157 - 175.
- Young, D.F., and Tsai, F.Y. (1973a) Flow characteristics in models of arterial stenoses - I: Steady flow. J. Biomech., 6: 395 - 410.
- Young, D.F., and Tsai, F.Y. (1973b) Flow characteristics in models of arterial stenoses - I: Unsteady flow. J. Biomech., 6: 547 - 559.
- Zagzebski, J. A., and Madsen, E. L. (1982) Physics and Instrumentation in Doppler and B-Mode Ultrasonography. In: Introduction to Vascular Ultrasonography, Ed. Zwiebel, W. J., Grune and Stratton, pp. 1 - 21.
- Zagzebski, J. A. (1986) Physics and Instrumentation in Doppler and B-Mode Ultrasonography. In: Introduction to Vascular Ultrasonography, second edition. Ed. Zwiebel, W. J., Grune and Stratton, pp. 21 - 51.
- Zalosh, R.G., and Nelson, W.G. (1973) Pulsating flow in a curved tube. J. Fluid Mech., 59: 693 - 705.
- Zarins, C.K., Giddens, D.P., Bharadvaj, B.K., Sottiurai, V.S., Mabon, R.F., and Glagov, S. (1983) Carotid Bifurcation Atherosclerosis: Quantitative Correlation of Plaque Localization With Flow Velocity Profiles and Wall Shear Stress. Circ. Res., 53: 502 - 514.
- Zierler, R.E., Roederer, G.O., and Strandness, D.E. (1983a) The use of frequency spectral analysis in carotid artery surgery. In: Cerebrovascular Insufficiency, Eds. J.J. Bergan and J.S.T. Yao. Grune and Stratton.
- Zierler, R.E., Bandyk, D.F., Berni, G.A., and Thiele, B.L. (1983b) Intraoperative pulsed Doppler assessment of carotid endarterectomy. Ultrasound Med. Biol., 9: 65 - 71.
- Zierler, R.E., and Strandness, D.E. (1984) Doppler From A Clinician's Viewpoint In: Vascular and Doppler Ultrasound, Ed. C. Carl Jaffe, Churchill Livingstone, pp. 51 - 68.

APPENDIX

At the time of printing of this thesis some of its contents had already been published in the following two journals:

J. Biomechanics, vol. 21, no. 4, pp. 277 - 286, 1988.
Authors: K.J. Hutchison, E. Karpinski, J.D. Campbell (thesis author), and A. Potemkowski.

Ultrasound Med. Biol., vol. 15, no. 7, pp. 611 - 619, 1989.
Authors: J.D. Campbell (thesis author), K.J. Hutchison, and E. Karpinski.

Significant parts of the textual methods, results, and discussion in these papers were incorporated into the methods, results, and discussion texts of this thesis. Furthermore, figures 1 through 9 in the J. Biomech. paper appear as figures 11, 12, 13, 32, 33, 34, 35, 36, and 37 respectively in the thesis. Figures 1 through 3 and 5 through 9 in the Ultrasound Med. Biol. paper appear as figures 3, 4, 16, 46, 47, 48, 49, and 50 respectively in the thesis. Also, table 1 in the Ultrasound Med. Biol. paper appears as table 6 in the thesis.